Alma Mater Studiorum · Università di Bologna

DOTTORATO DI RICERCA IN FISICA

Ciclo XXX

Settore Concorsuale di afferenza: 02/B3
Settore Scientifico disciplinare: FIS/07

Potassium channels and bioelectrical cellular properties during interactions with conductive polymers, electrotaxis and accelerated aging

Presentata da: Fabrizio Amorini

Coordinatore Dottorato:
Prof.ssa Silvia Arcelli

Supervisore:
Prof. Gastone Castellani

Co-supervisore:
Dott.ssa Isabella Zironi

Esame finale anno 2018

Abstract

Bioelectrical properties of the plasma membrane heavily characterize a living cell, they govern manifold functions of the cellular machinery and their alteration may lead to breakdown in its metabolism, loss of homeostasis, and finally death. By monitoring the potassium voltage-gated ion channels activity it was possible to study different topics. First, the interaction between cells and redox forms of organic films made by poly(3,4-ethylenedioxythiophene):poly(styre-nesulfonate) (PEDOT:PSS) was investigated, finding that the redox processes confer to PEDOT:PSS substrates the property to modify the ionic environment at the film-liquid interface through a "sponge-like" effect on ions, affecting cellular electrophysiology and functionality. Subsequently cell migration was studied under the action of external electric fields through the use of a programmable electronic board; preliminary results verified the success of this device in creating and controlling galvanotactic events. Finally, the premature aging process in cells carrying a G608G *LMNA* mutation, known as Hutchinson-Gilford Progeria Syndrome (HGPS) was assessed; highlighting that cells affected by HGPS overexpress BK_{Ca} channels on plasma membrane, and this seems to be correlated with an impaired replicative potential if compared to healthy cells.

Contents

Introduction

The first scientific observations regarding bioelectric properties of cells date back to the late 19th and were carried out by studying the excitability of nerve and muscle tissue. In the early 1880s Sidney Ringer published four papers [1, 2, 3, 4] considered the starting point for the development of the modern physiology, demonstrating the key role played by calcium in the contraction of the heart, as well as the possibility to maintain the normal heart beat form and frequency for several hours using a precise composition of a saline solution, showing for the first time, the importance of sodium, potassium and calcium ions in cell electrophysiology [5]. Walther H. Nernst gave a great contribution to the study of membrane potential, finding a mathematical relationship, known as Nernst equation (1888), by studying the electrical potentials arising from the diffusion of electrolytes in solution [6]. However, the basic propositions of the classical membrane theory were formulated only in the early 20th century by Bernstein [7, 8] and developed in a series of papers by Höber [9].

The existence of ion channels was hypothesized by the british biophysicists Alan Hodgkin and Andrew Huxley in their famous work published in 1952 [10] reporting their findings regarding action potentials recorded in nerves. For their discoveries *"concerning the ionic mechanisms involved in excitation and inhibition in the peripheral and central portions of the nerve cell membrane"* they received the Noble Prize in Physiology or Medicine in 1963 [11] together with Sir John Carew Eccles. Ion channel's existence was definitively confirmed in the 1970s by Neher and Sakmann, who developed an electrical recording

technique known as patch-clamp by which they obtained the first registration of a current flowing through a single channel [12] and for their discoveries concerning the function of single ion channels in cells they received the Nobel Prize in Physiology or Medicine in 1991 [13]. With this technique, a very tight seal is established between a glass pipette's tip and the plasma membrane, thus isolating small membrane patch. The ensuing decrease in background electrical noise allows one to reliably measure currents of the order of pA, the typical magnitude of cellular ionic currents. If the membrane patch is gently perforated by a depression, electrical access is obtained to the currents flowing through the entire cell's membrane, realizing the so called whole cell configuration. However the first X-ray resolved structure of an ion channel was actually obtained much later, studing a voltage-gated potassium channel from the bacterium Streptomyces Lividans [14]; the results achieved with this technique proved to be very useful to better understand the spatial organization of the amino-acids chains that compose the channel domains, as well as its selective properties.

Therefore, the last twenty-five years have witnessed an explosive growth of mammalian cell physiology, and many researchers, such as biologists, physiologists but also biophysicists and bioengineers continue to study these proteins to reach a more detailed understanding of how they exactly work. These researches also revealed that ion channels are implicated in manifold cellular processes and pathological conditions, such as: cell cycle, substrate adhesion, motility, carcinogenesis and ageing [15]. The aim of this work is to give a contribution in current interesting topics of biophysics, that are: i) the interaction between cells and organic polymeric matrices, ii) the effect of electric fields on cellular migration and iii) the identification of biomarkers for study the ageing process, starting from an experimental approach and an electrophysiological point of view, focused on a specific type of transmembrane potassium channel and the connections with the biological processes.

In particular, in the first Chapter, after a brief description regarding the bioelectrical properties of cells, and the molecular structure of a potassium ion channel, an overview on the main biological processes in which ion channels

play a key role is presented, with particular attention on cellular adhesion, migration and proliferation.

The materials, protocols and equipment used in the different experiments performed, are described in the second Chapter, focusing the attention on the patch clamp technique.

In the third Chapter are presented the results obtained by studying the biochemical properties of poly(3,4-ethylenedioxythiophene)poly(styrenesulfonate) (PEDOT:PSS) films. This organic polymer is a highly conductive material with good thermal and chemical stability and enhanced biocompatibility that make it suitable for bioengineering applications. In this work PEDOT:PSS has been studied as substrate for cell cultures, pointing out an interesting correlation between its redox state and the modulation effect on the bioelectrical properties of non-excitable cells. In particular, through the use of: i) electrophysiological response of the plasma membrane considered as a biosensor of the ionic availability; ii) X-ray spectroscopy to assess the ion exchange capability of PEDOT:PSS, and iii) atomic force microscopy to monitor PEDOT:PSS film thickness relative to its oxidation state, by which it has been possible to demonstrate that redox processes confer to PEDOT:PSS the property to modify the ionic environment at the film-liquid interface, through a "sponge-like" effect on ions. Finally, this work shows how this property offers the capability to electrically control central cellular properties, such as substrate adhesion and growth. Furthermore the electrical control of the oxidation state of PEDOT:PSS films allows to modulate peculiar physical and chemical properties of the material, such as topography, wettability and conductivity [16]. These experiments were developed in collaboration with the Materials Physics research group of the Department of Physics and Astronomy of the University of Bologna, coordinated by Prof. B. Fraboni.

In the fourth Chapter is described a study regarding the galvanotaxis phenomenon, namely the movement of an organism or any of its parts in a specific direction in response to an electric field, discovered since the end of the 19th century. In particular, a number of *in vitro* studies clearly showed that cells, when subjected to electric fields of the same magnitude of

the endogenous ones, tend to orientate and to migrate moving towards the cathode or the anode, depending on the cell type. This behavior seems to be present in many physiological processes, such as: embryogenesis, angiogenesis and tumor metastases. The main purpose of this project was to design and develop an electronic system capable to generate electric fields, and then galvanotactic events, in a scientific and easily reproducible manner. The prototyping board has been realized by Dr. A. Gabrielli and Dr. L. Boccioletti of the Department of Physics and Astronomy of the University of Bologna and tested in our biophysical laboratory. The results presented here come from preliminary experiments finalized to assess the performances of this device.

In the fifth Chapter a study concerning the involvement of ion channels in aging mechanisms by examining the Hutchinson-Gilford progeria syndrome (HGPS) is presented. HGPS is an extremely rare genetic disorder wherein symptoms resembling aspects of aging are manifested at a very early age. It is a genetic condition that occurs as a new mutation in the gene encoding for the nuclear structural protein lamin A (*LMNA*). The lamin family of proteins are thought to be involved in nuclear stability, chromatin structure and gene expression and this lead to heavy effects on the regulation and functionality of the cell machinery [17, 18]. Focusing on the large-conductance calcium-activated potassium (BK_{Ca}) channel expression, it was found that: i) the outward potassium (K^+) membrane current amplitude is positively affected by HGPS, if compared to that from healthy cells of juvenile subjects; ii) these results appear to be correlated with basic cellular activities, such as the adhesion process and the replicative boost. The functional role of BK_{Ca} currents is still unclear, but has been recently described a strong relationship with their membrane expression and the ageing process [19]. Therefore, the study of the HGPS also from the electrophysiological point of view might reveal new clues about the normal process of aging. This work was carried out in collaboration with the research group of Prof. G. Lattanzi (Institute of Molecular Genetics, C.N.R., Bologna, Italy), while primary dermal fibroblasts (hDF) from human donors were gently provided

by Prof. S. Salvioli (Department of Experimental, Diagnostic and Specialty Medicine, University of Bologna).

Chapter 1

Bioelectrical properties of cells

In this first Chapter, some basic concepts of cellular biology strictly necessary for the understanding of the experiments performed in this work and for their correct interpretation are presented. At the beginning, the description of the plasma membrane ion channels and bioelectric properties of cells are given. Afterwards attention has been focused on the structure of potassium channels and on their involvement in setting the resting membrane potential of cells. Finally, implications of this specific ion channel activity in some biological processes, such as adhesion, migration and proliferation are presented in detail.

1.1 Plasma membranes and ion channels

Ion channels are pore-forming proteins present on the membrane of any type of cell. Their main function is to facilitate the trafficking of hydrophilic and charged molecules, especially ions, through the cell membranes, which consist of a phospholipid bilayer impermeable to them.

Today it is believed that biological membranes, in the form of primitive self-assembled lipid bilayers, played a crucial role in the origin of life. In fact, thanks to their hydrophobic properties, they acted as a selectively permeable barrier with the fundamental function of creating vesicles and

compartmentalized areas with particular physical and chemical conditions suitable to start the basic reactions necessary for cellular metabolism [20].

Compared to carrier proteins and other proteins involved in the active transport, such as sodium-potassium pump (Na^+/K^+ ATPase), the transport of solutes through ion channels represents the fastest mechanism to exchange a large amount of ions in the shortest possible time. The reason for this is that, carriers and active transport proteins have specific binding sites, which can be occupied by the substrate (that is the ion), only when the protein is not carrying anything else across the membrane. In fact, during the capture and translocation processes the molecular structure changes, and the binding site, which is facing the same side of the substrate, becomes inactive; this means that they are not open simultaneously to the extracellular and intracellular environments.

In contrast, ion channels can be open to both cellular sides at the same time, allowing the solutes to flow passively through them without any additional input of energy, driven only by electrical (voltage) and chemical (concentration) gradients. This mechanism provides ion channels with a great advantage over other transport proteins and justifies the high rate of charged particles transported by ion channels. A single channel can transfer up to 10^8 ions per second from one side to the other of the membrane, that is, 10^5 times greater than any recorded rate of transport in carrier proteins, as reported in *figure 1.1*, where are also illustrated the three types of passive ion channels: voltage-gated, ligand-gated and mechanosensitive and the active transport proteins [21].

Ion channels are involved in manifold functions, but the main one is to participate directly in establishing a cellular homeostasis, allowing ion fluxes through cell membranes and creating a resting membrane potential, an electrophysiological cellular property common to both electrically excitable cells, such as muscular cells and neurons, and non-excitable ones. Moreover, they can also modify the membrane potentials in response to an external stimulus or a certain physiological cell condition, for example, shaping action potentials and other electrical signals by gating the flow of ions across the cell

membrane. In this way, they contribute to the electrical excitability of muscle cells and to the neural signaling in the nervous system, as well as control the flow of ions across secretory and epithelial cells and govern the electrolyte movements required for volume regulation of single cells and transporting of salts across epithelia [9].

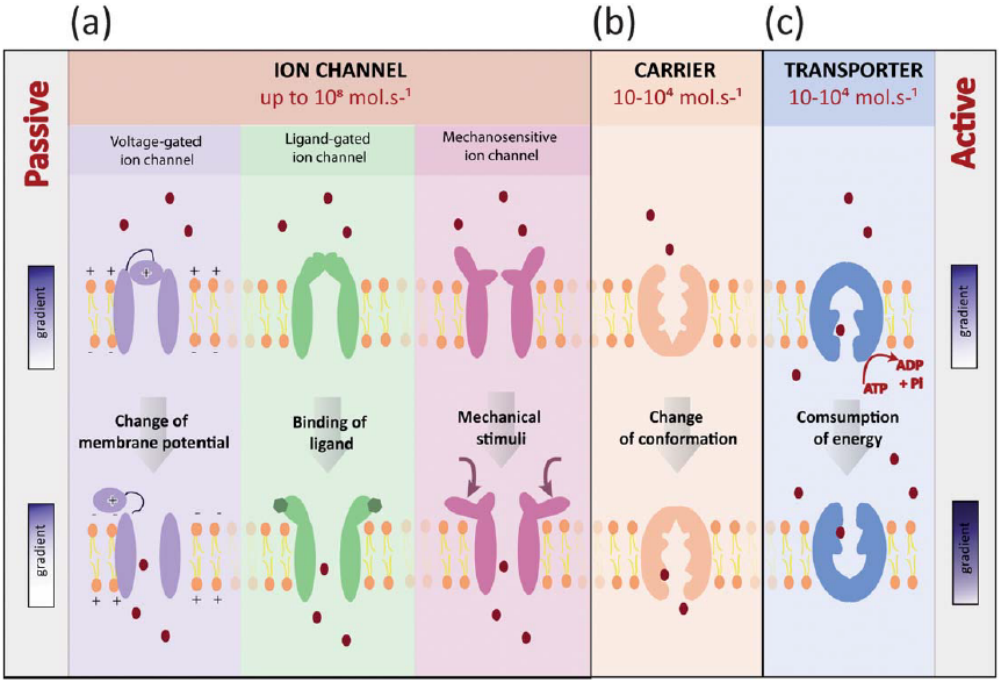

Figure 1.1: **Types of membrane proteins mediating translocation across cell membrane.** Passive ion channels (**a**) and carriers (**b**) are driven by a chemical gradient. Ion channels are classified into three groups according to their mechanism of opening: voltage-gated ion channels, that open after membrane depolarization, ligand-gated ion channels, that require binding with a ligand to be opened, and mechanosensitive channels open after a mechanic stimulation. (**c**) Active transport, instead, allows a transport against a chemical gradient, thanks to the consumption of energy, e.g. by ATP hydrolysis. Typical transport rates are also indicated [22].

1.1.1 Ion channels classification

As introduced in *figure 1.1*, there are many types of ion channels with different structure and properties, and each one is involved in particular functions or molecular network of the cellular machinery; a detailed description is given in the following overview:

- ***Voltage-gated (VG) ion channels.*** This superfamily of ion channels represents the third largest group of signaling molecules in humans (after the protein kinases and the G-protein coupled receptors, GPCRs). They are usually ion-specific and their opening and closing are triggered by modifications in the membrane potential, as a consequence of the variation of charged particles concentration between the two sides of the cell membrane. In general, they undergo conformational changes from a closed to an open state when cell membranes are depolarized or hyperpolarized. The three most important subfamilies of this kind of ion channels are sodium (human Na_v channels), potassium (human K_v and K_{ir}) and the calcium voltage-gated ion channels (human Ca_v). Other groups of VG ion channels have a more complex structure, they are gated by membrane potential variations, but are also modulated by secondary stimuli, that can be: chemical species (e.g. calcium ions, for the two-pore channels (TPC) [23] and for calcium-activeted potassium channels (K_{Ca}) [24], and nucleotides, for cyclic nucleotide- or hyperpolarized cyclic nucleotide-gated channels (CNG and HCN respectively [25, 26]), or even physical events, such as pressure or mechanical shocks, as for certain transient receptor potential (TRP) channels or two-pore domain potassium (K2P) channels [27, 28].

- ***Ligand-gated (LG) ion channels.*** Certain K^+, Cl^- and TRP channels are relatively voltage-insensitive, but are gated by secondary messengers or other intracellular or extracellular mediators. When a ligand-gated ion channel binds to a specific ligand, it induces a conformational change of the protein and the channel becomes active. The different

conformational states of the ion channels are related to different functional states: LG ion channels can be opened, closed or desensitized (closed without the possibility of being reactivated). Specific molecules, such as ions, neurotransmitters or hormones, increase the probability of the open state, changing the membrane permeability; therefore the functionality of the LG ion channels can be modulated by changings in the concentration of the amount of ligands.

- ***Mechanosensitive ion channels.*** Our knowledge of these kinds of ion channels, known also as stretch-gated (ST) ion channels, is limited. What we know is that they open after a pressure shock and are important regulators in osmotic sensing, motility and cellular migration, both in bacteria and eukaryotes. Various molecular mechanisms can be implicated in their activation. For example, in some cases the channel structure contains a domain, which binds to the lipid bilayer and acts as a spring, sensing the movement of the membrane. Thus, when the bilayer is stretched the open state of the channel is favored [22].

Interestingly, most of the human voltage-gated ion channels have bacterial homologues; this is a significant finding that confirms the important role in crucial life processes, such as motility, chemotaxis and pH homeostasis. For this reason, it is believed that these ion channels evolved from a common ancestor and have been classified as the voltage-gated-like (VGL) ion channels (*figure 1.2*) [29, 30].

Other ion channels, however, such as Cl^- ones and aquaporins, have completely different structural properties having evolved quite separately. Although our knowledge about structure and function of ion channels has tremendously increased over the last two decades, there is still a strong need for further research, especially for understanding their working mechanism and regulation, strictly involved in certain diseases and biological dysfunctions.

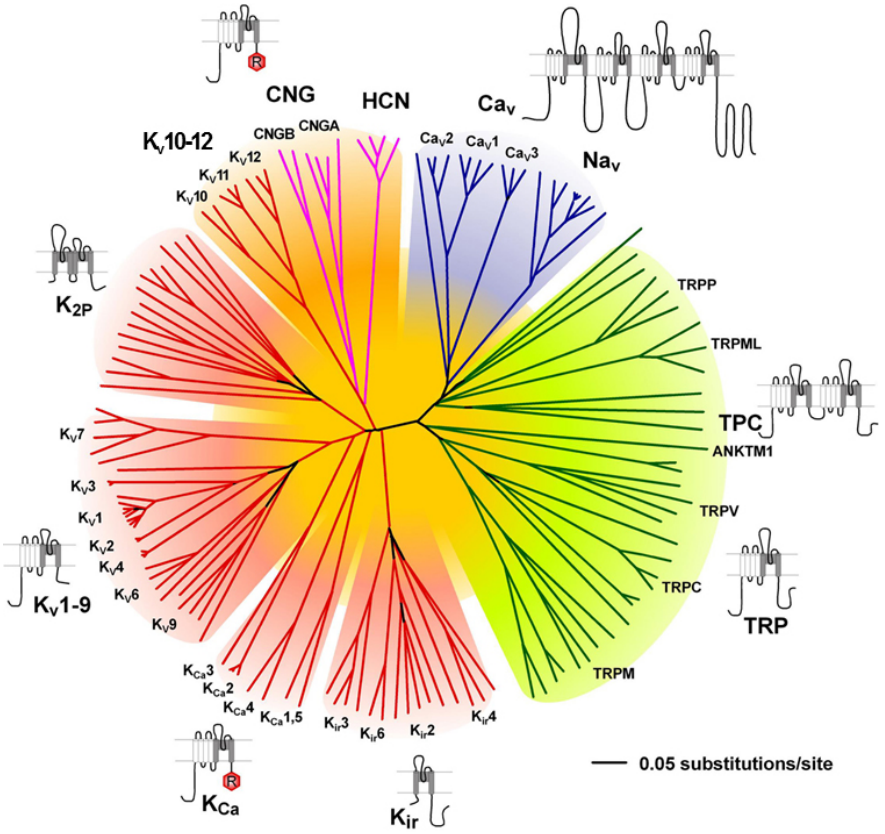

Figure 1.2: **Family tree of evolutionary relationship among human Voltage-Gated cation channels.** Dendrogram shows the different subfamily of cation channels distinguished by different colors [31].

1.1.2 Resting membrane potential

As a consequence of the ionic transport phenomena and the presence of proteins and nucleic acids within the cell, characterized by negative charges, the cytosol assumes a negative potential compared to the extracellular environment, where positive charges are more concentrated. This unbalanced distribution of electrical charges across the plasma membrane creates an electrical potential, which is the key to explain many cellular responses to external stimuli, such as, for example, cellular excitability or action potentials, in the case of neuronal cells.

In *table 1.1* are reported the intra- and extracellular concentrations of the main ions responsible for the membrane potential in a typical mammalian cell [9].

	$Concentration(mM)$	
Ions	Intracellular	Extracellular
Cations		
K^+	140	4-5
Na^+	5-15	145
Mg^{2+}	0.5	1-2
Ca^{2+}	0.0001	2.5-5
Anions		
Cl^-	4	110-117

Table 1.1: **Intra- and extracellular concentrations (mM) of the most common ions in a mammalian cell.**

The magnitude of the membrane potential depends on a specific ionic permeability and on the concentrations of ions on both the membrane sides. Ion channels provide specific ionic permeability, and their opening results in a flow of ions driven by their particular electrochemical gradient. This means that the membrane potential is governed by combined forces: diffusive forces, generated by a chemical concentration gradient, and electric forces, originated by the asymmetric charge distributions across the plasma membrane. The ionic steady state, characterized by constant ionic flows on either side of the cell membrane, defines the resting membrane potential and is maintained by the action of the sodium-potassium pump, which actively sustaines the correct ionic concentrations across the cellular compartments, as illustrated in *figure 1.3*.

Considering only the permeability for K^+, which is the most important ionic species in cellular electrophysiology, the membrane potential can be written by means of the Nernst equation:

$$E_{K^+} = \frac{RT}{zF} ln \frac{[K^+]_{out}}{[K^+]_{in}} \tag{1.1}$$

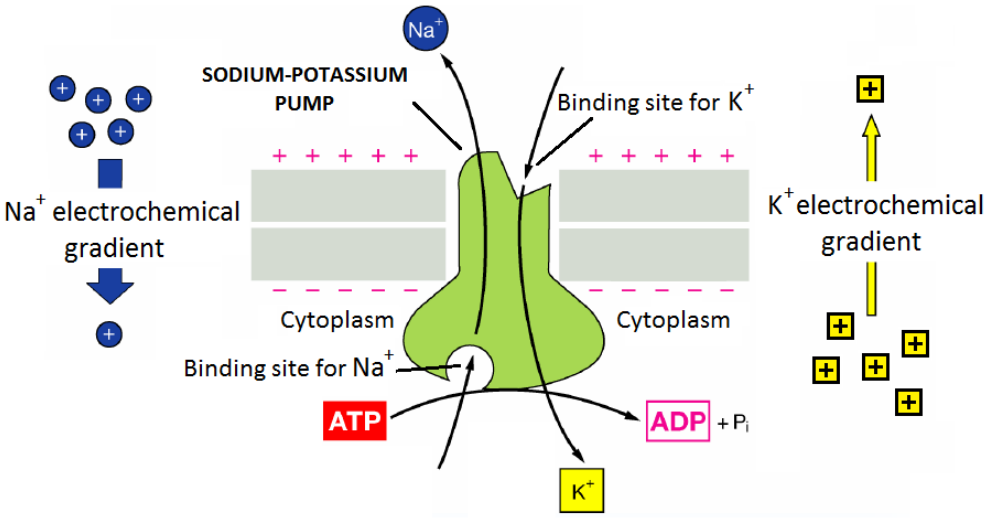

Figure 1.3: **Schematic representation of a sodium-potassium pump.** Na^+/K^+ ATPase allows the transport of three ions of Na^+ (blue circles) towards the extracellular compartment and two K^+ ions (yellow squares) towards the intracellular one, against their electrochemical gradients by exploiting the energy deriving from the hydrolysis of ATP molecules.

where: *in* and *out* stand for intra- and extracellular concentrations of K^+, z represents the ion charge, R is the universal gas constant, F is the Faraday constant, and finally T is the absolute temperature expressed in kelvin unit. The Nernst equation allows to calculate the equilibrium potential of a single ion, in this case K^+ (E_{K^+}), starting from the knowledge of its exact concentrations in the two cellular compartments. Therefore, E_{K^+} is positive when $[K^+]_{out}$ is greater than $[K^+]_{in}$ and negative when the ions, on the contrary, are more concentrated in the intracellular side. Instead if the ion is an anion the situation is inverted.

For many cells this approximation does not reflect a physiological condition; for example for neuronal cells the Nernst equation, considering only K^+ permeability, predicts a resting membrane potential of about -90 mV, while the actual potentials measured are about -60/-70 mV. This means that other ionic species, as for example Na^+, are involved in the regulation of the

cellular resting potential and, even if they have a permeability through the plasma membrane less significant than the K^+ one, they are able to shift the membrane potential towards more positive values.

A more accurate model to estimate the membrane potential is given by the Goldman-Hodgkin-Katz equation, which takes into account all the specific ionic permeability (p_i) of the plasma membrane:

$$E_m = \frac{RT}{F} ln \left(\frac{\sum_i^N p_i [{C_i}^+]_{out} + \sum_i^N p_i [{A_i}^-]_{in}}{\sum_i^N p_i [{C_i}^+]_{in} + \sum_i^N p_i [{A_i}^-]_{out}} \right) \tag{1.2}$$

In this formulation it is clear that cations (C^+) and anions (A^-) give opposite contributions in defining the membrane potential.

Furthermore, as previously observed in *table 1.1*, for mammalian cells the most important ions that affect the resting membrane potential are mainly: Na^+, K^+ and Cl^-, thus a good approximation of the membrane potential can be obtained by the Goldman-Hodgkin-Katz equation taking into account only these three ions.

Due to the ions movement the membrane potential (V_m) can be altereted from its resting state; in particular, the cells are said to be depolarized, when the V_m is altered to relatively less negative state, and are said to be hyperpolarized, when the V_m shifts towards more negative values than the resting membrane potential [32].

1.1.3 Electrical equivalent circuit of a cell membrane

As shown previously, at resting conditions, the membrane potential depends on the charge distributions across the plasma membrane. However, V_m changes in response to an electrical stimulation according to the electrical properties of the plasma membrane, such as ion permeability and conductance.

Passive electrical properties of a plasma membrane can be summarized, at first approximation, as an electrical circuit, composed by a resistor in parallel with a capacitor, both in electrical contact with a current generator,

which represents the external stimulus. In detail, the resistance is represented by the entire amount of ion channels expressed on the plasma membrane, and the capacitance is due to the phospholipid bilayer, which maintains the asymmetric distribution of charges, slowing their exchange through the membrane.

This means that a cell can be schematized as a parallel RC circuit, as shown in *figure 1.4A* and the value of the membrane potential follows Ohm's law $\Delta V_m = V_m - E = I_m R$, where E represents the resting membrane potential and I_m the total amount of current injected through the plasma membrane (*figure 1.4B top*).

Specifically, $I_m = I_r + I_c$, with I_r the resistive current and I_c the capacitive one, while R stands for the membrane resistance, which can be written in the approximation of a spherical cell of radius r. In this way R can be calculated as follows: $R = R_m/4\pi r^2$ where R_m is the specific membrane resistance depending on the number of passive ion channels opened at resting condition per unit area (Ωcm^2). Obviously, increasing the cell size, and hence its surface, R decreases with a quadratic law; this implies that for the same stimulus the variation of the membrane potential will be greater in small cells than in larger ones. Usually, in these mathematical models, it is preferred to refer to the electrical resistance through its inverse, the conductance $g = 1/R$.

As expected from this model, membrane potential reaches the steady state predicted by Ohm's law after a transient time, that depends on the time constant $\tau = RC$, which in living cells may range from $10\mu s$ to $10ms$. The value of the capacitance C depends on the amount of charges that can be accumulated across the plasma membrane as a result of a voltage difference following the law $C = \Delta Q/\Delta V$, as for an electric capacitor. Moreover, considering that the thickness of the plasma membrane is much smaller than the surface of a cell, the capacitance C can be estimated using the relation $C = \epsilon S/d$, resulting directly proportional to the cellular surface itself. However, generally, it is preferred to define a specific capacitance value per unit area: $C_m = 1\mu F/cm^2$, and, as done for the resistance R, write the total capacitance as $C = C_m 4\pi r^2$.

Thus, to obtain the real trend of V_m as a function of time, it is necessary to solve the differential equation:

$$C\frac{dV_m}{dt} + g(V_m - E) - I_m = 0 \tag{1.3}$$

which gives as solution for $V_m(t)$ the following function:

$$V_m(t) = u(t)V_s\Big[1 - e^{-(t/\tau)}\Big] + u(t)E\Big[e^{-(t/\tau)}\Big] \tag{1.4}$$

where $u(t)$ is the unit step function: it is zero when $t < 0$ and one when $t > 0$. On the other hand, after the current pulse, the RC equation is given by:

$$C\frac{dV_m}{dt} + g(V_m - E) = 0 \tag{1.5}$$

which gives as solution for $V_m(t)$:

$$V_m(t) = u(t)E\Big[1 - e^{-(t/\tau)}\Big] \tag{1.6}$$

In *figure 1.4 B (bottom)* are shown in detail different membrane potential trends of $V_m(t)$ resulting from diverse current step stimulations, according to equations 1.4 and 1.6. Note that, when no stimulus is applied the membrane potential assumes the value at resting conditions.

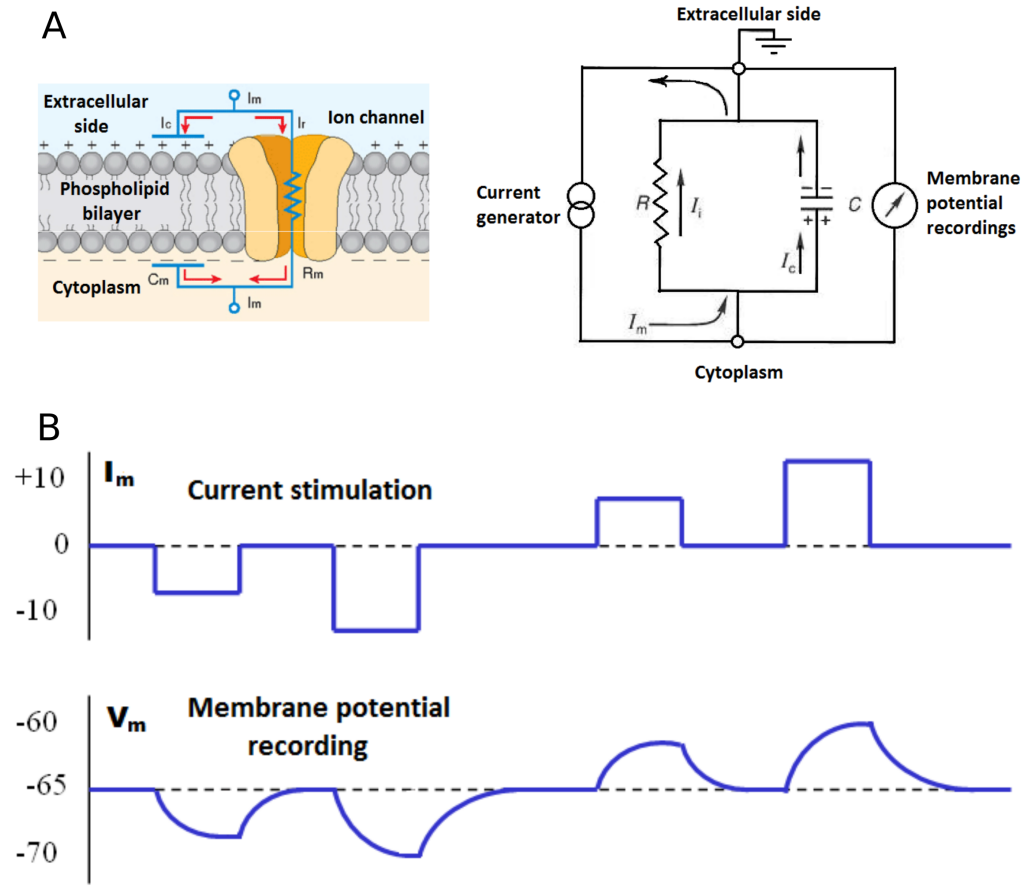

Figure 1.4: **Electrical equivalent of a cell.** (**A**) Schematic representation of the passive elements of a cell, where ion channels define the membrane resistance R, while the membrane itself defines the cell capacitance C. (**B**) Examples of V_m trends as a consequence of injected current stimuli I_m.

1.2 Voltage-gated potassium (K^+) channels

1.2.1 General considerations

Among the voltage-gated (VG) ion channels, VG K^+ channels are the most important ones in eukaryotic organisms because they participate in a large number of cellular functions, from the regulation of cardiac electrical patterns to signal transduction pathways. Furthermore, they are considered as a model in terms of the stucture, because it remains almost similar also in other types of VG ion channels.

The structure of a VG K^+ channel can be divided into two main parts: the pore-forming domain and the regulatory domain. The former is responsible for the K^+ ions transport inside the channel, while the latter senses the external stimuli and modulates the gating properties of the channel. Depending on the cell type, the regulatory domain can bind to auxiliary subunits that profoundly affect the channel physiological activity [33].

In *figure 1.5 (top panel)* is reported the main structure of a VG K^+ channel, based on the bacterial KcsA channel model. In detail it is classified as a homotetrameric channel because it is made by four identical transmembrane subunits, containing each one a voltage sensor and that surround a central pore. Each one of these subunits has six transmembrane crossings segments (S1-S6), that present an amino (N-) and a carboxy (C-) terminal group, placed both on the intracellular side of the membrane.

The selectivity filter, i.e. the ion conduction pathway, is placed in the inner part of the pore and is formed by a loop between the S5 and S6 segments; the voltage sensor includes the S4 region with its multiple positive charges. The four spheres at the top of the channels indicate the four K^+ ion binding sites, which are in general occupied alternately by K^+ ions and water molecules. The four inner helices (one for each subunit) cross the protein and give it the correct three-dimensional morphology, which represents a critical parameter for proteins, functionality; in addition, they create a water-filled cavity at the central region of the channel, necessary for the flow of K^+ ions.

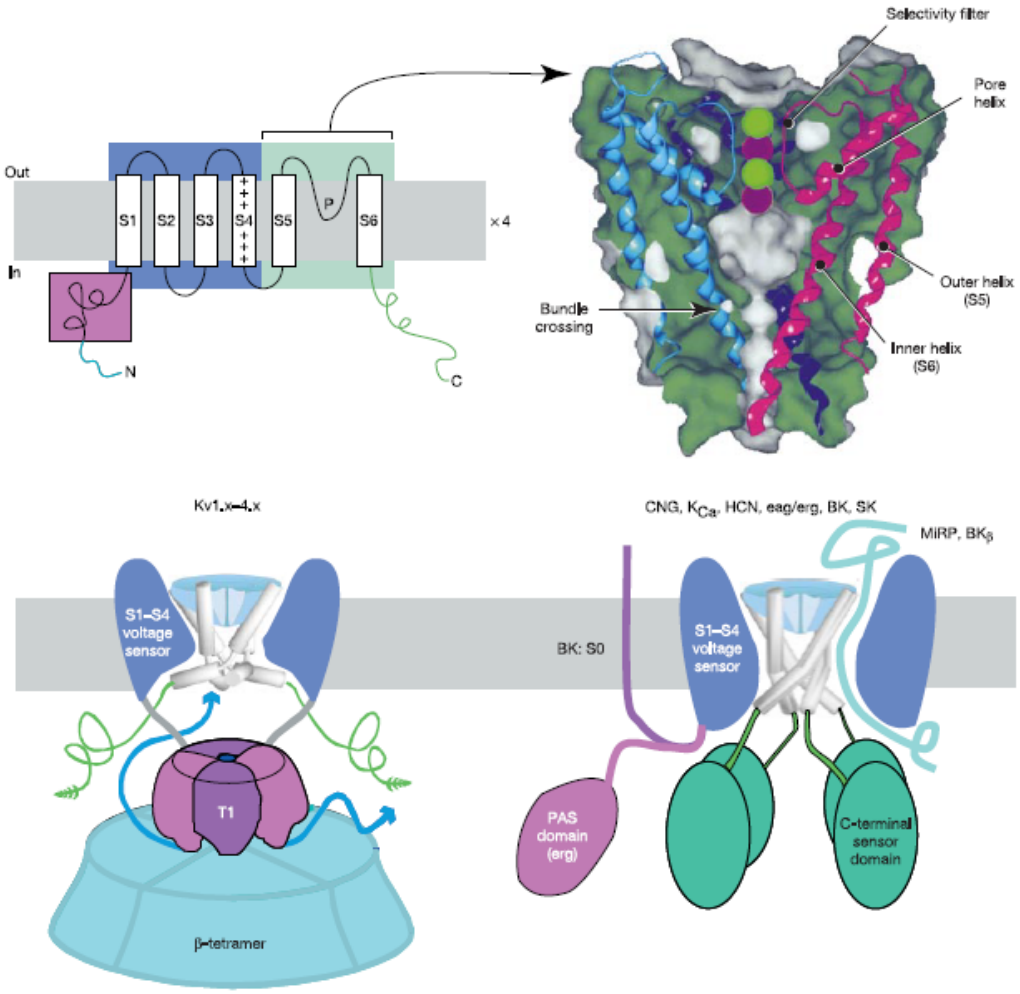

Figure 1.5: **Examples of structures of potassium channels.** In the top left panel is represented one of the four identical subunits of a typical K^+ channel, each one characterized by six transmembrane segments: the sensor region (S1-S4) and the selectivity filter (S5-S6). On the right the spatial organization of the secondary protein structures is depicted: in dark green the inside of the protein, in grey the water-exposed surface. In the bottom panel are illustrated two mechanisms of channel regulation through auxiliary specific subunits; the first one is an example for the K_v channels family (left), while the second one, is a characteristic representation of a potassium Ca^{2+}-activated (BK_{Ca}) channel (right). Picture from G. Yellen, 2002 [34].

In the bottom of *figure 1.5* are showed two mechanisms through which accessory subunits are able to regulate channel activity. The core of some K_v channels subfamilies (*figure 1.5*, lower left panel), for example, has at its N terminus a tetramerization domain (T1, purple) that serves as a platform for the attachment of the optional β-subunits, as well as for other protein-protein interactions. The binding of the channel with other subunits has the function to modulate its activity and is considered directly involved in intracellular signaling processes. Other tetrameric K^+ channels, as potassium Ca^{2+}-activated (BK_{Ca}) channels, have a different domain structure, characterized by the absence of a T1 domain and the presence of a sensor domain in the C terminus (*figure 1.5*, lower right panel). In this channel, the C-terminal sensor domains adopt a four-fold symmetrical organization and the N terminus have an additional transmembrane sensor domain (S0). The auxiliary subunit associated with this class of K^+ channels crosses the membrane, and appears to be intimately associated with the pore region, interacting directly with the voltage-sensor domain [34].

1.2.2 A closer look to the molecular structure

The molecular structure of a VG K^+ channel is characterized by a different dislocation of charges near both the intracellular and extracellular sides of the protein, due to the presence of electrically charged amino acids, as illustrated in *figure 1.6*, where amino acids with negative charge, typically Aspartic acid (*Asp*) and Glutamic acid (*Glu*), are depicted as red regions, while basic amino acids with positive charge, as Arginine (*Arg*) and Lysine (*Lys*), are in blue.

As expected for a cation channel, negative amino acids are localized near the pore, while positive ones are present in the peripheral regions of the channel. Clearly, this causes variations in the local concentrations of ions, favoring the accumulation of positive ions at the pore region of the protein, including K^+ ions.

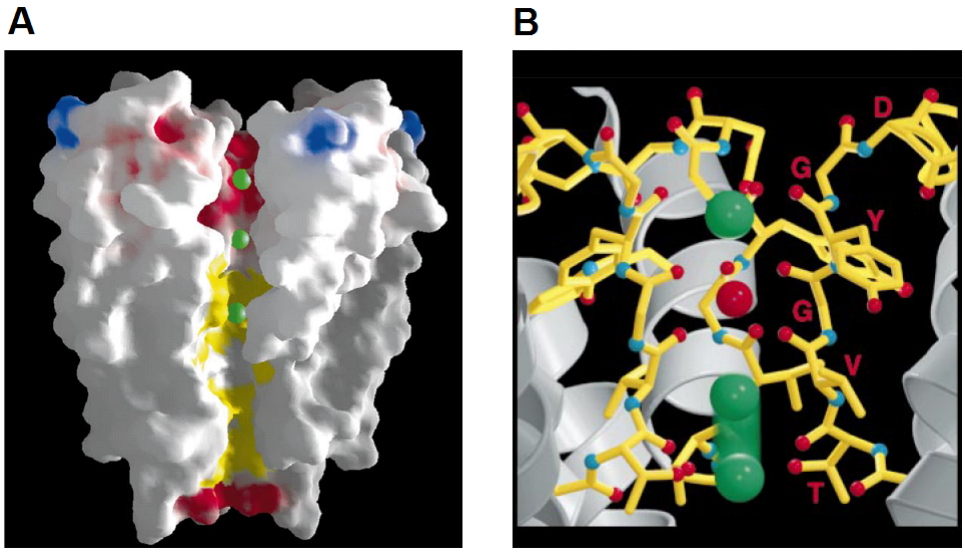

Figure 1.6: **Microscopic structure of a potassium channel.** (**A**) Section of the inner part of a K^+ channel displaying the solvent-accessible surface of the protein colored according to physical properties of the region of interest; red for negative charged amino acids, blue for positive ones, yellow for hydrophobic walls of the pore tunnel and green for the spheres representing the K^+ ion positions in the conduction pathway. (**B**) Focus on the selectivity filter region of the channel pore. The four subunits of the channels are characterized by the same specific amino acids sequence: *Thr, Val, Gly, Tyr, Gly* running from bottom to top. Two K^+ ions (green) are located at opposite ends of the selectivity filter, with a single water molecule (red) in between. The filter is surrounded by inner and pore helices (white) [14].

The overall length of the pore is about 45Å, while its diameter varies depending on the position considered. From the intracellular side, the pore begins as a tunnel of 18Å in length and then opens into a wide cavity near the middle of the membrane. This allows to the K^+ ions to move throughout the internal pore and cavity remaining mostly hydrated, lowering the electrostatic barriers without creating energy wells. Contrarily, the selectivity filter region is so narrow that a K^+ ion is forced to separate from water molecules to enter inside the channel.

The chemical properties of the wall that covers the internal pore and cavity give it a hydrophobic behavior (yellow in *figure 1.6A*); as a consequence there are no particular electrostatic interactions inside the pore tunnel.

As shown in *figure 1.6B*, the selectivity filter consists of a specific sequence of amino acids: Threonine (*Thr*), Valine (*Val*), Glycine (*Gly*), Tyrosine (*Tyr*), Glycine (*Gly*), known as *T-V-G-Y-G* sequence. The amino acids *Thr* and *Gly* are oriented in such a way to expose the oxygen atoms of their carbonyl groups to K^+ ions; this progressively leads to replace the bonds with the eight molecules of water (i.e. the K^+ hydration shell), with the oxygen atoms themselves, favoring the transit of K^+ ion within the selectivity filter.

Val and *Tyr* at the same time establish hydrogen bridges with the amino groups of the inner helix and pore helix, to maintain the correct geometry of the pore. This structural configuration is very important because it is at the origin of the selective properties of the channel, being able to exclude the smaller alkali metal cations, such as Li^+ (radius 0.60 Å) and Na^+ (0.95 Å), but allows the passage of the larger members of the series, as Rb^+ (1.48 Å) and Cs^+ (1.69 Å). In fact, Rb^+ is nearly a perfect K^+ (1.33 Å) analog, because its size and permeability characteristics are very similar to those of K^+. Furthermore, this well-defined electrostatic structure plays a key role also in the mechanisms that control the channel block.

1.2.3 Gating mechanism of a voltage-gated K^+ channel

Different mechanistic models have been proposed to describe how transmembrane segments could couple with the electric field to gate ion channel conduction. During the years, many studies have been conducted to demonstrate that voltage-gated ion channels have a specific region in each subunit, which is able to sense changes of the plasma membrane potential. These voltage-sensing domains act by shifting these proteins between activated and deactivated states, in response to changes in transmembrane voltage.

The main element of this structure is the fourth transmembrane region (S4), which has, at every third position, a positively charged Arginine or Lysine residue, which confer it the possibility to sense external electrical stimuli, leading to fluctuations and conformational changings within the plasma membrane. In fact it was observed that spontaneous or biochemically induced mutations of the S4 chain (obtained for example by replacing a positive charged residue with Cysteine), negatively affect the gating capability of the channel [34, 35, 36, 37, 38].

More recently, to explain the gating process has been proposed a detailed model based on six different steps, confirmed by several experiments and previous findings, as shown in *figure 1.7*. In particular, beginning with the activated state (state 1), in response to a hyperpolarizing stimulus, conformational changes occur that lead to ion depletion, hydrophobic dewetting, and the pore cavity closure, with concurrent early gating-charge inward movement, that block ionic conduction. As a consequence, the S4 segment is forced to move inwardly by ~ 15 Å relative to the largely rigid voltage sensing domain (VSD) core. At the same time a $\sim 120°$ rotation of S4 occurs, that keeps the gating-charge residues pointed toward the VSD lumens, leading to a lateral VSD-pore loosening, and then a subsequent full VSD relaxation, which permits the pore to remain closed, resting condition (state 4). A depolarizing stimulus reverses these steps. The key difference is that all the four VSD must be up before the closed pore can reopen; a fully outward S4 perturbs the S4-S5 linker/S6 packing, thereby allowing water, and hence ions, reentry and subsequent conduction, stabilized by linker/S6 repacking [39].

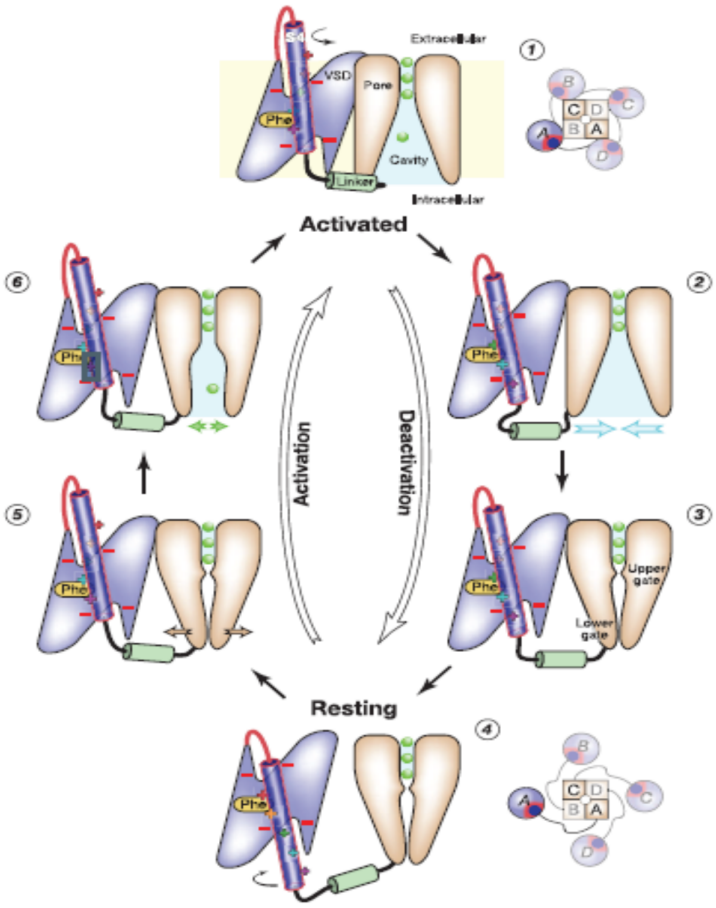

Figure 1.7: **Six-states model of gating process for a VG channel.** Starting from the activated state (1), ion depletion of the pore cavity, together with an inward motion of a single S4 segment, leads to a hydrophobic collapse of the pore tunnel (2). Closure of upper and lower gates arrests ion conduction (3). As S4 completes its inward motion, the S4-S5 linker helix moves fully down and the voltage sensing domain (VSD) loosen from the pore, consolidating the resting state (4). Subjecting the resting state to depolarizing voltage drives S4 outward. When all the four S4 and S4-S5 linker helices are fully up (5) and all VSD repack against the pore, the lower gate becomes destabilized. These fluctuations trigger pore opening and partial pore rehydration that allow ion entry and initial conduction (6). The presence of ions drives complete pore rehydration that pushes fully open the upper and lower gates, returning the channel to the activated state (1) [39].

1.2.4 Pharmacological block of K^+ channels

Characterizing the bioelectrical properties of a cell means to be able to identify the different ionic flows involved in the cellular response to an electrical stimulus. Recognizing the main types of ion channels expressed on the plasma membrane and understanding how they work can be very difficult. In addition to this, the great intrinsic variability of biological samples must be taken into account. For example, some channels become active only under certain physiological conditions of a cell, while others show a cell-dependent behaviour and their expression depends on the particular cell type.

One of the most useful approaches is to rationally proceed with pharmacological treatments, that are able to selectively block only some well-defined ion channels, leaving the others unaltered.

Focusing our attention on K^+ channels, one of the most effective pharmacological blocker is the quaternary ammonium cation, Tetraethylammonium (TEA), which acts suppressing the outward potassium current in a non-specific way [40]. The inactivation mechanism is due to the fact that this charged molecule has similar properties to the N-terminal chain of the channel; this means that it shows a specific affinity for some hydrophobic amino acids located at the pore region, binding to the channel and blocking the potassium flux. Due to steric effect, TEA affects the channels that are initially open and then it is able to block voltage-dependent ion channels that result activated in the cellular resting state or those forced to become activated consequently to a depolarizing stimulus.

Other potassium blocking agents are more specific and are able to inactivate only some types of channels. An example is Iberiotoxin (IbTx), a neurotoxin of 37 amino acids extracted from the scorpion venom, which represents one of the most powerful blocker of large conductance Ca^{2+}-activated potassium (BK_{Ca}) channels [41]. In this case, the occlusion of the channel is mainly due to electrostatic interactions between the negative charges, localized at the channel entry, and the positive ones located on some amino acidic residues of the toxin sequence. Another interesting blocker is Dendrotoxin (DTx) that,

like IbTx, is a neurotoxin, isolated in 1980 by green mamba poison; this is a small protein of about 60 residues that contains amino acids positively charged, such as Lysine and Arginine, able to interact with the negative charges of the channel, causing a conformational change that prevents its functionality [42]. This electrostatic interaction between the blocker and the ion channel creates aggregates that physically block the entrance of the pore tunnel.

The inactivation mechanism presented for all these blocking species is mainly mechanical and their effect is concentration-dipendent, as increasing the blocking agent concentration corresponds to an increase of the effect. For this reason, to have a significant effect, it is generally useful to work with saturating concentrations of blockers, that is, 10 mM for TEA and 100 nM for IbTx and DTx. In *Table 1.2* are reported the main types of K^+ channels on which the above-discussed blockers have the greatest effect at the indicated concentrations [43].

TEA $(10mM)$	$IbTx$ $(100nM)$	DTx $(100nM)$
Ca^{2+}-activated K^+	BK_{Ca}	$K_v1.1$
$K_v1.1$		$K_v1.2$
$K_v1.6$		
$K_v2.1 - K_v2.2$		
$K_v3.1 - K_v3.4$		

Table 1.2: **Blocking soliution for K^+ channels.** Specific K^+ channels blocked by tetraethylammonium (TEA), iberiotoxin (IbTx) and dendrotoxin (DTx) at standard working concentrations.

1.3 K^+ channels and cell functionalities

Among the large family of ion transport proteins, K^+ channels are probably the ones that have the greatest importance in terms of their roles in cell

machinery; in fact, depending on the specific cell type, localization on the plasma membrane and other regulatory factors, K^+ channels participate actively in the regulation of manifold cellular functions, and therefore, are involved in several fundamental processes, as described in *figure 1.8*. For these reasons they represent interesting targets for which a therapy could be designed in pathological states, particularly in the treatment of cancer and, specifically, in counteracting metastatic processes.

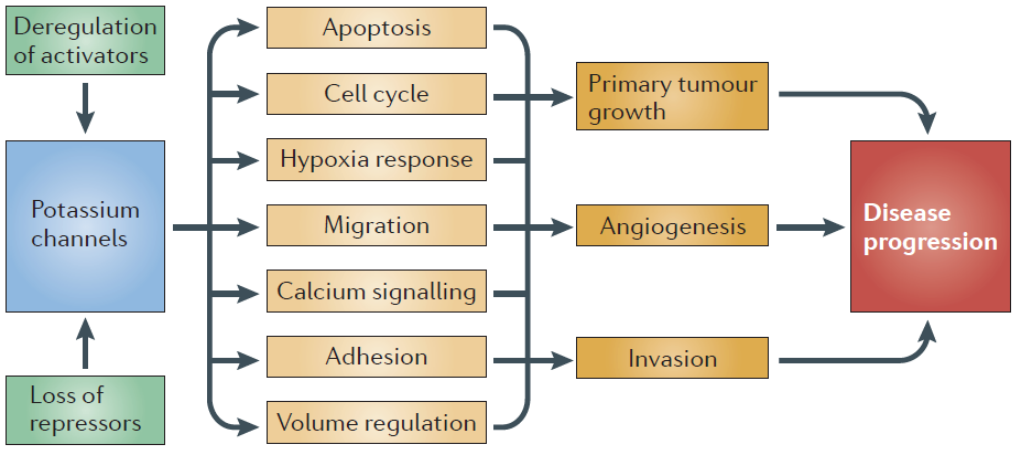

Figure 1.8: **Summary of the roles of K^+ channels and correlation with progression of pathological conditions.** Changes in the expression levels of K^+ channels can occur at different levels of the DNA transcriptional mechanism and in some cases, a quantitative increase in activity can be explained by upstream changes. Furthermore, K^+ channel activity can be increased by other factors (hormones or growth factors) and can be reduced by chromosomal aberrations that lead to reduced channel expression levels. These changes can have substantial effects on cellular processes such as cell adhesion, proliferation, migration and death, and can influence, at the same time, the occurrence and progression of cancers [44].

1.3.1 Cell adhesion and migration

Eukaryotic cells represent the minimal structural units that define living organisms. By proliferating, moving and mechanically interacting with

neighboring cells, they can organize themselves in complex organizations, such as tissues, organs and finally multicellular living organisms, composed of billions of single cells. Living cells actively sense and respond to the environmental stimuli around them, which may be chemical, electrical or mechanical.

Cell adhesion is an example of a biological process that, besides the intrinsic molecular mechanisms, depends strictly on the mechanical properties of the surrounding environment. The external stimuli induce the generation of intracellular contraction forces that drive the cell spreading, by using a mechanism based on the conversion of physical signals into biochemical signaling events. This mechanotransduction process is involved in manifold cellular functions, such as proliferation, motility and tumorigenesis.

Cell migration is another highly complex and multistep process intimately linked to the adhesion one, in fact they share several common features, structures and pathways, including surface receptors, signaling molecules, and cytoskeleton remodelling. The eukaryotic cytoskeleton, in particular, is the cellular basic structure, composed by three main kinds of protein fibers: actin-filaments, microtubules, and intermediate filaments. The combination of these molecular elements creates a complex, highly organized and dynamic structure that gives to the cell fundamental physical properties, such as its shape, elasticity and mechanical resistance to deformations, which is actively involved in the migration function.

In particular, to migrate, a cell has to acquire a characteristic polarized morphology in response to extracellular signals. This process can be summarized into four steps:

1. actin assembling localized at the cell front drives the extension of flat membrane protrusions called lamellipodia;

2. single fingerlike extensions (filopodia) develop from the cell membrane to sense the environment;

3. at the leading edge of the lamellipodium, the cell forms adhesion complexes, termed focal adhesions, mediated by transmembrane protein receptors, as integrins, that connect the extracellular matrix (ECM) to the actin cytoskeleton, anchoring the protrusions and holding the cell body;

4. the forces produced by the contractile network, due to the combined action of actin filaments and focal adhesion disassembly help to retract the trailing cell edge.

The morphology of a moving cell is described in *figure 1.9A*, where is also represented the cell studied with the immunofluorescence technique, that is a common practice in biology to highlight the different structural proteins involved in defining the morphology of migrating cells (*figure 1.9B*).

Through these main steps, a cell is able to combine the activity of retrograde actin movement with the contractile forces produced by stress fibres, generating the needed tension to pull its body forward [47].

In this contest, K^+ channels are important components of the cellular adhesion machinery and play a key role in driving cell polarization and migration. A significant proof is that, when specific blocking molecules inhibit these channels, migration is impaired [48]. Diverse explanations have been proposed about the mechanism through which K^+ channels may influence the process of cell migration, including the regulation of cell membrane potential and volume (see *figure 1.10*).

As previously shown, K^+ channels control actively the driving force for the electrogenic transport of ions across the plasma membrane, regulating the membrane potential. For example, it was observed that, depolarizing the plasma membrane by elevating the extracellular K^+ concentration, migration can be inhibited [49].

Migration is also a Ca^{2+}-dependent process; in fact the control of electrical driving force represents a critical parameter for Ca^{2+} fluxes and its intracellular concentration [50, 51]. In detail, intracellular Ca^{2+} concentration is involved in actin filaments polymerization and depolymerization process,

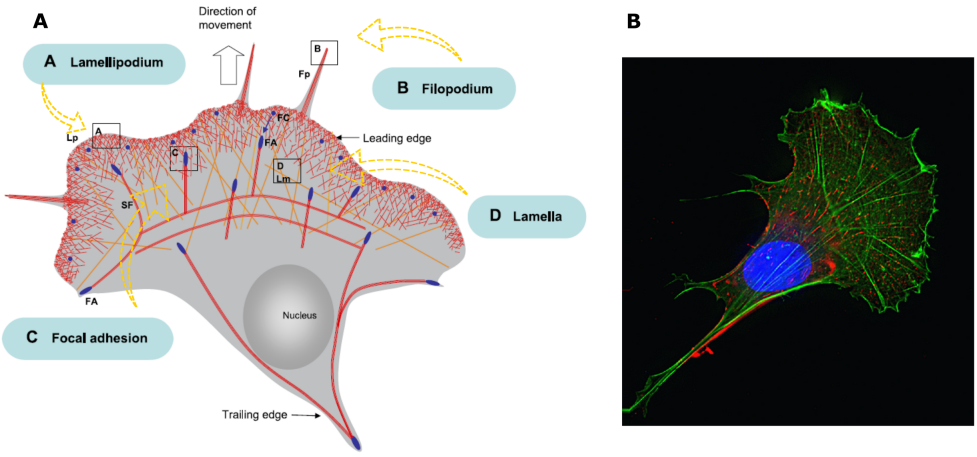

Figure 1.9: **Morphology of a migrating cell.** (**A**) Description of structural elements involved in cell motility: Lamellipodia (Lp; A), Filopodia (Fp; B), Focal adhesion complexes (FA; C) and Lamellae (Lm, D) (picture adapted from Le Clainche and Carlier, 2008 [45]. (**B**) Immunocytochemistry helps to highlight morphological structures of a migrating cell: cellular nucleus (blue), actin filaments (light green), representing the stress fibers along which the cell transports the mechanical stimuli, and fibronectin (red), which is an important extracellular matrix protein involved in cell adhesion, growth, migration and differentiation (picture from the "Cell and Molecular Biology Laboratory" of the Hand and Upper Limb Centre (HULC) in London [46].

coordinating the retraction of the rear part of migrating cells with forward protrusions [48]. The membrane potential acts on Ca^{2+} influx mainly in two ways, depending on the expression pattern of channels in the respective cell type: i) setting the electrical driving force required for Ca^{2+} to enter the cell; ii) controlling the gating behaviour of particular voltage-gated Ca^{2+} channels (*figure 1.10A*).

As mentioned, migrating cells undergo dramatic changes of their morphology while they move, generated by a sort of delay between the retraction of the rear part of the cell, compared to the development of the front one, and resulting in an intermittent local swelling of the protruding lamellipodium and shrinkage at the rear part, caused by the combined activity of ion channels and osmotic pressure changings (*figure 1.10B*).

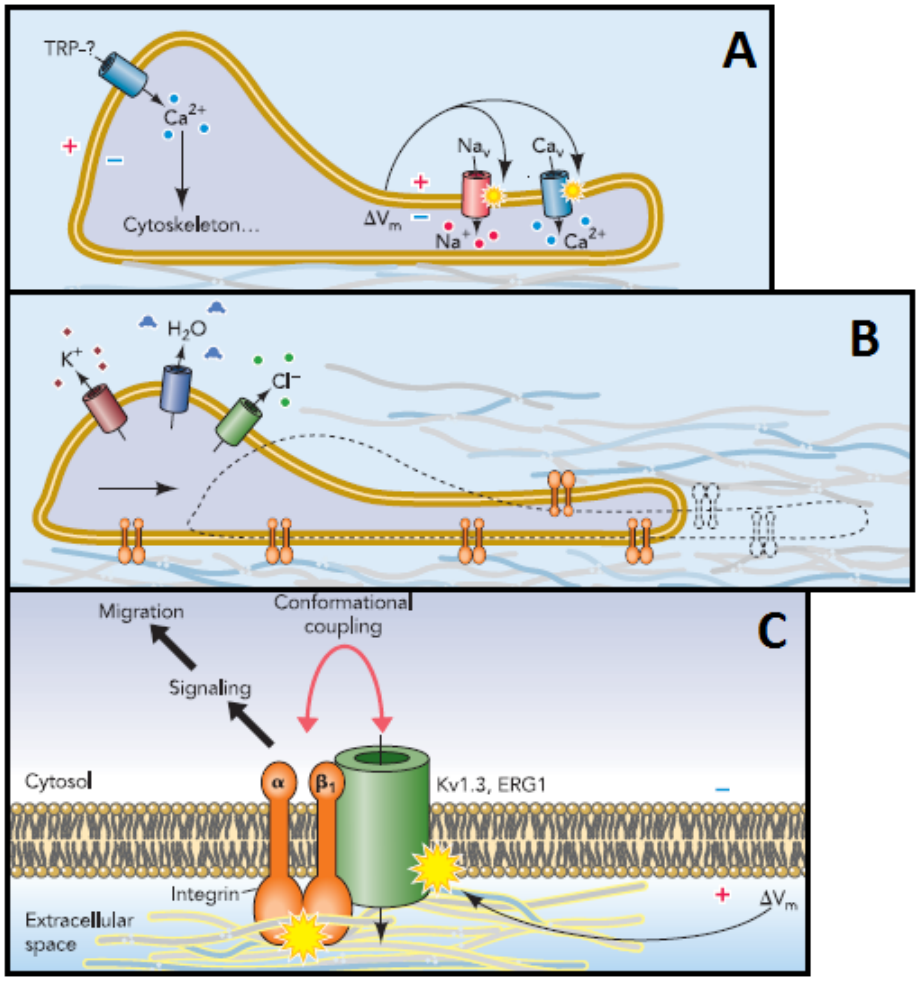

Figure 1.10: **Hypothesis of K^+ channel involvement in cell migration.** (**A**) K^+ channels, controlling the cell membrane potential (V_m), regulate the electrical driving force for Ca^{2+} influx via Ca^{2+} channels. Furthermore, changes of the cell membrane potential (ΔV_m) affect the gating behaviour of voltage-gated Na^+ channels and Ca^{2+} channels. (**B**) K^+ channels play a key role in cell volume regulation. They, cooperating with other channels, can induce a localized cell shrinkage that supports the retraction of the rear part of migrating cells. (**C**) K^+ channels interact with important components of the cellular migration machinery such as integrins. Conformational coupling of K^+ channels and integrins provides the basis for the reciprocal regulation of these proteins. Their mutual activation is required for an efficient cell migration [48].

Reasonably, swelling and shrinkage become very important for moving cells when they have to cross narrow spaces between other cells or within the extracellular matrix, such as in the metastatic process; this was observed in glioma cells invading brain slices [52], a particular family of brain tumor cells, that includes the cell line used as an *in vitro* model in the experiments described in this work.

The correct regulation of the cell volume by K^+ channels represents another important factor for cytoskeleton remodelling mechanism, since swelling leads to actin depolymerization, whereas cell shrinkage promotes actin polymerization [53], creating optimal intracellular conditions required for the cytoskeletal migration machinery.

Voltage-gated K^+ channels, are known to interact directly with proteins that are crucial for cell focal adhesion, such as: integrins [54], cortactin [55], and tyrosine kinases (FAK) [56]. The functional interaction between K^+ channels and these proteins in many cases is mutual. Recent evidence suggests that integrins can regulate ion channels, forming macromolecular complexes. When associated with these protein, K^+ ion channel functionality becomes more complex, because it is regulated by extracellular signals (through integrins), but, at the same time, the channel is also able to control integrin activation and/or expression, by creating a link between the intracellular environment and the external one, promoting or not cell adhesion [15] (*figure 1.10C*).

1.3.2 Cell galvanotaxis

Galvanotaxis is the ability of a cell to actively move in response to electric fields. Many hypotheses have been proposed to interpret galvanotactic behaviour of cells over the years, but the mechanism is not yet well understood. Galvanotaxis is a complex process that represents the collective outcome of various contributing mechanisms, including: asymmetric ion fluxes, preferential activation of voltage-gated ion channels, and electrophoretic redistribution of membrane components. Furthermore, we know that galvanotaxis requires

the same cytoskeletal rearrangements needed for cell motility, i.e. elongation of actin filaments, formation of adhesive contacts through integrins, binding with protein of the extracellular matrix (ECM) and, finally, contraction, driven by myosin II [57]. This myosin-based mechanism represents the most common molecular motor of muscle and non-muscle cells and it is regulated by intracellular calcium concentration ($[Ca^{2+}]_i$), because it plays an important role in polymerization and depolymerization of actin filaments.

According to these observations, it was demonstrated that cells respond actively to changes in $[Ca^{2+}]_i$, showing that, when subjected to a direct current electric field (dc EF) they displace themselves following the high to low $[Ca^{2+}]_i$ gradient [58]. In this model it is hypothesized a redistribution of intracellular Ca^{2+} as a sort of "Ca^{2+} wave" inside the cell, which produces the contraction of the anodic side, thereby propelling the cell towards the other direction, as represented in detail in *figure 1.11*.

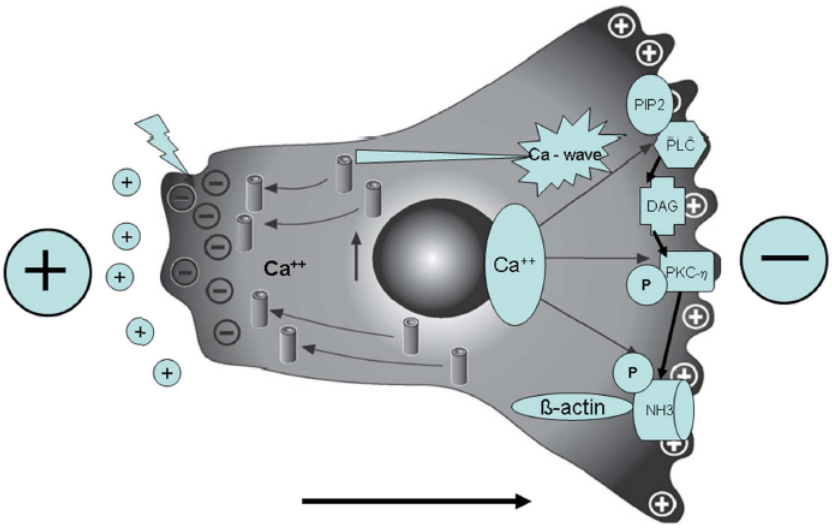

Figure 1.11: **A cell with negligible VGCCs conductance exposed to a dc EF.** The membrane towards the anode is hyperpolarized and attracts Ca^{2+} by passive electrochemical diffusion. Consequently, this side of the cell contracts, thereby propelling the cell towards the cathode. Picture from Richard H. W. Funk et al., 2015 [58].

As a consequence of the EF applied, ions and molecules negatively charged migrate and accumulate in the region of the cell towards the anode, then the plasma membrane changes its polarization state and becomes hyperpolarized. This leads to an inflow of calcium ions due to the increased electrochemical gradient, resulting in a localized contraction of this part of the cell; thus, the detachment of the rear part, favours the forward push of the cell towards the cathode. This model is valid especially for cells with negligible voltage-gated Ca^{2+} channels (VGCCs) conductance.

Instead, when cells show a high expression of voltage-gated ion channels on their plasma membrane, including also VGCCs, the effect observed is different; in fact, in this situation, channels near the cathode are stimulated to open, as a consequence of the depolarization of this side of the membrane, allowing Ca^{2+} influx. In such a cell, intracellular Ca^{2+} levels increase on the anodal side, as well as on the cathodal one, and the direction of cell movement, if present, depends on the balance between electro-osmotic forces [59]. In *figure 1.12* is presented a panel that explains this situation in detail.

However, the cytoplasmic Ca^{2+} concentration is actually regulated by other mechanisms, e.g. by local availability of calcium ions in special vesicles inside the cell, or indirectly by other ion channels. Thus, it is clear that, the understanding of bioelectric phenomena represents a critical step to try to explain the galvanotactic capability of cells.

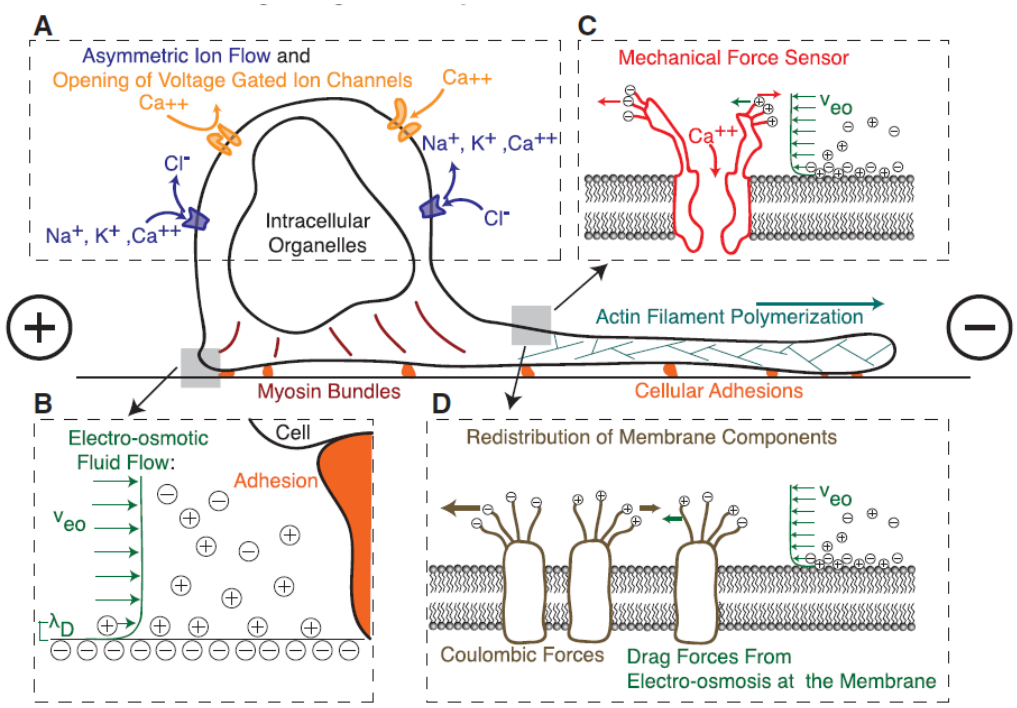

Figure 1.12: **Model of a cell characterized by voltage-gated ion channels exposed to an electric field.** (**A**) An electric field polarizes the cell changing electromotive forces and opening/closing voltage-gated ion channels. (**B**) Electro-osmotic flow, at the charged migration surface applies external force on the cell, which could for instance displace adhesions laterally. (**C**) Electro-osmotic forces created by the relatively immobile charged ions in the cell membrane attracting a mobile double layer at the cell surface combining it with electrostatic forces on charged macromolecules and membrane components to produce mechanical work. As depicted, this could asymmetrically activate a force sensor creating a local signal that could be used to define the front and the back of the cell. (**D**) Local electro-osmotic and electrostatic forces at the cell membrane also electrophorese membrane components. Negatively charged components move to the anode, and positively charged components migrate to the cathode. Electro-osmotic forces at the membrane also act to push proteins to one side of the cell or the other depending on the net surface charge of the cell. Picture from G. M. Allen et al., 2013 [60].

1.3.3 Cell proliferation

Cell proliferation is a complex and well-synchronized event, stringently regulated by many factors, such as: ions, molecules and proteins associated with the cell cycle machinery, including Ca^{2+}, ATP and many other cell cycle regulators [61].

Recently, ion channels have been recognized to play an important role in cell proliferation, becoming interesting targets for studying cancer initiation and progression. Voltage-gated K^+ channels contribute significantly to cell mitotic biochemical signaling and cell cycle progression, in physiological as well as in pathological conditions, leading to a cell proliferation success, when the cellular machinery works correctly, or, contrarily, to replicative defects, such as cell cycle arrest, senescence or apoptosis. As seen for the cell adhesion process, the appropriate adjustment of the cellular volume, the regulation of cytosolic Ca^{2+} concentration and the modulation of the cell resting membrane potential represent crucial factors involved in the cellular replicative mechanisms [62, 63, 64].

In particular, it was demonstrated that during cell cycle transitions, multiple families of voltage-gated K^+ channels become active, including outward rectifying channels (K_{ir}) and Ca^{2+}-activated K^+ (BK_{Ca}) channels [65, 66]; moreover their expression or activity changes across stages of the cell cycle [67]. This is true also for malignant cells, including metastatic ones, in fact it was observed that the set of ion channels expressed on their plasma membrane, as well as their functionality, change as a consequence of the oncogenic process, if compared to the healthy ones [68, 44].

These modulations contribute to hyperpolarize and depolarize the plasma membrane, resulting in rhythmic oscillation of the membrane potential during the cell cycle, with a consequent effect on it (*figure 1.13*).

As a confirmation of this, it was observed that cells with a hyperpolarized resting potential, such as muscle cells and neurons, in general show a negligible mitotic activity; while highly proliferating cells, as cancer cells, have a depolarized membrane potential in comparison to normal ones.

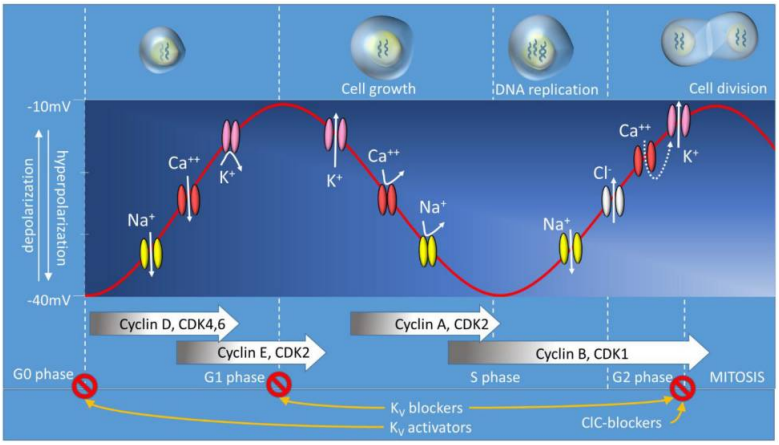

Figure 1.13: **Involvement of different voltage-gated ion channels during the cell cycle.** The activity of particular voltage-gated ion channels moves positive charges from the extracellular space to the cytoplasm, causing the depolarization of the membrane. This event appears to be essential to promote the transition from the G_0/G_1 phase to the S phase of the cell cycle. In contrast, membrane potential during the S phase tends to repolarize due to the opening of K^+ channels. Mitosis is associated with more depolarized membrane potential and is favored by an increase of cytosolic Ca^{2+} concentration. Depolarization and augmented Ca^{2+} entry allow the stimulation of Ca^{2+}-activated K^+ (BK_{Ca}) channels, which are responsible for water leaving the cytoplasm, resulting in a cell shrinkage before cell division. Picture from V. R. Rao et al., 2015 [69].

For example, in sarcoma cells it was observed that V_m undergoes a transient hyperpolarization before entering in mitosis (M) phase, followed by a rapid depolarization through the M phase, suggesting that V_m varies through the cell cycle progression; furthermore, lowering the V_m to a hyperpolarized state similar to that of neurons leads to a mitotic block in certain proliferating cells, while a sustained depolarization can induce DNA synthesis and mitosis [69].

Moreover, studing a breast cancer cell line, it has been noted that, during the cell cycle progression, V_m is correlated with the transition of each phase: the pharmacological arrest of cells in G_1/S or G_2/M transition results in a

hyperpolarized V_m, while cells arrested in the G_0/G_1 and M phases show a depolarized V_m.

Similarly, in neuroblastoma cell lines, cell cycle progression was observed to be correlated with hyperpolarized V_m in G_1/S transition and depolarized V_m at the M phase [70].

All these results clearly indicate that K^+ ion channels may be determinant in modulating the replication of both tumoral and healthy cells.

Chapter 2

Materials and methods

In this Chapter the details about the materials, the equipments and the experimental protocols employed for the preparation of PEDOT:PSS substrates and biological samples, the recording of the electrophysiological parameters and the investigations of cellular functionality are presented. In particular, after a brief description regarding the protocols adopted to maintain cells in standard culture conditions, the fabrication procedure of redox PEDOT:PSS substrates and the characterization methods used to study their physical properties are described. Furthermore, the patch clamp technique performed in this work is explained in detail, as well as the data recording methods and their analysis. Finally, the biological tests used to investigate the cellular response under different growing conditions are described.

2.1 Cell culture protocols

Glioblastoma multiforme cell line (T98G). The T98G cell line, derived from a brain tumor from a 61-year-old Caucasian male, was purchased from the European Collection of Authenticated Cell Cultures (ECACC). Cells were maintained in Roswell Park Memorial Institute (RPMI) medium, supplemented with 10% foetal bovine serum, 1% L-glutamine, 10% sodium pyruvate and antibiotics (1% penicillin and 1% streptomycin).

Human dermal fibroblast (hDF). hDF primary cells were obtained from skin biopsies according to standard culture protocols, and were gently provided by Prof. S. Salvioli (DIMES, University of Bologna) and G. Lattanzi and M. R. D'Apice (Tor Vergata Polyclinic, Roma). All the donors, an healthy young (age 23 years old), two juvenile carrying a G608G LMNA mutation (age 6 and 9 years old) and two healthy juvenile (age 9 years old), gave their informed consent before biopsy was performed. hDF of 3-15 passage number were maintained in Dulbecco's modified Eagle's medium (DMEM), supplemented with 10% foetal bovine serum, 1% L-glutamine, 10% sodium pyruvate and antibiotics (1% penicillin and 1% streptomycin). Before performing the experiments, hDF cultures were checked for the presence of signs of proliferative senescence (increased doubling time and morphological changes such as extensive enlargement of the plasma membrane) and only if these signs were absent the cells were used.

All cell cultures were periodically checked for mycoplasma infection or other contaminants. Unless otherwise stated, all chemicals and solutions were purchased from Sigma.

2.2 poly(3,4-ethylenedioxythiophene):poly(styrenesulfonate) (PEDOT:PSS) substrates

In this section the procedure to realize the PEDOT:PSS substrates and the experimental techniques adopted to study their physical properties are described. For further details see *Marzocchi et al., 2015* [16].

2.2.1 Fabrication of the PEDOT:PSS substrates

Electropolymerized PEDOT:PSS was synthesized onto glass slides previously coated with spin-coated PEDOT:PSS (commercially available CleviosTM CPP105D) thin films. The deposition solution was prepared by dissolving

Poly (sodium 4-styrenesulfonate) powder (average molecular weight $\sim$ 70000 g/mol) and the pure EDOT monomer in water. The deposition was stopped at 0 V in order to obtain a "Not biased" film that exhibits features that are intermediate between the oxidized and reduced substrates. These biased forms were obtained by using PEDOT:PSS films as working electrodes in phosphate buffer solution (PBS), containing (in mM): 150 NaCl; 3 Na_2HPO_4; 1.05 KH_2PO_4 and applying a positive voltage of +0.8 V (Oxidized) or a negative one of -0.9 V (Reduced) using a potentiostat.

2.2.2 Atomic force microscopy

PEDOT:PSS thickness was monitored as a function of time in a phosphate buffer saline solution (PBS) 0.1 M using a Park NX10 atomic force microscopy (AFM) with Park PPP-CONTSCR cantilevers (k = 0.2 N/m) in non-contact mode. A potential difference vs Ag/AgCl pseudo-reference electrode was continuously applied to the film using a Pt-wire counter-electrode connected to a Metrohm PGSTAT204. While the AFM recorded continuously a line scan, the potential was switched between an oxidizing (+0.8 V) and a reducing (-0.8 V) value every 100 s. AFM height maps of reduced, neutral and oxidized films were acquired in air.

2.2.3 Energy-Dispersive X-ray spectroscopy (EDX)

The relative abundance (in atomic %) of K^+, Na^+ and Cl^- atoms was measured through energy-dispersive X-ray spectroscopy (EDX) using a Cambridge Stereoscan 360 Scanning Electron Microscope (SEM) equipped with an Oxford Instruments X-ray detector. The PEDOT:PSS films investigated with EDX were deposited on a poly(methyl methacrylate) (PMMA) layer, so as to remove the interference coming from K^+, Na^+ and Cl^- atoms within the usual glass substrate. After PEDOT:PSS deposition, the films were immersed in a solution containing NaCl 0.1 M and KCl 0.1 M and a potential difference of +0.8 V (Oxidized) or -0.9 V (Reduced) vs SCE reference electrode was

applied for 1 h. As a control, some PEDOT:PSS films were immersed in the electrolyte solution for 1 h with no bias applied (Not biased). The data obtained were normalized to the relative abundance of K atoms in the not biased PEDOT:PSS film.

2.3 Patch clamp technique and data analysis

Resting membrane potential and voltage-dependent membrane current were measured both using a patch-clamp technique in whole-cell configuration at room temperature (RT, 22-24°C) with an EPC-10 amplifier (HEKA Elektronik, Darmstadt, Germany) interfaced with a compatible computer system equipped with Patchmaster software. Before recordings, cells were detached by trypsinization (trypsin-EDTA 0.02%), suspended in 1:3 culture medium and kept inside a biological safety cabinet in a Falcon tube. Within 6 hours, about 30 $\mu l/cm^2$ of suspended cells were seeded on the cellular growth support depending on the experiment to be performed. After 15 min was controlled the adhesion degree of the cells to the substrate, they were rinsed twice with the bath solution and about 2 ml of the same solution was left for recordings. The bath solution (extracellular electrolyte solution), the same for all cells, contained (in mM): 133 NaCl, 4 KCl, 2 $MgCl_2$, 2 $CaCl_2$, 10 4-(2-hydroxyethyl)-1-piperazineethanesulfonic acid (HEPES) and 10 glucose (pH 7.4, NaOH). The electrode solution (pH 7.2, KOH) contained, for recordings with T98G cells (in mM): 10 NaCl, 120 K-aspartate, 2 $MgCl_2$, 4 $CaCl_2$, 10 HEPES, 10 ethylene glycol tetraacetic acid (EGTA), 3 Mg-ATP, 0.2 GTP-Tris, while for hDF cells (in mM): 145 KCl, 1 $MgCl_2$, 1.8 $CaCl_2$ and 10 HEPES. After filling patch pipettes with the electrode solution, those whose resistance ranged between 3 and 7 MΩ were used for recording. When needed, blocking solutions to test the presence of specific ion channels on the plasma membrane were prepared. In particular, in this work I used a solution containing 10 mM of tetraethylammonium chloride (TEA), prepared starting from an adjusted bath solution (123 mM NaCl), to check the pre-

sence of potassium currents, and a second solution, obtained adding 100 nM of Iberiotoxin (IbTx), in order to characterize specific potassium currents, according to *table 1.2*. For further details see *Amorini, 2014* [71].

2.3.1 Voltage-clamp configuration

This is the basic patch clamp mode; the related circuitry is shown in the *figure 2.1*. The pipette potential is derived from the signal applied in input (Stim-In), with a variable offset added from the V-membrane control. The sum of these two sources is displayed and monitored as signal (Voltage Monitor). Before being applied to the pipette a further variable offset is added to V_0, which is due to the Liquid Junction Potential (LJP), that is a potential occuring when two electrolytic solutions of different concentrations are in contact one with the other.

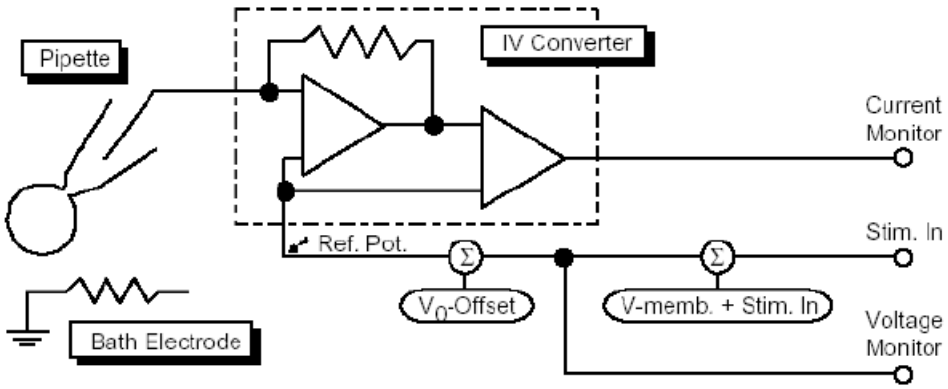

Figure 2.1: **Circuit diagram for the voltage clamp mode.** The high gain operational amplifier is connected in the circuit so that the transmembrane potential is compared with the clamp voltage stimulus (Stim. In). A current is generated to bring the membrane potential to the clamp voltage, and measured as a voltage drop across the feedback resistor.

Current traces were low-pass filtered at 2.9 kHz and digitized at 20 kHz by using EPC-10 board. Voltage stimuli (20 mV, 150 ms) from -30 to +110 mV were delivered at intervals of 1 s; to inactivate other voltage-activated K^+ currents, the holding potential V_h was set to 0 mV. Before each recording, a tracked leakage subtraction was performed (and then repeated automatically every 10 ms), together with on line compensations to minimize fast and slow capacitance transients. If the compensation process succeeds it is possible to start the stimulation protocol and then automatically measure cell capacitance and record current amplitude.

In the panel shown in *figure 2.2* are represented some drawings regarding the different steps of voltage clamp technique with examples of traces taken from the EPC-10 manual [72], which can be summarized as follows:

A When Ag/AgCl electrode is immersed inside the bath solution the resistance measured depends mainly on the concentration and mobility of ions contained in the pipette;

B Simulated response of a 10 MΩ pipette that is open to the bath solution. Resetting the amplifier (1) and applying a test pulse of 10 mV amplitude and 5 ms duration (2, 3) (red trace) the current response (black trace) can be displayed on the digital oscilloscope. If the gain range (4) is appropriate, you see a rectangular current of about 1 nA in response to the test pulse, according to Ohm's law;

C attaching the pipette on the cell membrane the electrical resistance increases considerably and it is possible to obtain a Giga-seal;

D in order to see the small currents resulting from the Giga-seal you need to set the gain to an appropriate value (1), in this way you can see two fast capacitive transients (black current trace) due to the electrical capacity of the pipette, which can be filtered by C-fast compensation, manually (2, 3) or automatically (4);

E after C-fast compensation the capacitive spikes are no longer present in the current trace, even increasing the gain;

F in whole-cell configuration the plasma membrane is disrupted by a depression performed through the pipette tip and consequently the resistance decreases;

G after reducing the gain to 20 mV/pA (1), the R-memb indicator should reflect the changed input resistance (2). If the voltage values at the current-to-voltage converter output exceed the amplifier's voltage range this is signalized by the red clipping indicator (3). As done for C-fast compensation you can filter the current trace activating the C-slow compensation, manually (4, 5, 6, 7) or automatically (8). If the compensation fails, you should repeat the compensation steps until it succeeds; clicking the Cap Track button (9) does this automatic compensation repetitively after a delay specified (10);

H after C-slow compensation the system is ready to perform the stimulation protocol desired and then the current amplitude recordings.

For statistical analysis, only the values of the current amplitude recorded after reaching the steady-state level were considered and averaged to produce a single value for each trace acquired (*figure 2.3*). To quantify the plasma membrane permeability at potassium ions was used an adjusted bath solution (123 mM NaCl) containing 10 mM of tetraethylammonium chloride (TEA) that was applied to the cells with a perfusion rate of approximately 1-1.5 ml/min. By using the cell membrane capacitance we estimated the cellular radius according to the method described by *Sakmann and Neher, 1995* [73]. All values were expressed as mean ± S.E.M. The Student's t-test was used to compute the probability values (p) in two-group comparison for each voltage step. For the statistical significance was considered a threshold of $p = 0.05$.

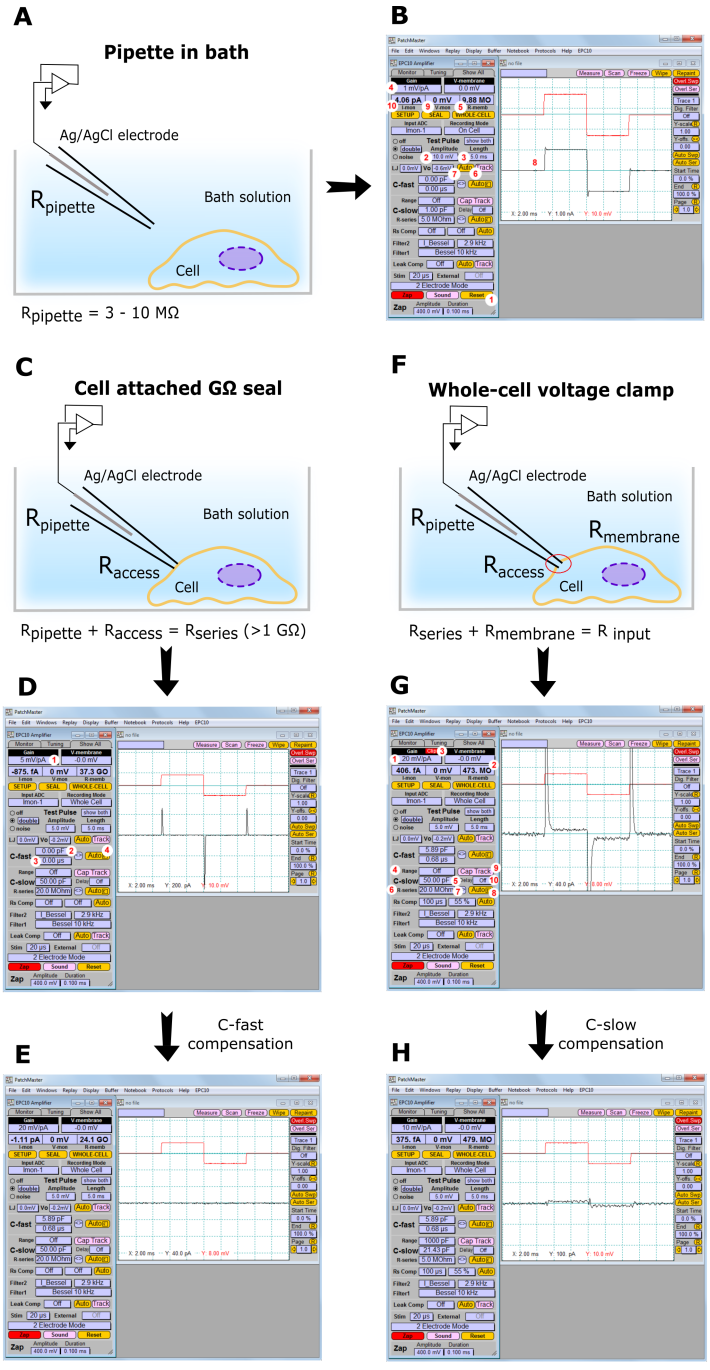

Figure 2.2: **Steps needed to perform whole-cell voltage clamp recordings.**

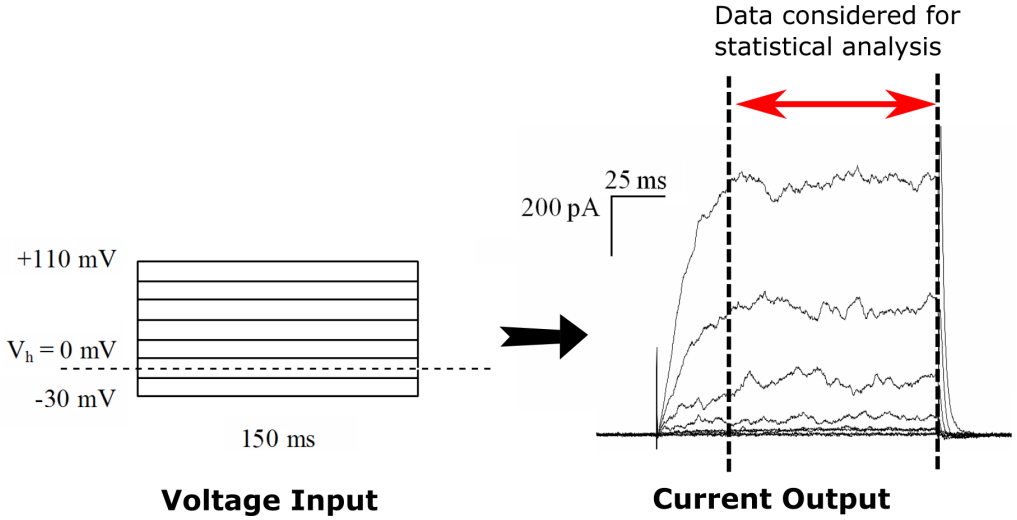

Figure 2.3: **Example of recording.** On the left is reported the stimulation protocol adopted in all the experiments performed (-30 to +110 mV at step of 20 mV and lasting 150 ms). On the right, an indication of the region considered for statistical analysis of the recorded current amplitudes values.

2.3.2 Current-clamp configuration

The current clamp mode can be used to measure the resting membrane potential or action potentials in electrically excitable cells; in this work, data were obtained adopting the "whole-cell" configuration. The relative electric circuit is shown in *figure 2.4*. The membrane potential is measured at Voltage Monitor level and represents the output of the recording. For stimulation, a commanded current can be injected while the pipette potential is measured. The commanded current (CC Stim. In) is determined by the sum of the voltages from the external stimulation input and the I-membrane control in the software.

Resting membrane potential was acquired through the balanced bridge technology of the EPC-10 amplifier, with the same digitizing rate used for voltage-clamp recordings. Before switching into the current clamp modality the compensation of the capacitance transients in the voltage clamp mode

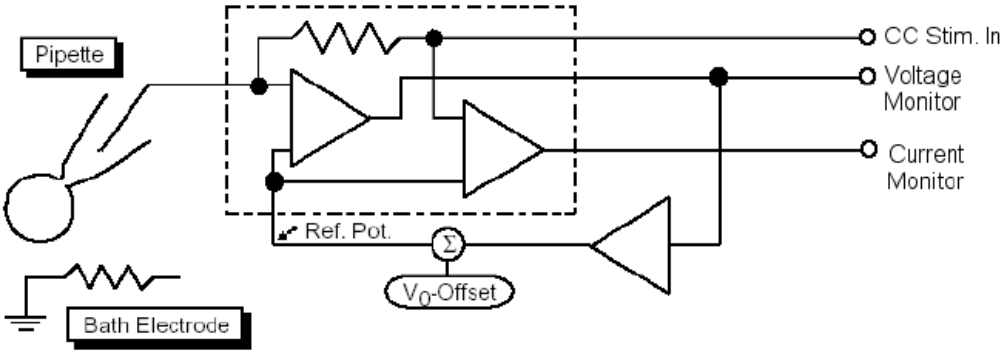

Figure 2.4: **Circuit diagram for the current clamp mode.**

was performed. The membrane current (I-membrane) was clamped at 0 pA in order to balance the ionic flows inward and outward the cell. To evaluate the resting membrane potential and at the same time the quality of the seal and the goodness of the recording, I used a stimulation protocol consisting of current steps (20 pA, 150 ms) from - 120 to + 120 pA delivered at intervals of 1 s. The resting membrane potential value of each cell was obtained by averaging the data from the baseline, i.e. the region of the voltage traces (from 0 to 100 ms) corresponding to the current holding of 0 pA. All values were expressed as mean ± SEM. Student's t-test was used to compute the probability values (p) in two-group comparison. A p threshold of 0.05 was considered for statistical significance.

2.4 A programmable electronic platform

2.4.1 Technical description of the prototyping board

The prototype presented is based on an Arduino2 board linked to a stripboard with electronic components. As shown in *figure 2.5* (left) the entire system is assembled inside a sealable plastic box in order to be easily transportable and avoid accidental breakage.

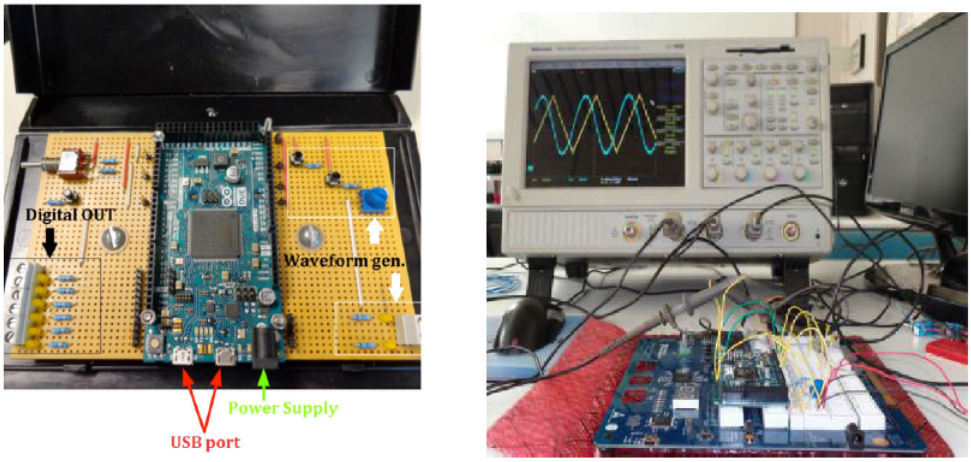

Figure 2.5: **Assembly and testing of the prototyping board.** (left) The programmable electronic platform soldered and mounted inside the plastic case; (right) example of the waveform generated by the prototype.

The Arduino2 board allows to make the electronic platform fully reprogrammable and versatile. The actual configuration of the device (including firmware) is capable to provide: six digital outputs of 3.3 V maximal voltage and one electric current output from 5 μA to 5 mA. Furthermore, on the platform there is a two-output waveform generator, able to produce four different independent waveforms (sinusoidal, square, triangle and sawtooth) whose frequency varies from 1Hz to 170 Hz (*figure 2.5* (right), *table 2.1*). In particular, the circuit in *figure 2.6* was tested as it was a wave-generator, by choosing the shape of the waveform and the frequency. These waveforms can be applied to generate an EF ("non-contact" mode) or, by closing the circuit in series with the culture medium, to generate a current flowing within the culture medium ("contact" mode). Moreover, we used an additional feature capable to generate constant voltages tuneable from 10 V to 50 V. In these conditions the EF can only be applied in the "non-contact" mode.

Outside the galvanotactic chamber, there were inserted, in series with the electrodes, two resistors (R and R_{var}) (*figure 2.6*): R can control the current range from 100 to 600 μA, while R_{var} can finely measure the current

within the living cell environment. Thus, we are able to precisely provide measurements of the current flowing through the cell culture medium with a resolution in the order of few μA.

Microcontroller AT91SAM3X8E	Operating Voltage 3.3 V
Digital I/O Pins 54 (12 PWM)	Analog Outputs Pins 2 (DAC)
Flash Memory 51 kB	SRAM 96 kB
Clock Speed 84 MHz	Length 101.52 mm
Width 53.3 mm	Weight 36 g
6 voltage digital outputs (0-3.3 V)	1 current output (5 μA-5mA)
2 indipendent output waveform generator: sinusoidal, square, triangle and sawthooth at freq. 1-170 Hz	

Table 2.1: **Technical specifications of the Arduino2 board.**

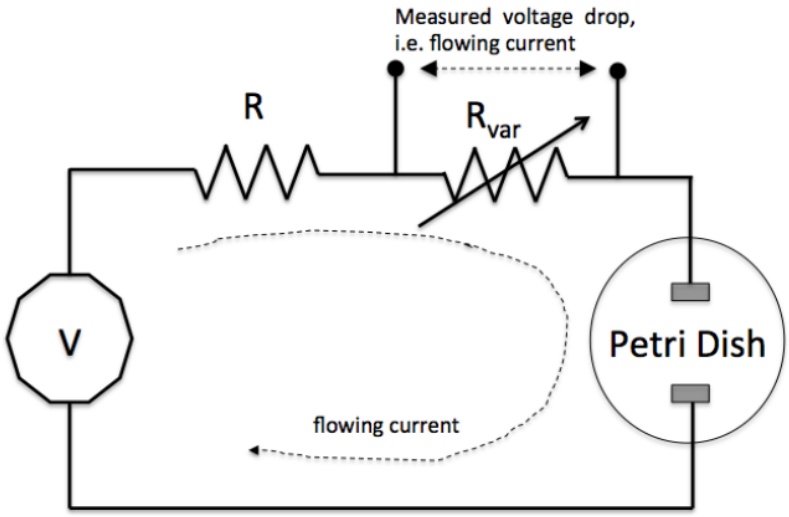

Figure 2.6: **Schematic representation of the circuit diagram used in the "contact" mode.** The current values were obtained using a variable resistor R_{var} by measuring the voltage drop.

2.4.2 Experimental setup

Glioblastoma multiforme cells (T98G), derived from a human tumor, were used to prepare the biological samples to test the device. Cells were plated on a standard 35 mm sterile plastic lidded dish for cell cultures (Petri dish) at a density of $0.010 \times 10^6 cm^{-2}$ and maintained in standard culture conditions (see cell culture protocols section) inside the microscope stage incubator. This apparatus is capable to provide the culturing standard conditions (37°C in humidified atmosphere at 5% CO_2) and, once placed on the motorized table of the inverted microscope Eclipse Ti (Nikon, Bologna, Italy), the image acquisition of living cells can be performed for several days. The Petri dish and the electronic components useful to deliver the stimuli were allocated into the microscope stage incubator by means of a home-made support platform (*figure 2.7*).

This platform has been designed to allow two pairs of copper plates placed along two perpendicular directions at different distances apart around the Petri dish ("non-contact" mode) or two Ag/AgCl electrodes plugged into the culture medium ("contact" mode). In the first case, we are able to switch the direction of the EF during the cellular motion and observe directly the cell response without any electric rearrangement, and to easily move the electrodes in order to obtain different strengths of the EF during the same experimental set. In the second case, we provide to the cells a constant current flow by the electrodes indirectly contacting the culture medium by means of agar salt bridges, made by plastic pipette tips filled with a pre-heated solution of 2-5% agar and 1M KCl (weight/volume) into which the wires are embedded. This technical escamotage ensures, indirectly, the electrical connection between the electrodes and the culture medium while minimizing the occurrence of chemical reactions at the surface of the electrodes. No distance or direction changes are allowed. In both cases, we can provide an electrostatic or variable EF upon time, depending on how we program the Arduino2 system.

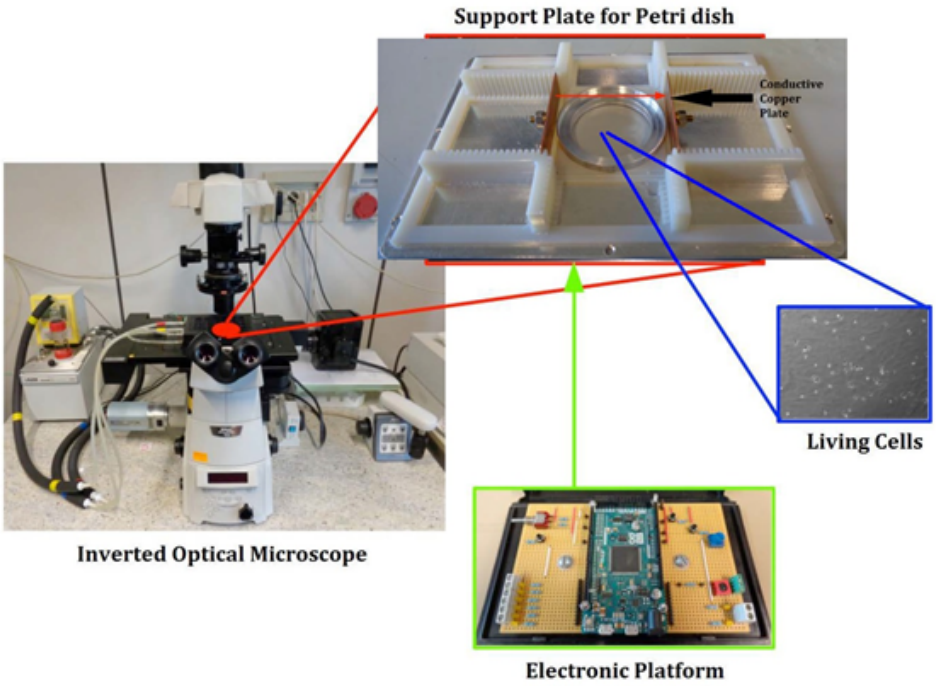

Figure 2.7: **Experimental equipment for galvanotaxis studies.** The inverted microscope Nikon Eclipse Ti, equipped by a small incubator for the living cells time-lapse imaging, is currently in use at the Department of Physics and Astronomy of the University of Bologna. The support plate for the 35 mm Petri dish appears in the "non-contact" mode: the conductive copper plates are external to the Petri dish and connected to the anode (left) and to the cathode (right) (not shown).

In both operating modes the same experimental protocol was adopted. Image acquisition in time-lapse of living cells lasted two hours, with an acquisition rate of 1 frame/minute; frames from 0 to 60 min are acquired without any field, in order to evaluate the performance of cells under control conditions (baseline). At 61 min the field was turned on and applied at a constant voltage for 60 min (until the end). By the use of Nikon Instruments Software (NIS) we acquired, in phase contrast configuration, 120 images (60 with and 60 without the stimulus) at 100× magnification. The analysis of the

frames sequence was performed with the tracking object tool of the tracking module of NIS Elements analysis software: each single cell of the visual field acquired (the centrum of the Petri dish) was selected if distant enough from the other interfering cells, and tracked during the time-lapse section. Then, a polar graph was generated by the measured parameters, line speed (μm/s) and heading (degrees), that projects the real movements of the object into the graph area as vectors.

2.5 Cell adhesion and proliferation tests

These tests were performed to study T98G and hDF cellular viability in the different conditions treated in this thesis, that is, cells grown: i) on redox forms of PEDOT:PSS substrates; ii) in the presence of potassium blocking solutions.

When T98G and hDF cells reached sub-confluence, they were detached by trypsinization (trypsin-EDTA 0.02%) and suspended (1:3) in their respective culture media (supplemented RPMI for T98G and supplemented D-MEM for hDF as described previously) at RT. In order to plate the same number of cells for each growth substrate, cell counting by the hemocytometer was performed. Cells were seeded at a density of $0.010 \times 10^6 cm^{-2}$ for T98G and $0.015 \times 10^6 cm^{-2}$ for hDF, with 500 μl of respective culture medium. To study cell adhesion and proliferation, T98G and hDF cells were kept in a CO_2 incubation system integrated within a motorized stage, able to perform time-lapse imaging up to several days.

For adhesion experiments, cells were allowed to adhere for 15 min before the acquisition of images, performed in phase-contrast at 100× of magnification for a time interval up to 4 h, every 30 min, with the inverse automated optical microscope Eclipse-Ti (Nikon, Bologna, Italy). The same setup was used also for proliferation, but in this case acquisition was performed every 24 h, up to cellular confluence (72 h for T98G and 96 h for hDF), in *figure 2.8* is shown an example of cell growth.

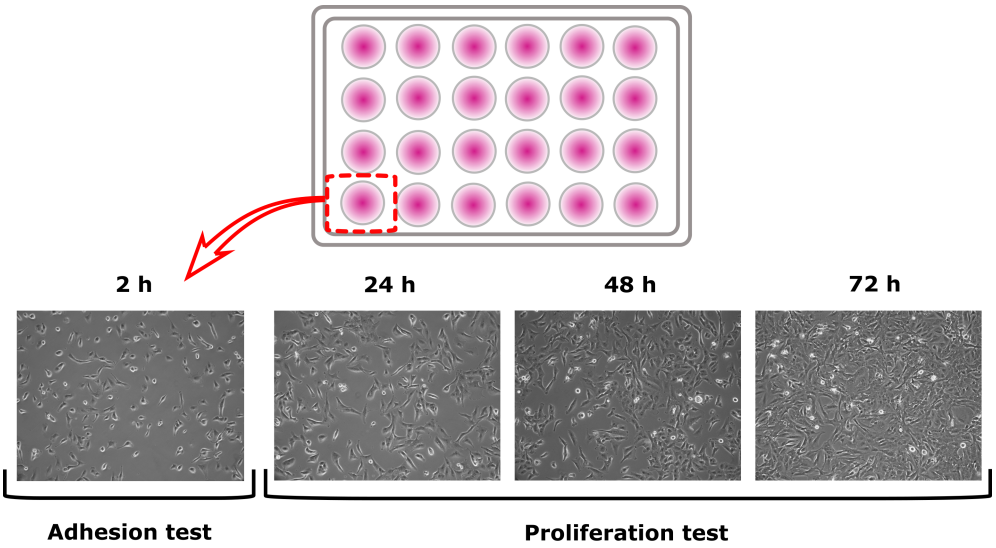

Figure 2.8: **Adhesion and proliferation tests.** (top) Schematic representation of a 24 multi-well plate used to growth experiments. Cells were plated in their respective culture medium. (bottom) Examples of images acquired after 2h (to assess cell adhesion capability) and after 24, 48 and 72 h from seeding for proliferation studies (T98G cells).

The number of adherent and not-adherent T98G and hDF cells was determined at 2 hours from plating, by classifying them according to morphological parameters such as shape (spherical or non-spherical), structural polarization, the presence of lamellar cytoplasm, leading lamella, and clear signs of stress fibers due to the focal adhesion process, as explained in *figure 2.9*.

The adhesion capability was defined as the number of adherent cells counted in a focal field of 0.68 mm^2 divided by the total number of cells. Proliferation analysis was performed by counting all cells present in an image field using ImageJ software and normalizing. The proliferation rates of both cell populations have been estimated by counting the number of adherent cells after 24, 48 and 72 h for the T98G and 96 h for the hDF (according to their malignancy grade, cancer cells reach the confluence earlier than healthy ones). The mean number of cells counted in three fixed focal fields sizing 0.68 mm^2 acquired from four wells at each time point was normalized with

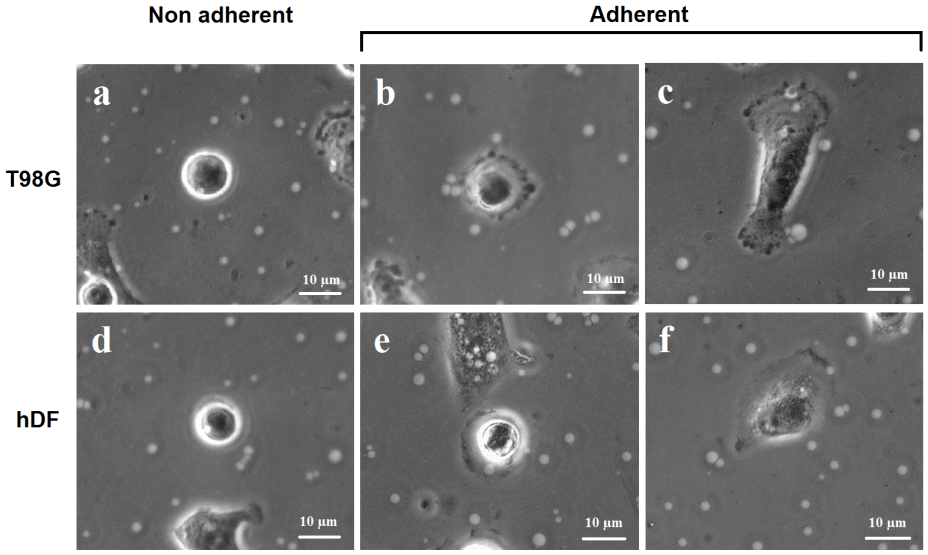

Figure 2.9: **Cell adhesion criteria.** Representative examples of T98G (**a, b, c**) and hDF (**d, e, f**) phase contrast microscopy images at 400× of magnification after 2 h from seeding on reduced PEDOT:PSS substrate. Cells in images **a** and **d** appear in rounded shape without any sign of cell spread; **b** and **e** show cells in an early phase of the focal adhesion process. **c** and **f** represent polarized moving cell with clear leading edge. Cells were considered adherent when widely spread or polarized respect to those poorly developed and still in a spherical shape. Scale bar 10 μm.

respect to the number of cells at 24 h from seeding. To study ageing in hDF, a sub-population of each cell type examined has been treated by 100 nM rIberiotoxin in order to inhibit BK_{Ca} channels. The results of the independent experiments were reported as mean ± SEM. Student's t-test was used to estimate the statistical significance; a value of $p = 0.05$ was considered as probability threshold.

2.6 Immunofluorescence assay

Immunofluorescence experiments were conceived to study ageing in human dermal fibroblasts. Part of the cell samples derived from the patch-clamp experiments were seeded at a density of 15.000 cells/well onto an imaging 24-well plates with the bottom made from cover glass and suitable for fluorescence microscopy at high resolution (Imaging Plate CG 1.5, Miltenyi Biotec GmbH, Germany) and incubated aerobically for 24 hours at 37°C. After washed three times with cold 0.15 M phosphate-buffered saline (PBS) pH 7.0 and subsequently fixed for 15 min with methanol 100% at -20°C, fixative were aspirated and cells were rinsed three times in cold PBS.

The presence of the large conductance Ca^{2+}-activated K^+ (BK_{Ca}) channels was assessed by using an indirect immunofluorescence assay performed with rabbit polyclonal IgG specific to the 199-213 amino acid residues of the BK_{Ca} channel protein on the 1st extracellular loop (Alomone Labs, Jerusalem, Israel).

A sample of cells, preventively treated with the blocking buffer solution, were loaded with the primary antibody 1:50 diluted in PBS, prepared from a stock solution (0.8 mg/ml in deionized water), and incubated overnight at 4°C. Cells were washed three times with PBS and then further incubated for 1 hour at RT with the secondary antibody, a donkey anti-rabbit IgG fluorescein 5-isothiocyanate (FITC)-conjugated antibody, 1:400 diluted in PBS. After rinsing three times in PBS samples were dry and added by the mounting medium with DAPI Duolink (Sigma-Aldrich, St. Louise, MO, USA) and observed with a Nikon Eclipse-Ti microscope equipped with epifluorescence filters. Images were acquired with a Q Imaging Retiga-2000RV camera by using the NIS-Elements AR software at 100× and 400× of magnification. Each experiment was performed in triplicate and repeated three times.

Semi-quantitative analyses was performed by the Nis-Elements 4.0 software (Nikon) processing the Regions of Interest (ROI) drawn around ten cells from each visual field acquired (n = 30). To calculate the integrated density the corrected total cell fluorescence (CTCF) formula has been used: area of

selected cell×mean fluorescence of background readings. Student's t test was used to compute the probability values (p) in the two-group comparison. A p threshold of 0.05 was considered for statistical significance.

Chapter 3

Electrically controlled PEDOT:PSS governs membrane potential

In this Chapter the results obtained studying the biological response to PEDOT:PSS substrates are shown. After a brief presentation regarding PEDOT:PSS structure and physicochemical properties, as well as its improved biocompatibility compared to other conducting polymers, all the findings resulting from the interactions between the cells tested in this work and the redox PEDOT:PSS substrates are described and discussed in detail.

3.1 Introduction

3.1.1 PEDOT:PSS structure and properties

Conjugated polymers (CPs) are a promising material class for bioelectronics and bioengineering applications such as bio-sensing and tissue repairing [74, 75]. Their beneficial properties of biocompatibility[76] and biofunctionalization,[77] along with their electrical, chemical and environ-

mental stability[78, 79] have earned them great attention towards novel applications in electronic medical devices.

One of the most interesting feature of CPs is their combined electronic and ionic conductivity and the possibility to modulate their oxidation state in a continuous manner [75]. Possible consequences of this unique material property are manifold. About two decades ago, it was demonstrated that changing the oxidation state of poly-pyrrole (PPy) allows for control of the morphology and growth of adherent mammalian cells [80]. Since then, most research in this area has been focused on the capability of CPs to electrochemically drive important physiological functions, such as adhesion[81, 82, 83, 84, 85, 86], proliferation [80, 82, 85, 86] differentiation[87] cell cross-talking, and secretion, biochemical and electrical signaling [88, 89]

Among CPs poly(3,4)-ethylenedioxythiophene (PEDOT) is particularly interesting due to its improved chemical-physical properties. It was developed at the Bayer AG research laboratories in Germany in the second half of the 1980s. It is an intrinsically conductive conjugated polymer composed by a chain of 3,4-ethylenedioxytiophene (EDOT) monomers, as shown in *figure 3.1*, which greatly improves conductivity and thermal and chemical stability compared to PPy, through decrease in band gap and reduction-oxidation potential [90].

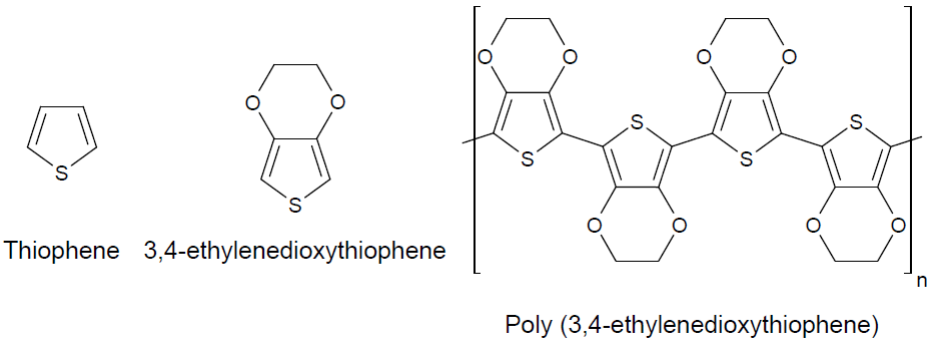

Figure 3.1: **Chemical structure of thiophene, 3,4- ethilenedioxythiophene (EDOT) and poly(3,4- ethilenedioxythiophene) (PEDOT).**

In detail, thermal studies showed that a continuous degradation occurs above 150°C and complete decomposition above 390°C [91]. Moreover electrical conducting properties appear to remain almost unaltered after aging in environmental conditions. This high stability is attributed to favourable ring geometry and the electron-donating effect of the oxygen atoms at the 3,4-positions stabilizing the positive charge in the polymer backbone.

PEDOT can be repeatedly doped and undoped. It is almost transparent and light blue in the oxidized state and can be easily changed into opaque and dark blue appearance in the neutral state. Thus its colour changes visibly when its doped state changes and may be suitable for optical applications, such as electrochromic displays [92]. More interestingly, the doping process affects also the conductivity of the polymer; in particular, PEDOT has a band gap of about 1.5-1.6 eV [93].

The lower band-gap relative to polythiophene is thought to originate from the influence of the electron-donor ethylene dioxy groups on the energies of the frontier levels of the π system. Experimental results show that, after doping, PEDOT exhibits reduced absorption in the visible: the oscillator strength shifts from around 1.5 eV (lowest $\pi \rightarrow \pi^{\star}$ transition) to below 1 eV in the metallic state. Thus, it shows a high electrical conductivity in its doped state [94].

Furthermore, compared to other conducting polymers, electrochemically synthesized films of PEDOT have a low redox potential and excellent stability in their doped state. from cyclic voltammetry experiments, it is found that the redox peaks at approximately 0 mV (oxidation) and -400 mV (reduction) remaining almost unaffected during cycling. However, only under an applied negative potential of -700 mV were the neutral films found to be stable. Open circuit potential measurements show that the neutral films are rapidly oxidized [95].

Specifically, doping of PEDOT occurs via a charge-balanced process in which the positive charge of mobile holes in the PEDOT polymer backbone is counterbalanced by negatively charged counter-ions introduced into the polymer itself during preparation. Interestingly, the amount of doping and

the chemical nature of the anion determine crucial physical and chemical properties of the conducting polymer/anion composite. One of the preferred anions used in the doping process is Polystyrenesulfonate (PSS) which produces highly conductive and stable CP composites due to its chemically inert polyanionic structure [96].

A schematic representation of the structure of PEDOT:PSS polymer composite, in its different scale levels, i.e. primary, secondary and tertiary, is presented in *figure 3.2*. For further details about the peculiar properties of the PEDOT:PSS films used as biocompatible substrates for the experiments described in this thesis see Marzocchi et al., 2015 and Marzocchi 2015 [16, 97].

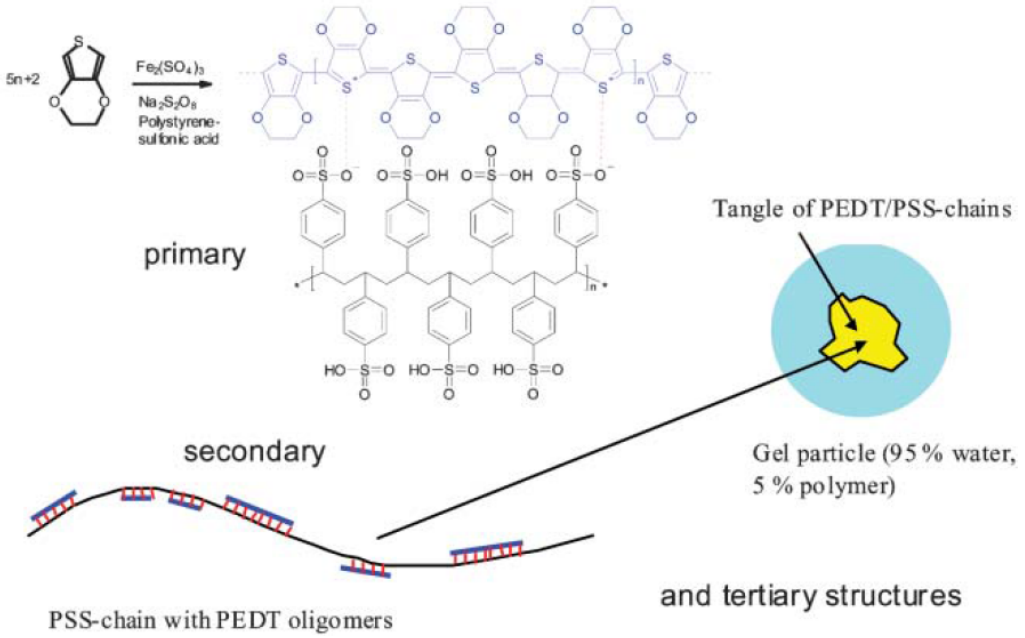

Figure 3.2: **Multilevel structure of poly(3,4-ethlenedioxytiophene) poly(styrenesulfonate) (PEDOT:PSS) films [97].**

3.1.2 PEDOT:PSS as a biocompatible substrate

PEDOT doped with PSS has shown an improvement in biocompatibility among a wide spectrum of cell types, along with the possibility of obtaining biofunctionalized substrates to improve the biotic/abiotic interface [98]. In particular, adhesion and proliferation of human fibroblasts [99] and epithelial tumor cell lines [100] are boosted, while the long-term survival of primary neurons [100, 101] and the differentiation process in myoblast are supported [102], suggesting PEDOT-PSS as an improved electro-ionic interface for a broad range of bio-medical applications.

It is known that the variation in oxidation state of CPs impacts their peculiar physical and chemical properties, such as topography, wettability [81, 86, 103], mechanical properties [98] and conductivity [16], which generally represent fundamental features that drive actively the cellular behaviour. Thus, the properties of the material should be considered carefully when studying its effects on cells in order to reduce the number of variables and understand which parameters are really important for cellular response.

In particular, oxidation or reduction of conducting polymers requires an uptake or release of ionic species from solution to compensate the variation in electronic charge on the polymer backbone. For example, in conducting polymers that contain large polyanions as dopants such PEDOT-PSS, reduction triggers an uptake of cations to balance the negative charge of the immobile polyanions. The increased amount of cations renders reduced PEDOT-PSS films more hydrophilic [16] and can induce swelling in solution [101]. Other effects include modification of protein adsorption [98] or field-induced conformational changes of the polymers; for example, at high applied voltage a reorientation of the hydrophobic groups toward the surface has been observed, decreasing the surface energy and conferring to the polymer film a higher hydrophobicity [81, 86, 103].

A complex interplay of physical and chemical properties of CPs controls cell viability and other cell behaviors. Nanotopography, for example, can elicit strong effects on cell adhesion, spreading, proliferation and genomic responses

in a broad range of cell types [103, 16, 104, 105, 106]. In some cases, it has been suggested that cells can recognize the morphological structures of the adhesion surface through a mechanotransduction mechanism that transduces external mechanical stimuli into biochemical signals, thus mediating the cell responses [107, 108, 109].

Regarding wettability, it was observed that cells adhere, spread, and grow better on surfaces with moderate hydrophilicity due to enhanced adsorption of serum proteins such as fibronectin and vitronectin [110], which are crucial for the focal adhesion process. Wettability, however, appears as a secondary property compared to the substrate topography [111].

Although these factors suggest that a possible route to control cells functionality with CPs might be based on the physical nano-structure of the surface, this approach showed a limited applicability for PEDOT:PSS based interfaces: CP films with surface roughness ranging from 6 to 33 nm, as obtained by variations in the deposition protocol, did not show a significant trend in cell adhesion and proliferation rate [16]. In addition, by testing PEDOT films with different conductive properties, it was also possible to exclude the possibility that conductivity could explain variation in cell behaviors. Further, we observed that a relevant enhancement of cell proliferation rate on reduced substrates occurs on different types of PEDOT:PSS used as substrate, and that the modifications in morphology or conducting properties induced by the reduction or oxidation process are separate from the effects on cell behavior parameters.

As a consequence of these findings, it was possible to conclude that the electrochemical state of the conducting polymer must be considered a crucial parameter for controlling cellular behavior at the CP/cell interface [16]. However, the detailed physicochemical interaction underlying the observed redox-control of cellular behavior remained elusive.

Therefore, one of the main topics of my experimental research activity concerned the study of PEDOT:PSS ion exchange capability relative to its redox forms, using cells as biological mediators. In particular I used the electrophysiological response of the plasma membrane of two different cell

types, glioblastoma multiforme cell line (T98G) and human dermal fibroblasts (hDF), as biosensors to indirectly measure ionic activities in the medium directly above the exchanging surface.

I then correlated these results with cell behavior parameters such as adhesion ability and proliferation rate. These findings clearly indicate that the redox state confers to PEDOT:PSS the property to modify the ionic environment around the cells, through a sort of "sponge-like" effect on ions. Thus, it was proved that cell adhesion and proliferation rates, two biological processes that are tightly correlated to both the ionic equilibrium and the electrophysiology of the cell, may be driven by this ionic modulation, suggesting interesting future developments and possible bioengineering applications.

3.2 Results

To understand the physiological adaptation of cultured cells to biased and not biased PEDOT:PSS substrates different biological responses were taken into account, i.e. adhesion capability, proliferation boost, voltage-dependent ion current and resting membrane potential. Thanks to its features, Glioblastoma Multiforme cell line (T98G) was chosen as a representative model for tumoral phenotype in this study. In particular, the stability of the cell line in culture, the high proliferation rates, the lack of contact inhibition and replicative senescence, as well as a well-known domain of potassium (K^+) channel expressed on the plasma membrane, made this cell line an ideal model for our purposes. On the contrary, the response of primary human dermal fibroblasts (hDF) was considered as a model of healthy cell, since they express a similar set of potassium ion channels on their plasma membrane. Therefore, the results obtained by the comparison between the T98G and hDF cell types, are even more interesting because they reflect two diametrically opposite physiological states of a living cell. Experiments were performed seeding the cells on a polystyrene substrate of standard cell culture plates, used as control (CTRL) and on all the three types of PEDOT:PSS substrates here investigated: Not

biased, Oxidized and Reduced, fabricated by electrodeposition through 8 cycles of cyclic voltammetry as described in Chapter 2, paragraph 2.2.1.

3.2.1 Adhesion and proliferation rates of the T98G cells are PEDOT:PSS redox state dependent

Results presented in *figure 3.3A* show that the adhesion properties of the T98G cells are enhanced when the PEDOT:PSS substrate has been biased: the adhesion rate of cells plated on the Oxidized (52.2 ± 1.3%, n = 12) or Reduced (63.5 ± 1.1%, n = 13) significantly increases compared to the Not biased (30.6 ± 2.1%, n = 14) with a $p \ll 0.001$ for both comparisons. It is relevant that substrates in the reduced form exert a stronger effect than the oxidized ones ($p \ll 0.001$), suggesting that they act in different ways on the adhesion process. Furthermore, a decreased adhesion capability on the Not biased, which is about 50% lower compared to the CTRL (58.3 ± 0.8%, n = 21) is observed and this highlights that the not biased substrate itself may affect the cell adhesion process.

Regarding the replicative boost, already the qualitative observation of the acquired images reveals that T98G proliferation function is affected by PEDOT:PSS (*figure 3.4*). In detail, referring to *figure 3.3B*, it appears clear that cellular growth is positively affected by the oxidized (2.7 ± 0.1, n = 5) and the reduced (3.9 ± 0.4, n = 5) forms of the PEDOT:PSS substrate compared to the not biased one (2.0 ± 0.2, n = 6), matching the adhesion results. Indeed, at 72 h after seeding the proliferation rate of cells growing on the biased PEDOT:PSS was significantly higher compared than that obtained for the Not biased samples ($p < 0.05$ and $p < 0.01$, respectively for Oxidized and Reduced vs Not biased). This effect seems to be more relevant on the Reduced, being already significantly different at the beginning of the growth curve (after 48 h from seeding) and stronger at the confluency when compared to the Oxidized ($p < 0.05$). Furthermore, in order to display the effect of the pristine form of PEDOT:PSS, data obtained from T98G growing on the CTRL and on the not biased substrates were compared; cell population

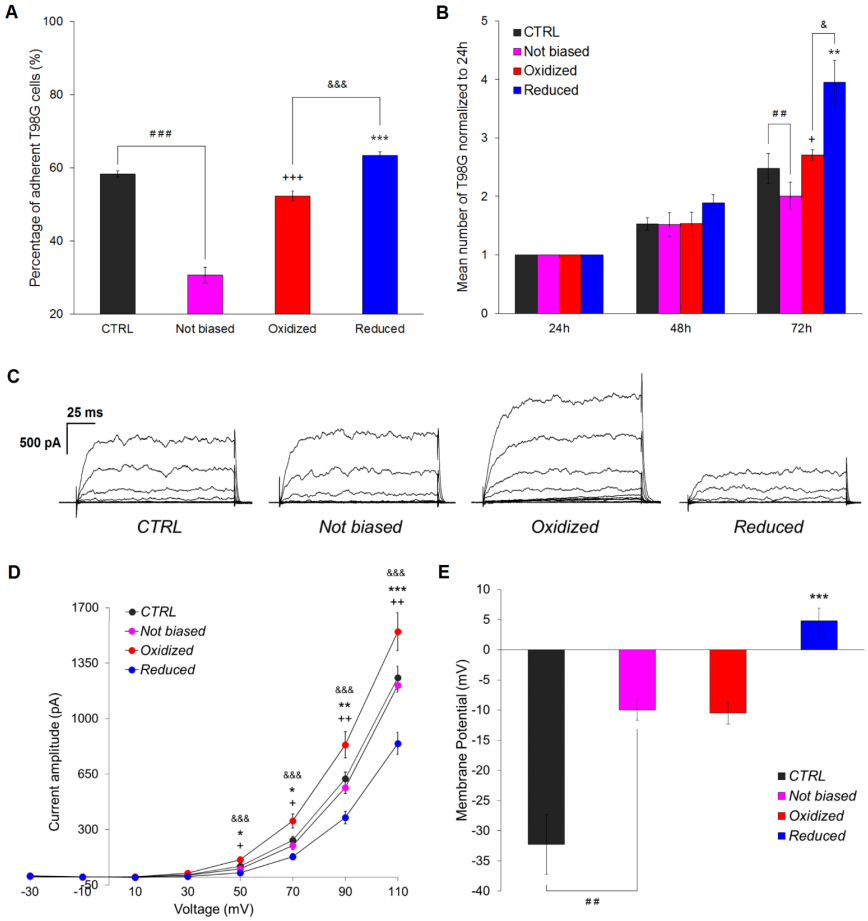

Figure 3.3: **Effects of PEDOT:PSS at different redox forms on T98G adhesion, proliferation and electrophysiology.** (**A**) Adhesion rate: percentage ± SEM of adherent T98G after 2 h from seeding on polystyrene Petri dish (CTRL, n = 21) and on Not biased (n = 14), Oxidized (n = 12) and Reduced (n = 13). (**B**) Proliferation rate: mean number ± SEM of T98G cells counted at 24, 48 and 72 h (confluence) and normalized to data obtained at 24 h from seeding. Cells were plated on CTRL (n = 5) and on Not biased (n = 6), Oxidized (n = 6) and Reduced (n = 6). (**C**) Comparison of representative examples of whole-cell current traces recorded in T98G seeded on CTRL and on PEDOT:PSS substrates. (**D**) Average ± SEM of current-voltage relationships (I-V) recorded in T98G plated on CTRL (n = 16), Not biased (n = 14), Oxidized (n = 14) and Reduced (n = 15). (**E**) Average ± SEM of the resting membrane potential recorded in T98G seeded on CTRL (n = 11), Not biased (n = 7), Oxidized (n = 13) and Reduced (n = 10). CTRL vs Not biased: ##p<0.01, ###p<0.001; Not biased vs Oxidized: +p<0.05, ++p<0.01, +++p<0.001; Not biased vs Reduced: *p<0.05, **p<0.01, ***p<0.001; Reduced vs Oxidized: &p<0.05, &&&p<0.001. All p values were calculated by Student's t-test.

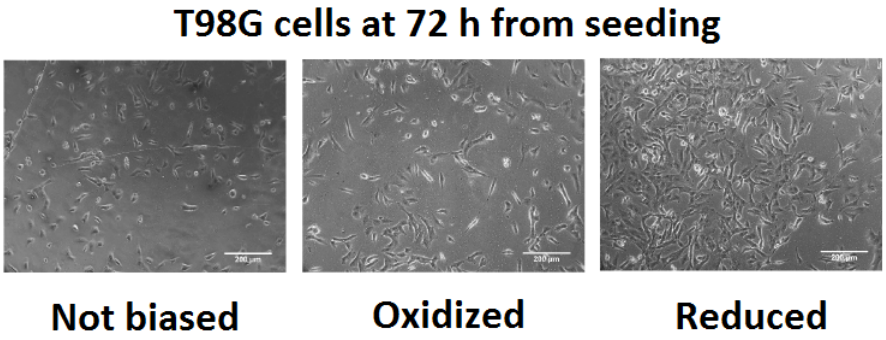

Figure 3.4: **Proliferation of T98G cells.** Representative example of T98G phase contrast microscopy images at 100× of magnification on oxidized (+0.8 V), not biased and reduced (-0.9 V) PEDOT:PSS after 72 h from cell seeding. Scale bar 200 μm.

showed a significantly higher proliferation rate on the CTRL only at 72 h after seeding. Despite these results, the proliferation rate increment at the confluence time point (72 h) on the Reduced sample is by three times as much the value at time zero (24 h), suggesting a strong efficiency of this specific redox state on cellular replication process.

3.2.2 PEDOT:PSS redox state affects the electrical properties of the T98G cells

The results described thus far show that cell adhesion and proliferation processes are strongly correlated with the redox state of PEDOT:PSS. Beside other pathways, it is known from the literature that these processes are actively driven by K^+ channels activity [112, 62, 70]. Thus, since redox processes in PEDOT:PSS substrates are accompanied by ion-migration across the film-liquid interface [75], the attention was focused on the electrical properties mediated by intra- and extracellular ionic concentrations. In detail, transmembrane whole-cell currents, recorded in voltage-clamp mode, and resting membrane potential, recorded in current-clamp mode, were considered for this investigation, starting from T98G cells plated on CTRL and on Not

biased, Oxidized and Reduced.

In order to single out the K^+ current from the overall current recorded in both cell types I performed a set of experiments using the non-selective K^+ channel's inhibitor tetraethylammonium chloride (TEA) at the saturating concentration of 10 mM. As reported in *figure 3.5A* T98G cells displayed an outward current whose amplitude, at 110 mV of voltage potential, is about 1257 ± 74 pA (n = 16) that is almost completely blocked by perfusion with TEA (128 ± 20 pA). The same is true also for hDF (as it will be shown in more detail in the next paragraph). Indeed, although their current amplitude at 110 mV of stimulation step reaches only half of that of T98G cells, that is 592 ± 63 pA (n = 12), when TEA is applied the current drops to very comparable values (83 ± 34 pA) *figure 3.5B*. Thus, no other relevant currents were revealed by this analysis, indicating that the current recorded is predominantly due to ion fluxes through outward K^+ channels; this is a further confirmation of the fact that these two cell types have similar electrical properties, as mentioned earlier.

Representative examples of the current traces recorded on CTRL and on Not biased, Oxidized and Reduced are reported in *figure 3.3C*, which compares mean current amplitudes relative to each voltage step (I-V curve) recorded from T98G cells plated on CTRL with those plated on each different form of PEDOT:PSS substrates. The statistical analysis shows that the amplitude of K^+ current recorded is not affected by the Not biased. Interestingly, both the Oxidized (1549 ± 120 pA at 110 mV, n = 14) and the Reduced (843 ± 70 pA at 110 mV, n = 15) appear to act as consistent effectors, significantly changing the amplitude of the current compared to the Not biased (respectively $p < 0.01$ and $p < 0.001$ at 110 mV of voltage stimulation) (*figure 3.3D*).

Taking into account these results, it becomes central to determine whether and how resting membrane potential (V_{rest}) is affected in the presence of the biased forms of PEDOT:PSS. Therefore, the resting potentials of T98G cellular membranes were recorded from cells plated on CTRL, Not biased, Oxidized and Reduced in current-clamp mode (whole-cell current clamped at 0 pA). Averaged values of V_{rest} and statistical significances are displayed in

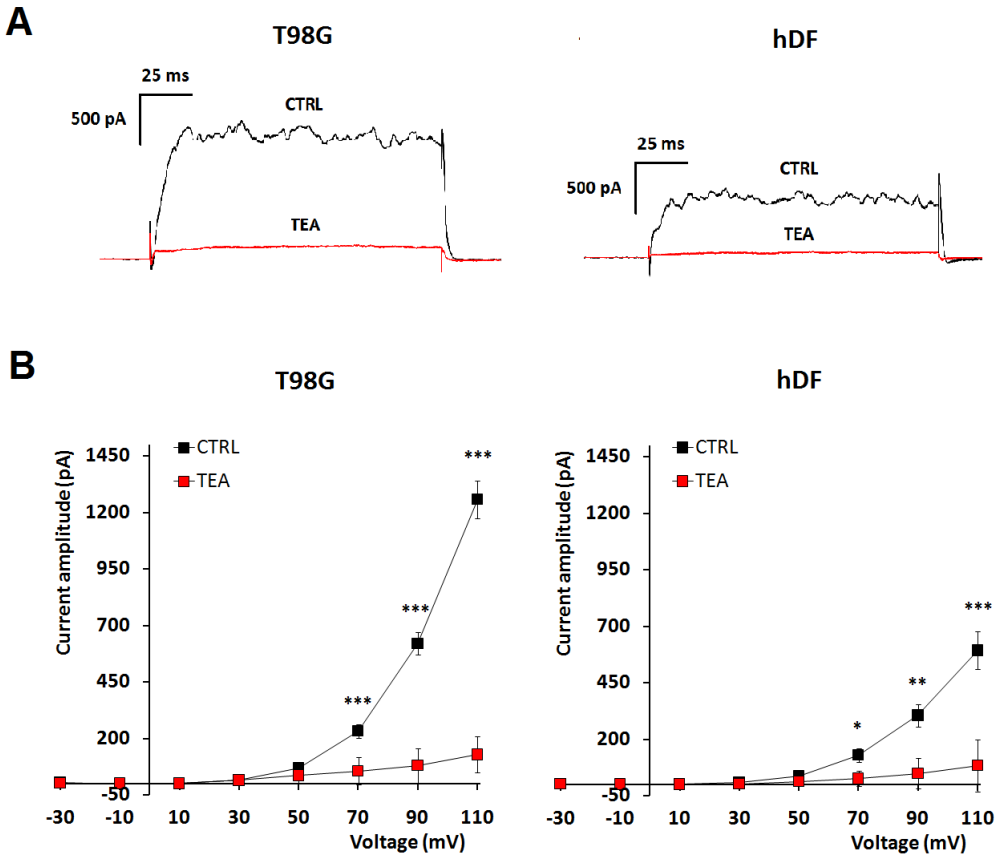

Figure 3.5: **Currents recorded in whole-cell configuration and TEA effect on T98G and hDF.** (**A**) Representative examples of current traces recorded at +110 mV before (CTRL) and after (TEA) 10 mM TEA application on polystyrene Petri dish. (**B**) Average ± SEM of current-voltage relationships (I-V) obtained in T98G (CTRL n = 16; TEA n = 9) and hDF (CTRL n = 12; TEA n = 4) before and after TEA application as explained in (A). CTRL vs TEA: *p<0.05, **p<0.005, ***p<0.001. All p values were calculated by Student's t-test.

figure 3.3E. The results show that V_{rest} is affected by the not biased substrate by inducing a depolarization which increases in the biased samples from the Oxidized to the Reduced. In more detail, significant differences ($p < 0.01$) in the V_{rest} values obtained from T98G plated on the CTRL substrates are emerged when compared to the Not biased. Furthermore, assessing V_{rest} for Oxidized and Reduced, it was found a significant difference compared to the Not biased only for Reduced ($p < 0.001$). Thus, the most interesting and significant finding is that Reduced induces the largest depolarization of V_{rest}.

3.2.3 Testing a different type of cell

In order to validate our results in healthy cells, the same experiments were performed using human dermal fibroblasts, which are characterized, as showed above, by a very similar set of ionic channels expressed on the plasma membrane, but in the same time are more comparable to normal physiological conditions. Thus, testing hDF it was found out that adhesion rates are not significantly different between populations of cells plated on the not biased ($58.1 \pm 1.2\%$, $n = 13$), oxidized ($59.8 \pm 1.8\%$, $n = 10$) and reduced ($57.3 \pm 2.2\%$, $n = 11$) substrates (*figure 3.6A*). Interestingly, the comparison between the adhesion capability of T98G and hDF plated on Petri dish (CTRL) reveals that normal cells adhere better on polystyrene culture plates compared to tumoral ones, likely indicating that the physical properties of this material supports better the hDF adhesion process ($83.0 \pm 0.7\%$, $n = 12$) than the T98G one ($58.3 \pm 0.8\%$, $n = 21$). Furthermore, both cell populations show a decreased adhesion rate on PEDOT:PSS not biased that is about 25% lower compared to the CTRL one ($30.6 \pm 2.1\%$ vs $58.3 \pm 0.8\%$ and $58.1 \pm 1.2\%$ vs $83.0 \pm 0.7\%$ for the T98G and hDF respectively). This finding indicates that the Not biased itself may affect the cell adhesion process. Assessing the growth rate of normal hDF cells (*figure 3.6B*), it seems to be affected by the not biased as well as the biased forms of PEDOT:PSS substrates at an earlier stage than the one of T98G cells. Indeed, at 48 h from seeding the proliferation rate on the reduced (1.6 ± 0.1, $n = 6$) substrate is already

significantly higher than the not biased one (1.2 ± 0.1, $n = 6$). At 72 h and 96 h (the confluence time for hDF) both the Oxidized and Reduced are able to increase the proliferation rate, with a stronger effect of the reduced one. This type of cells shows, at each time point, a lower (but not statistically significant) proliferation rate on the Not biased compared to CTRL, while on Reduced a two-fold increase in the proliferation rate at 96 h is observed. Transmembrane whole-cell currents and resting membrane potentials were recorded from hDF plated on CTRL and Not biased, Oxidized and Reduced, in the same experimental conditions as for T98G. The representative examples of the current traces of cells plated on the four different substrates (*figure 3.6C*) and the mean currents relative to each voltage step (I-V curve) (*figure 3.6D*) show that the amplitude of K^+ current is not affected by the not biased PEDOT:PSS. Therefore, interestingly, in hDF the modulation due to the different oxidation forms of PEDOT:PSS substrates is not observed. Averaged values of V_{rest} and statistical significances are displayed in *figure 3.6E*. The main findings are that: a) V_{rest} is different between the tumor and the normal cells independently from the substrate, and b) the V_{rest} of both cell types is affected by the not biased substrate, inducing a depolarization. Indeed, the statistical analysis highlights significant differences ($p < 0.05$) in the V_{rest} values when hDF are plated on CTRL compared to the Not biased. Therefore, unlike the tumoral cells, hDF cells plated on Reduced show the same trend but the depolarization is much less pronounced compared to T98G and not significantly different relatively to the Not biased. Then, unlike the T98G cells, in the case of hDF no significant differences (or very mild) in adhesion and proliferation rates were observed between the biased forms of PEDOT:PSS and the not biased ones. These results strongly correlate with the data obtained by the electrophysiological analyses, indeed both V_{rest} and voltage-dependent ionic currents are not affect by the Oxidized and the Reduced (*figure 3.6*).

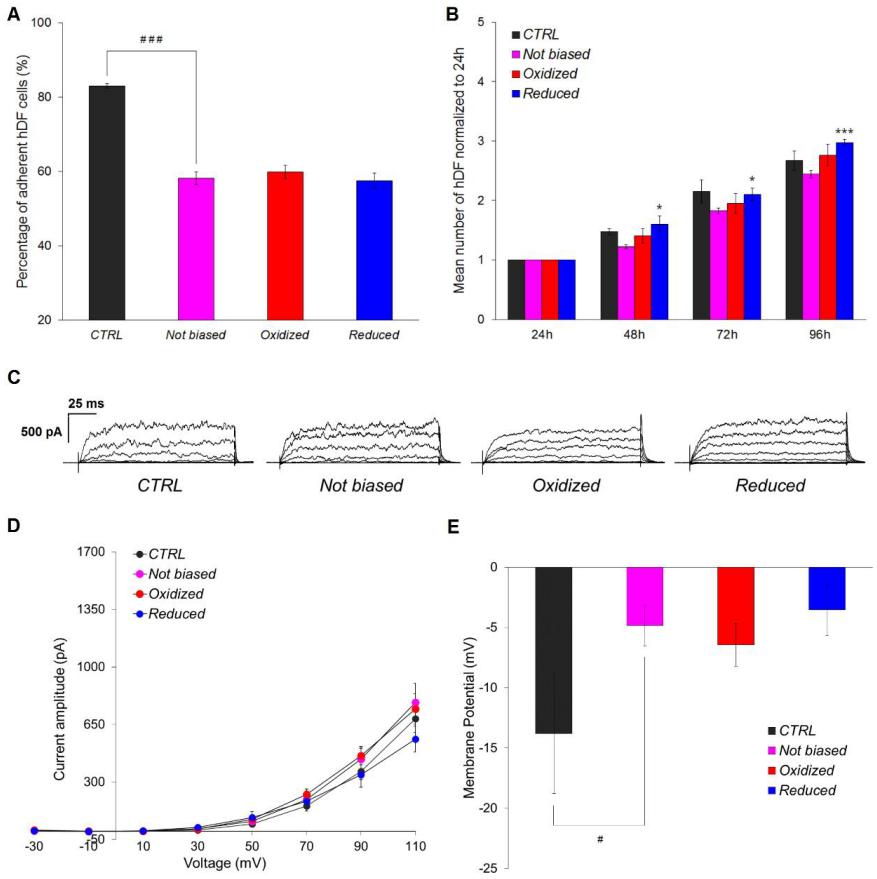

Figure 3.6: **Effects of PEDOT:PSS at different redox forms on hDF adhesion, proliferation and electrophysiology.** (**A**) Adhesion rate: percentage ± SEM of hDF after 2 h from seeding on polystyrene Petri dish (CTRL, n = 12) and on Not biased (n = 13), Oxidized (n = 10) and Reduced (n = 11). Adherent cells were counted in the same way as for T98G. (**B**) Proliferation rate: mean number ± SEM of hDF cells counted at 24, 48, 72 and 96 h (confluence) and normalized to data obtained at 24 h from seeding on CTRL (n = 6), Not biased (n = 6), Oxidized (n = 5) and Reduced (n = 6). (**C**) Comparison of representative examples of whole-cell current traces recorded in hDF seeded on CTRL, Not biased, Oxidized and Reduced. (**D**) Average ± SEM of current-voltage relationships (I-V) recorded in hDF on CTRL (n = 8), Not biased (n = 10), Oxidized (n = 6) and Reduced (n = 6). (**E**) Average ± SEM of the resting membrane potential whole-cell recorded in hDF after seeding on CTRL (n = 12), Not biased (n = 9), Oxidized (n = 7) and Reduced (n = 9). CTRL vs Not biased: #p<0.05, ###p<0.001; Not biased vs Reduced: *p<0.05, ***p<0.001. All p values were calculated by Student's t-test.

Specifically, in *figure 3.7*, it was reported a comparison between the V_{rest} of T98G and hDF. It reveals that the resting condition of the two cell types on CTRL are significantly different ($p < 0.005$), showing for T98G cells a more hyperpolarized plasma membrane.

This difference in the starting point of the V_{rest} could be the key to understanding why all the redox forms of PEDOT:PSS are not able to change the V_{rest} itself and to modulate the behaviour of hDF in the same way to what was observed for T98G.

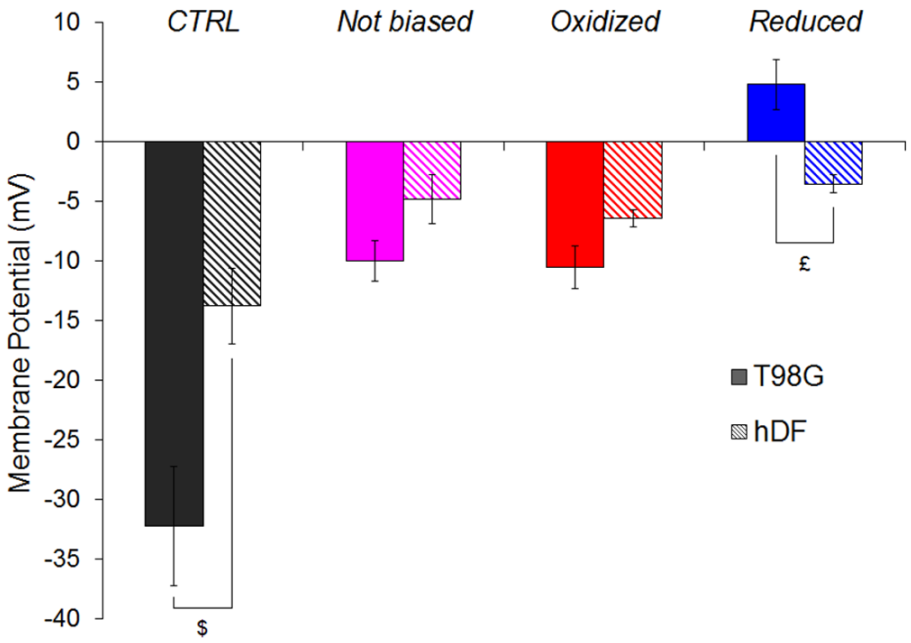

Figure 3.7: **Comparison between resting membrane potential recorded in T98G and hDF cells.** Average ± SEM of the resting membrane potential whole-cell recorded in T98G (solid colours) and hDF (diagonally striped colours) after seeding on CTRL (T98G n = 11, hDF n = 12) and on PEDOT:PSS Not biased (T98G n = 7, hDF n = 9), Oxidized (T98G n = 13, hDF n = 7) and Reduced (T98G n = 10, hDF n = 9). CTRL (T98G) vs CTRL (hDF): \$p<0.005; Reduced (T98G) vs Reduced (hDF) £p<0.005. All p values were calculated by Student's t-test.

Finally, data from all patch clamp recordings are summarized in *table 3.1*, for both types of cells.

In addition to current amplitude recorded at + 110 mV of voltage stimulation, it gives values (± SEM) of the membrane capacitances and relative cellular radius, estimated by the spherical capacitor-capacitance relationship [73], which look very similar to each other, ruling out the possible dependence of the results obtained from the cell size and morphology.

	CTRL	**Not biased**	**Oxidized**	**Reduced**
T98G	n = 16	n = 14	n = 14	n = 15
Current amplitude (pA)	1257 ± 74	1210 ± 44	1549 ± 120	843 ± 70
Capacitance (pF)	37.4 ± 5.2	46.7 ± 4.2	38.6 ± 2.0	41.4 ± 4.2
Radius (μm)	16.7 ± 1.1	19.0 ± 0.8	17.5 ± 0.4	14.8 ± 1.9
	n = 11	n = 7	n = 12	n = 10
Resting membrane potential (mV)	-32.3 ± 5.0	-10.0 ± 1.7	-10.5 ± 1.8	4.8 ± 2.1
hDF	n = 8	n = 10	n = 6	n = 6
Current amplitude (pA)	685 ± 83	784 ± 115	745 ± 93	561 ± 79
Capacitance (pF)	29.3 ± 6.1	23.1 ± 3.0	27.2 ± 2.9	30.3 ± 5.0
Radius (μm)	14.9 ± 1.5	13.2 ± 1.0	14.6 ± 0.8	15.3 ± 1.3
	n = 12	n = 9	n = 7	n = 9
Resting membrane potential (mV)	-13.8 ± 3.2	-4.8 ± 2.0	-6.4 ± 0.7	-3.5 ± 0.7

Table 3.1: **Summary of patch clamp experiments.** Mean values (± SEM) of whole-cell current amplitude (at 110 mV of voltage stimulation step), capacitance, radius and resting membrane potential obtained from recordings of T98G and hDF cells seeded on the PEDOT:PSS substrates tested in this work.

3.2.4 Swelling properties of PEDOT:PSS

Firstly, the swelling of the PEDOT:PSS film as a function of its oxidation state was characterized. To this end, AFM measurements in buffer solution (PBS) under electrochemical control, using reference and counter electrode, were performed. The variation of PEDOT:PSS film thickness, Δz, as measured while the polymer film is cycled between a reduced (negative potential of -0.8 V) and oxidized (positive potential of +0.8 V) state is displayed in *figure 3.8* (top panel). Variation of the potential leads to a characteristic fluctuation in the height of the film with a peak-to-peak amplitude of about 50 nm (10% of film thickness). The time scale of this swelling process was found to be in the order of tens of seconds. In the reduced state (negative potential) the extension of the film was maximized, while oxidation led to shrinking. However, during biological experiments, changes in the PEDOT:PSS redox state occurred on a longer time scale, following an exponential decay towards an intermediate state, which is showed in *figure 3.9*.

In order to investigate the possible impact of redox-processes on the surface topography of PEDOT:PSS films, it was acquired an AFM height maps for the reduced, neutral and oxidized films (*figure 3.8*, bottom). All three films exhibit the characteristic cauliflower morphology of electropolymerized PEDOT:PSS with nanometric globular extensions at the surface. In the reduced state, the globular extensions at the surface are slightly enlarged which is attributed to the swelling. Accordingly, also the roughness in the reduced state was slightly enlarged. Statistical analysis on 5 μm maps revealed rms-roughness values of 15.5 $\pm$ 2.2 nm, 9.8 $\pm$ 2.2 nm and 11.0 $\pm$ 2.8 nm, for reduced, neutral and oxidized films, respectively. However, these differences in surface topography are small and cannot be expected to account for the observed changes in cell behavior; larger variations on PEDOT:PSS surface topography (for example control of roughness ranging from 6 nm to 33 nm) can be obtained by varying electropolymerization conditions, which were reported not to exhibit significant impact on cells [16].

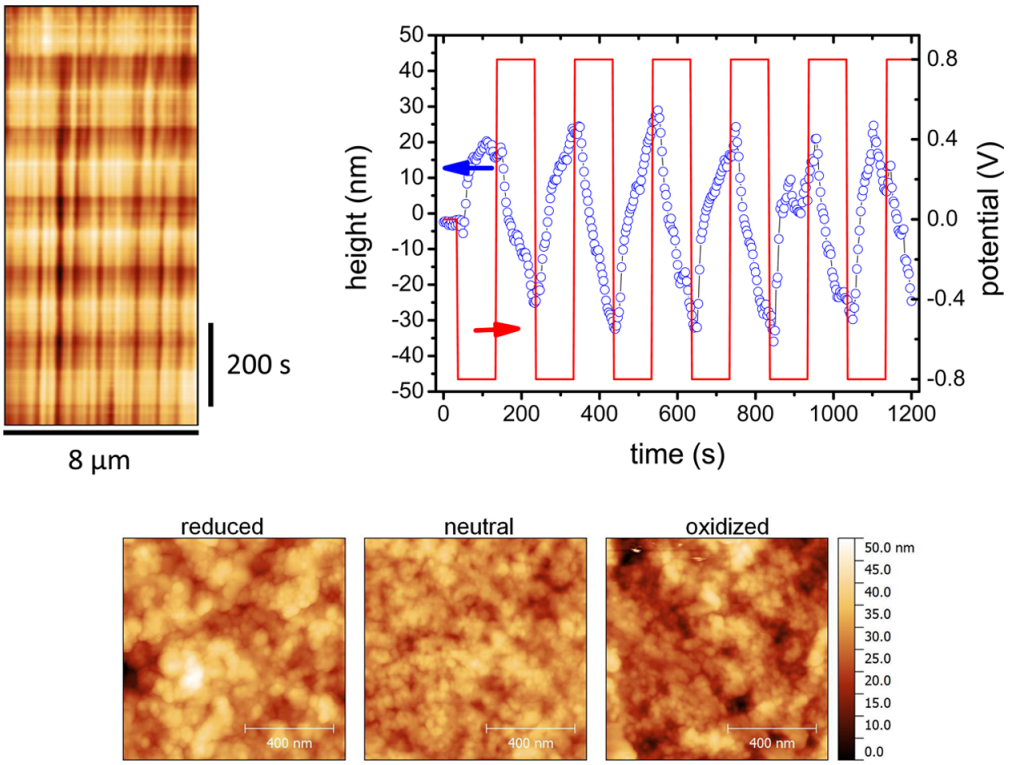

Figure 3.8: **Investigation of impact of potential on PEDOT:PSS film morphology and film thickness by AFM (non-contact mode). Top left**: height line scan (x-direction) continuously measured for 1200 s (y-direction) while the potential applied to PEDOT:PSS film immersed in PBS was varied between +0.8 V and -0.8 V. **Top right**: height of a single point in the linescan (blue, left scale) and applied potential (red, right scale) as a function of time. Negative potential yielded an increase in height due to redox mediated swelling. **Bottom**: height maps of reduced, not biased and oxidized PEDOT:PSS film.

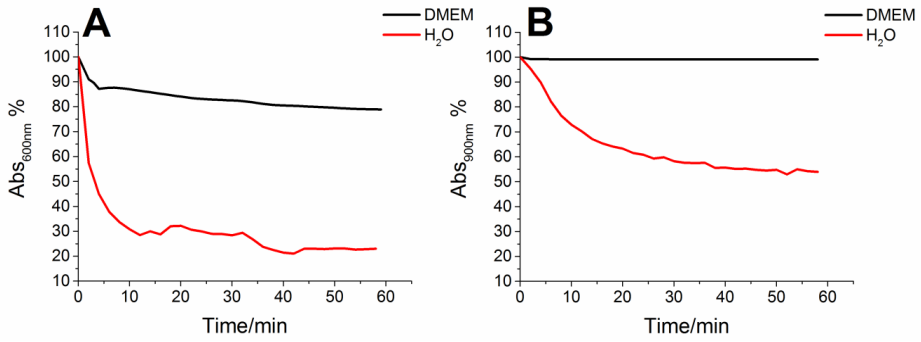

Figure 3.9: **PEDOT:PSS de-biasing curves recorded in DMEM and water by the acquisition of absorption spectra every one minute after the polarization.** The de-biasing curves of reduced (**A**) and oxidized (**B**) PEDOT:PSS were obtained by following the absorption of the peaks at 600 nm and at 900 nm, respectively. The peak at 600 nm is assigned to the transition $\pi \rightarrow \pi^{\star}$ of the polymer in neutral state and it was used to estimate the amount of PEDOT:PSS in a reduced form. The peak at 900 nm is ascribable to polarons, and it was exploited to evaluate the recovery of not biased PEDOT:PSS after the oxidation to bipolarons which show no absorption in the examined wavelength range.

3.2.5 Testing ion concentrations and migration dynamics in PEDOT:PSS

Using energy dispersive X-ray spectrometry (EDX) it was possible to quantify the amount of ion uptake during oxidation or reduction of PEDOT:PSS substrates in an electrolyte solution.

In *figure 3.10* are reported the atomic percentages of Na^+, K^+ and Cl^- ions, as well as the sum of K^+ and Na^+ (cations) for the three investigated cases. Both biased samples, Oxidized (2.4 ± 0.3, $n = 3$) and Reduced (10 ± 1, $n = 3$), showed a significantly increased amount of cations compared to the Not biased (1.6 ± 0.3, $n = 3$) with a $p < 0.05$ for both comparisons. It was also observed that cation adsorption was enhanced in the reduced form with respect to the oxidized one ($p \ll 0.001$).

The K^+ level was not statistically different between Oxidized (0.7 ± 0.2,

n = 3) and Not biased (1.0 ± 0.2, n = 3), while Not biased and Reduced were significantly different with a $p < 0.005$. Conversely, the Na+ level for Not biased (0.6 ± 0.2, n = 3), Oxidized (1.7 ± 0.3, n = 3) and Reduced (6.0 ± 0.7, n = 3) were significantly different with $p < 0.01$ for all the comparisons.

Moreover these findings demonstrate that during the oxidation process, a little amount of Cl^- anions penetrated into PEDOT:PSS, as suggested by a normalized Cl^- content of 0.4 ± 0.1. On the other hand, Reduced and Not biased exhibited a Cl^- signal that was lower than the limit of detection of the EDX analyzer. All results are summarized in *table 3.2*.

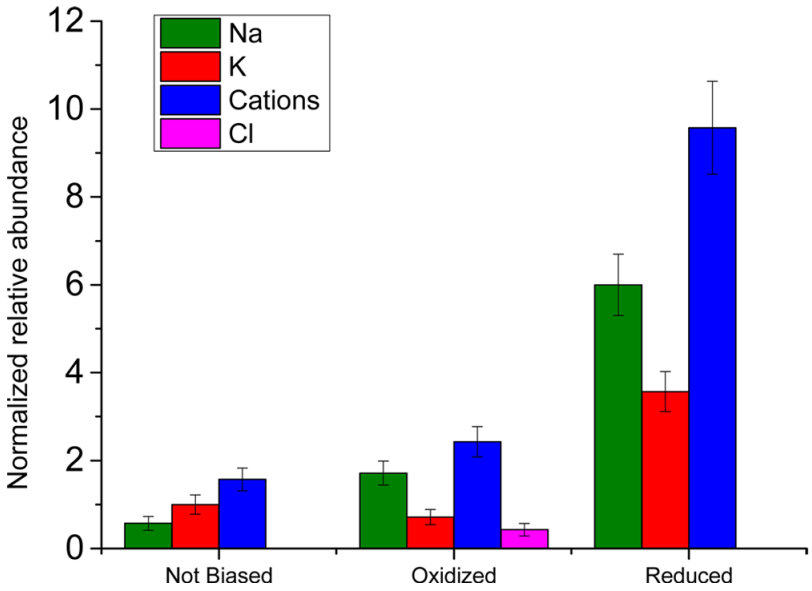

Figure 3.10: **Relative abundance of Na, K and Cl ions in not biased, oxidized and reduced PEDOT:PSS films.** The data were normalized to the K abundance recorded for not biased PEDOT:PSS film. The overall presence of positive ions absorbed by PEDOT:PSS, given by the sum of Na and K concentrations, is represented by the label "Cations".

	Na	K	Cations	Cl
Not biased	0.6 ± 0.2	1.0 ± 0.2	1.6 ± 0.3	0.0
Oxidized	1.7 ± 0.3	0.7 ± 0.2	2.4 ± 0.3	0.4 ± 0.1
Reduced	6.0 ± 0.7	3.6 ± 0.5	10 ± 1	0.0

Table 3.2: **Relative abundance (average ± standard deviation) of Na, K and Cl in not biased, oxidized and reduced PEDOT:PSS films.** The overall presence of positive ions absorbed by PEDOT:PSS, given by the sum of Na and K concentrations, is represented by the label "Cations".

3.2.6 Partial overoxidation of oxidized substrates

In order to prove that the PEDOT:PSS overoxidation occurs also at +0.8 V the substrates were characterized by cyclic voltammetry. The first cyclic voltammogram (*figure 3.11A*) recorded in PBS between -0.2 V and 1.5 V shows an irreversible redox wave with a peak potential of 1.4 V. Such a process, which is ascribable to the PEDOT overoxidation, starts at about +0.6 V, this value being lower than the potential used to prepare oxidized substrates used in this work (+0.8 V). In the second cycle, no redox wave is observed because all PEDOT sites were overoxidized during first cycle. A cyclic voltammetry (*figure 3.11B*) was also recorded between -0.2 V and +0.8 V in order to demonstrate that the process is irreversible also in this potential range. The redox wave observed for potential higher than +0.5 V decreases by increasing the cycle number, suggesting that an irreversible oxidation occurs. It is worthy to mention that a potential around to +0.8 V is kept for a few minutes during such electrochemical characterization while the PEDOT:PSS substrates were biased for 1 h. Therefore, also the electrochemical characterization shows that PEDOT:PSS is partly overoxidized during the 1 h polarization at +0.8 V.

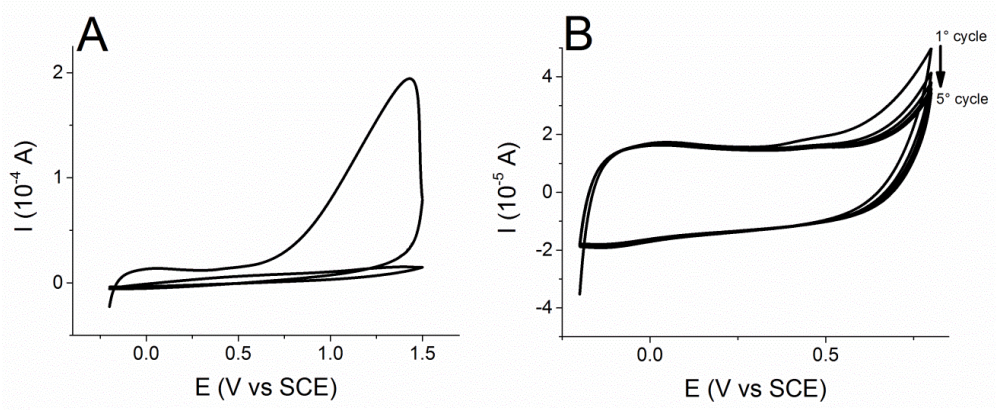

Figure 3.11: **PEDOT overoxidation.** Cyclic voltammograms recorded in phosphate buffer saline (Scan rate = 0.005 V/s) using the PEDOT:PSS substrate as working electrode, between -0.2 V and 1.5 V (**A**) and -0.2 V and +0.8 V (**B**).

3.3 Discussion

In this section, a discussion of the findings presented in the previous paragraphs is presented. In the light of AFM (*figure 3.8*) and EDX (*figure 3.10*) experiments, it is clear that the PEDOT:PSS redox state impacts the volume of the films and the concentration of ions. These findings can be explained by electrochemical processes and electroswelling [113] occurring during the application of an electrical potential to a conducting polymer film in contact with an electrolyte.

A model is proposed in *figure 3.12*, that shows a section of the not biased PEDOT(red):PSS(blue) substrate immersed in PBS (light blue) and an insert of its chemical structure (*figure 3.12A*). During reduction (negative potential), electrons enter into the film and reduce the amount of positive charge on the PEDOT chains. To maintain electroneutrality, cations (i.e. Na^+ and K^+) migrate from the solution into the film and counter-balance the negative charge on immobile PSS polyanions. The large influx of cations leads to swelling of the PEDOT:PSS film (*figure 3.12B*).

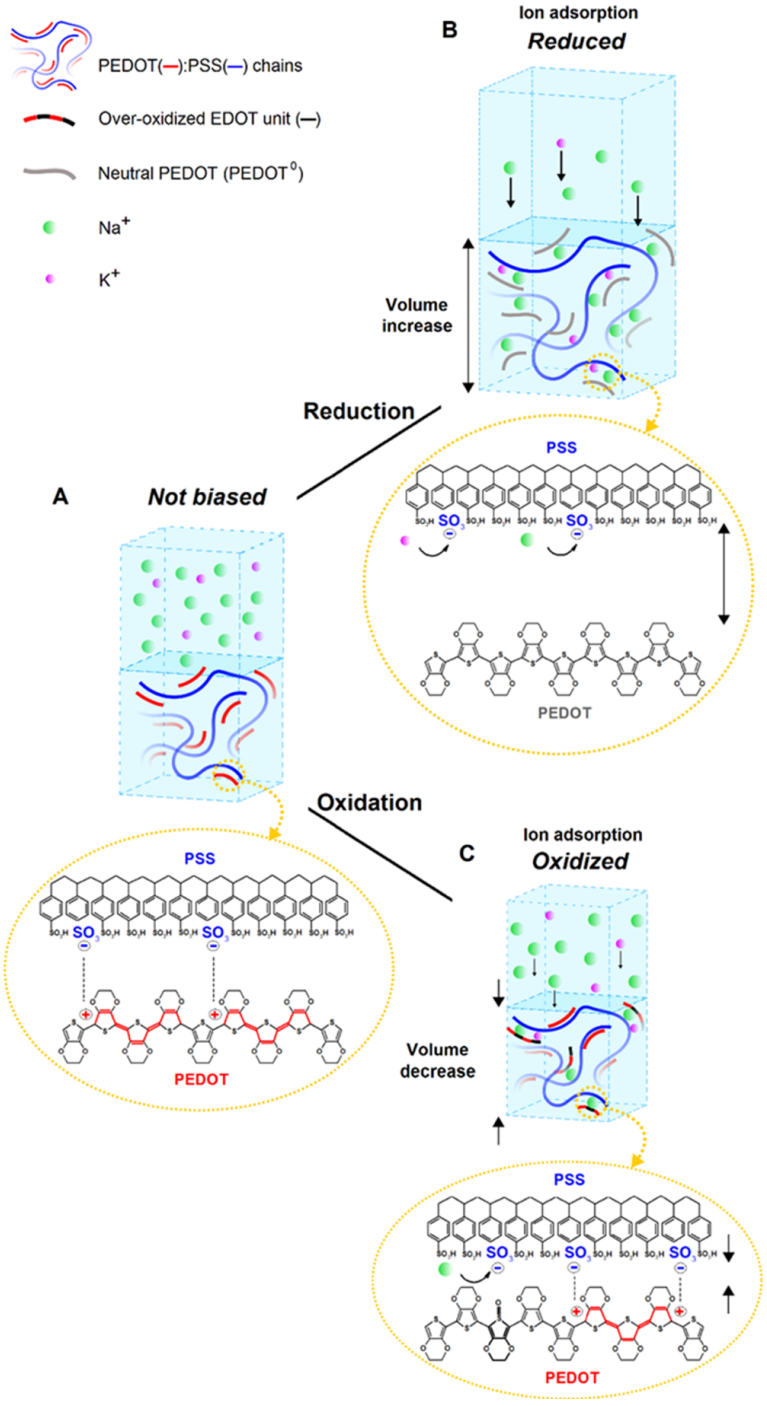

Figure 3.12: **Schematic representation of the nano-sponge mechanism.**

On the other hand, oxidation removes electrons from PEDOT and thus augments the amount of positive charge. The resulting higher charge density then leads to formation of polaronic structures which strongly interact electrostatically with the negatively charged PSS, thus reducing film volume (*figure 3.12C*).

However, during oxidation, a second competitive process takes place, that is, an over-oxidation of the material, as discussed in the previous paragraph *figure 3.11*. This irreversible process leads to the formation of neutral, sulfoxide containing units in PEDOT [114, 115]. As a consequence of over-oxidation, some cations migrate into the film to neutralize the PSS negative charge.

The three investigated PEDOT:PSS redox states (Not biased, Oxidized and Reduced) thus differ significantly in ion-concentration and volume and it is possible to consider the PEDOT:PSS film to act as an electrically controlled nano-sponge for cations. Importantly, during cell-culture experiments, the PEDOT:PSS film is no longer biased and its redox-state starts to shift towards the neutral state, following the de-biasing curve shown in *figure 3.9*. Charged films consequently release incorporated ions at a slow time-scale of hours when measurements are done at physiological ionic strength. The redox state defines which and how many ions are absorbed, and afterwards released (*figure 3.12*).

The continuous release of ions from the surface impacts on the electrophysiology of adherent cells. The resting membrane potential (V_{rest}) of cells is in general set by the balance between the intra- and extracellular ion concentration regulated by the type and properties of passive (leakage) and voltage-gated membrane channels, as explained in detail in Chapter 1. In particular, in T98G cells plated on the control substrate (polystyrene Petri dish) it was recorded a V_{rest} of about -40 mV. Considering that the overall outward current is mainly due to K^+ ion flux (*figure 3.5*) one would have expected to observe a V_{rest} similar to the equilibrium potential for the K^+ ion (about -90 mV). Furthermore, electrophysiological analyses revealed that no inward current can be induced by voltage potential stimuli lower than -30

mV and that, as reported by Olsen and Sontheimer [116] this is primarily due to an absence of inwardly rectifying K^+ channels (K_{ir}). As a result, it is reasonable to expect an accumulation of K^+ ions in the extracellular solution and thus a depolarization of the plasma membrane [116].

Therefore, the very simple setting of the T98G V_{rest} and strict dependency on the K^+ electrochemical driving forces, make this cell line a very good model to investigate the redox state of PEDOT:PSS, considering its electrical properties as a biosensor probe. In light of this, it is clear that small changes in the external K^+ concentration, especially those localized at the film-liquid interface, might be capable to interfere with the Nernst equilibrium, thus modifying the diffusive gradient and, consequently, changing V_{rest}.

In particular, it is known that membrane depolarization occurs for increasing extracellular K^+ concentration and associated decreasing driving force for K^+ efflux [117]. Similarly, when the extracellular K^+ concentration increases due to the release of K^+ previously adsorbed by the PEDOT:PSS substrates, V_{rest} depolarization occurs (*figure 3.3E* and *figure 3.13*). Indeed, in accordance with the "nano-sponge" effect, the V_{rest} recorded from cells plated on PEDOT:PSS substrates goes through a depolarizing trend from the control to the not biased form (with a V_{rest} recorded very similar to the oxidized one) and then to the reduced form following the schematic mechanism described in *figure 3.12* and 3.13.

In the previous section it was also observed that different redox states of PEDOT:PSS exhibit different effects on T98G outward K^+ currents (*figure 3.3D*). The membrane stimulation of T98G cells by voltage steps (maximum = 110 mV), showed that the outward current reached the same values when cells were plated on the control and not biased substrate, while an increase was observed on the oxidized condition and a decrease on the reduced condition.

The greatest contribution to the whole-cell ionic currents in T98G cells is due to high conductance Ca^{2+}-activated voltage-gated K^+ (BK_{Ca}) channels, which are precisely modulated by the intracellular Ca^{2+} concentration [118]. The opening of voltage-gated-calcium-channels (VGCCs) at membrane depolarization greater than -40 mV allows an inward Ca^{2+} flow [119] resulting

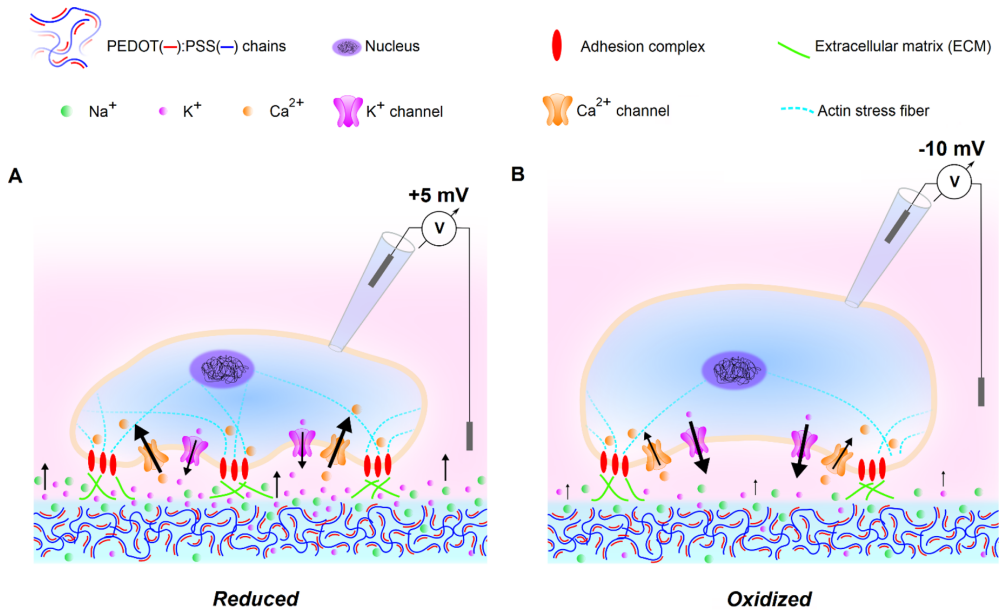

Figure 3.13: **Schematic representation of the nano-sponge effects on electrochemical cellular equilibrium.** Immediately after the polarization process, cells are plated on PEDOT:PSS substrates. Following a de-biasing/time curve the polymeric matrix relaxes, allowing ions to diffuse into the cell culture medium (light pink). Cations are thus released and the ionic concentration changes at the film-liquid interface, where cells adhere, as a function of the redox state: (**A**) PEDOT:PSS reduced substrate releases cations, increasing their extracellular concentration. Consequently, the diffusive strength across the cell membrane decreases, lowering the outward K^+ current (small arrows) and depolarizing the plasma membrane (+5 mV) which enhances the inward flow of Ca^{2+} (big arrows). This new electrochemical equilibrium boosts the adhesion process and encourages the progress of the cell cycle; (**B**) PEDOT:PSS oxidized substrate releases a lower number of cations leading to a similar but milder effect than that observed for the reduced substrate, due to a higher K^+ current (big arrows), more polarized membrane potential (-10 mV) and lower Ca^{2+} current (small arrows), resulting in slower adhesion and proliferation rates.

in increased BK_{Ca} channel activity. Despite this upregulation, the increased concentration of released cations in the medium around the cells caused by PEDOT:PSS substrates, significantly affects the diffusive gradient of K^+ across the cell membrane.

This is true especially for the reduced redox state, where the release of a higher amount of cations induces a decrease in K^+ outward flow. In accord with this, only the oxidized substrate showed a slight increase in the current amplitude, and this is the condition that appears to release the least amount of K^+. These effects are likely balanced in the not biased form. Therefore, it is possible to conclude that the resting membrane potential and outward current amplitude recordings obtained from cells plated on the different forms of PEDOT:PSS are in good agreement with the ion adsorption and release capabilities of PEDOT:PSS shown in the EDX results (*figure 3.10*), confirming that the "nano-sponge" effect can be applied to modulate the cell electrical functions.

Interestingly, redox forms of PEDOT:PSS are also responsible for strong changes in cellular adhesion properties and cell proliferation. Indeed, these two biological parameters increased in T98G cells plated on the oxidized and the reduced substrates compared to the not biased one, matching the same trend of the V_{rest} (*figure 3.3*). It has been recently found that membrane depolarization affects endothelial cell stiffness by influencing the polymerization state of cortically located actin filaments [117]. This means that depolarized T98G cells, such as those plated on the reduced PEDOT:PSS substrate, may have a better and faster adhesion response compared to stiffer cells plated on relatively less depolarizing substrates such as the not biased or the oxidized ones, according to what showed in *figure 3.13*.

Another important factor to be considered when talking about cell adhesion is the intracellular Ca^{2+} availability; indeed, it plays a key role in the regulation of many of the molecular pathways essential for cell movement, such as the dynamics of the actin cytoskeleton and the formation and disassembly of cell-substratum complexes [120], as shown in detail in Chapter 1. Thus, an increase of the cytosolic Ca^{2+} availability at the first steps of

the focal adhesion process, consistent with T98G cells showing a depolarized plasma membrane, might result in a better-triggered machine improving adhesion capability, as observed for reduced substrate.

As mentioned in Chapter 1, cell membrane potential and replicative boost are strictly interrelated. For example, the pre-mitotic phase of replicating cells exhibits reduced K^+ channels functionality and a significantly depolarized membrane potential [70]. This is in agreement with previous findings reporting that sustained depolarization is able to induce DNA synthesis and mitosis in cells [67].

Furthermore, Ca^{2+} has been recognized as a strategic mediator of intracellular signals implicated in the control of mitogenic pathways [121], and thus its intracellular increase in depolarized cells may trigger mechanisms required for cell proliferation and accelerate the replicative boost, in accordance to what said for adhesion. Therefore, the increased proliferation rate observed on the reduced PEDOT:PSS form can be explained by the capability of the "nano-sponge" effect to induce the depolarization of V_{rest}, which encourages the overcoming of the checkpoint between the phase G_2 and M of the cell cycle and supports the replicative process, making available a greater amount of intracellular Ca^{2+}.

All the above results indicate that K^+ ion driving forces play a crucial role in modulating the replication of cells, in particular tumoral ones. The depolarization of the membrane potential was also observed in the oxidized and not biased substrates, but less evident as expected.

To assess the effects of the redox state of PEDOT:PSS substrates with another kind of cells, human dermal fibroblasts (hDF) were chosen as a model of a healthy cell. In this case it was observed that the ion exchange capability of PEDOT:PSS film is unable to sufficiently modulate the plasma membrane responses, as well as the adhesion and proliferation rates, which remain very similar for all the PEDOT:PSS forms tested (*figure 3.6*). A possible explanation for this behavior, as I mentioned earlier, might be the different electrophysiological resting state of hDF; indeed, as observed in (*figure 3.7*), these cells show a value of V_{rest} that is much more depolarized compared with

that of T98G plated on control Petri dish, in addition to a whole-cell outward current amplitude much smaller, practically halved. These observations point to a less reactive electrophysiological setup for hDF cells, and then lower driving forces for the cations outward fluxes, thus leading, in the case of an increase of the extracellular ionic concentration, to under-threshold effects.

Chapter 4

Cellular response to electric fields

The main objective of this Chapter is the description of some preliminary results obtained with the electronic device capable to create and control galvanotactic events, described in Chapter 2. In the first part, a brief introduction to galvanotaxis is given; subsequently, qualitative and quantitative analyses of the recorded data are presented and discussed in detail.

4.1 Introduction

The discovery that cells show orienting and migrating properties in a specific direction relatively to a direct current electric filed (dc EF) dates to the late nineteenth century [122] and has been named galvano- or electro-taxis. *In vitro* experiments revealed that cells sense EF from a threshold value of 10 mV/cm [123], while dc EF with magnitudes on the order of 0.1-10 V/cm are required for observing the electrotaxis phenomenon [123, 60]. Recent meta-studies have suggested that electrically sensitive cell lines are the rule, not the exception [60, 124].

The majority of cell types prefer to migrate toward the cathode, as for neural crest cells, fibroblasts, keratinocytes, chondrocytes, rat prostate cancer

cells, several glioma cell lines and epithelial cell types [125, 126, 127, 128, 129, 130, 131, 58, 132]; while only few move to the anode, among them there are corneal endothelial cells, bovine lens epithelium, human granulocytes, and human vascular endothelial cells [133].

Both speed and direction of the movement are voltage-dependent [134]. Although galvanotaxis may seem unlikely *in vivo*, it is quite prevalent, and many data suggest that it is implicated in cell movements, that occur throughout development, morphogenesis and regeneration. Cell motility properties are involved in the regeneration of damaged tissue and wound healing; cell migration is also considered the main cause behind the metastatic process [59, 135]. Furthermore, during embryogenesis, the motion of cells toward a specific target is a crucial feature for tissue organization and organ formation [136, 137].

The methods of applying EF, as well as the assays to perform electrotaxis experiments, have changed little over the past several decades [138]. In particular, despite the use *in vivo* of the EF occurs necessarily in a "non-contact" mode, the majority of the *in vitro* electrotaxis experiments [138, 139, 140, 141, 142] are conducted involving metal electrodes directly or indirectly (through agar or salt bridges) inserted into the culture medium ("contact" mode). In both cases, the main physics result is a different diffusive pressure on the two side of the cell, achieved passively by a reorganization of ions ("non-contact" mode), or actively by their fluxes inside the culture medium ("contact" mode). This has led to some confusion about the physical forces involved in the galvanotaxis phenomenon; however, what appears clear today is that ion channels play a key role in driving this process.

Therefore, to study electrotaxis in an *in vitro* 2D environment, it has been designed and built an experimental system consisting of a programmable, high performance, electronic platform and a special holder for the galvanotaxis chamber that allows to apply direct current (dc) or alternating current (ac) EF of different waveforms and frequencies, in both the "contact" and "non-contact" modes. It was also inserted into the system a resistance able to return the current measure along the time.

In order to verify the functionalities of this system and to set all the experimental parameters capable to reproduce the electrotaxis phenomenon several tests were performed, monitoring the effects of EF and current density on the motility function of a human tumor cell line (T98G).

4.2 Results

The work started by testing the experimental system measuring the current in the "contact" mode: the anode was connected to the 3.3 V output of the Arduino2 platform and the cathode to the reference ground as shown in *figure 4.1* at left. The graph in *figure 4.1* on the right shows the ion current measured as described in Chapter 2 (*figure 2.6*): after switching on the circuit, the current drops extremely fast and, within twenty minutes, reaches a plateau at 200 μA, which is about 30% of the value at time zero.

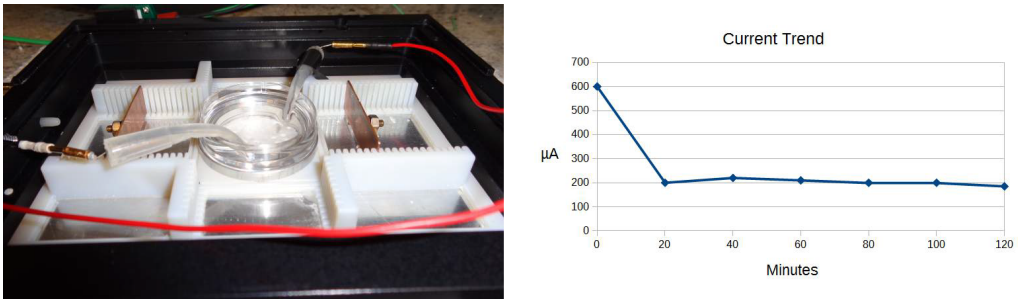

Figure 4.1: **Current measurement as a function of time.** (**left**) The support plate for 35 mm Petri dish appears in the "contact" mode: the two Ag/AgCl electrodes are immersed into the culture medium by agar bridges and connected to the anode (left wire) and to the cathode (right wire). In this experimental set-up an electric current flows through the biological sample. (**right**) Graph of the current measured during a time-lapse experiment by a calibrated variable resistor in series with the electrodes.

The current is expected to change with time, because ions and charged molecules of the colture medium (aminoacids and proteins for example) tend to accumulate near the electrodes and may also polymerize, thus increasing the resistance of the circuit, but this happens much faster than expected. Moreover, it was observed the formation of bubbles around the cathode, confirming the generation of secondary chemical products.

In our experimental condition, the current's fluctuation might be unpredictable and the cellular movement during the current delivering is difficult to observe.

Therefore, the system was tested in the "non-contact" mode (*figure 2.7* Chapter 2) by placing the copper plates at 42.5 mm from each other (the minimum distance possible next to the outer sides of the Petri); applying a voltage of 20 V we were able to generate an EF of 4.7 V/cm.

We observed the behavior of seven cells by analyzing their morphology, speed and heading for each frame acquired during the 120 min of the experimental section.

In *figure 4.2* we show two sample images, at time 60 min (t = 1h, A) and at time 120 min (t = 2h, B), where the morphology of cells before and after the EF exposure can be observed. The cells numbered as "1" and "2" present at t = 1h an elongation oriented along the perpendicular to the direction of the EF, that progressively increases throughout the time of stimulation.

The quantitative analysis of speed and heading expressed in the polar graphs (*figure 4.3*) indicate that the cells "1" and "2" increase their speed but only the "2" modifies the direction of its motion. In addition, also cell "8" shows an elongated shape at t = 1h (*figure 4.2A*), but not perpendicularly oriented with the EF. In this case, the stimulus seems to affect only the heading and not the velocity (*figure 4.3*).

This is the only cell, among 7, that shows a leading edge (the part of the cell that start to advances) polarized along a new direction after the EF application, indicating a changing of the heading motion from the baseline phase to that of stimulation.

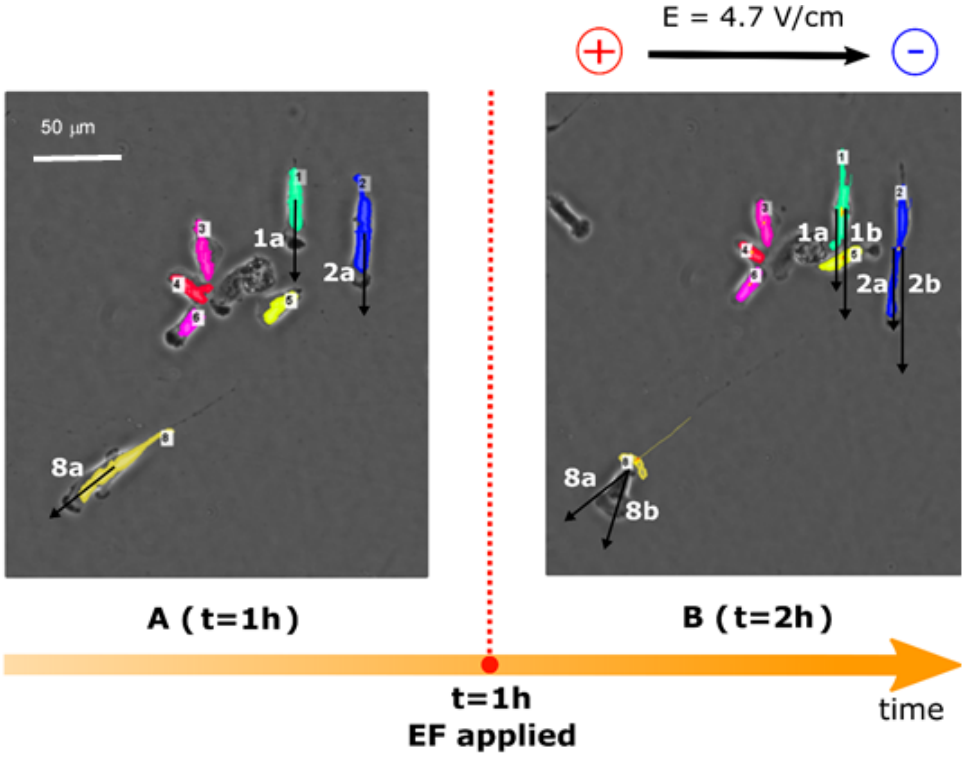

Figure 4.2: **Cell migration during the effect of the EF**. Sample Images of the visual field acquired in time-lapse phase contrast microscopy (100× magnification) **A**) after 60 min of baseline (without EF) and **B**) after 60 min of exposure to an EF of E = 4.7 V/cm. Black arrows represent the cell direction and the length of elongation.

Cells numbered as "3", "4", "5" and "6" show a more condensed morphology during the entire experiment and the EF does not seem to have effect on the considered parameters (*figure 4.3*).

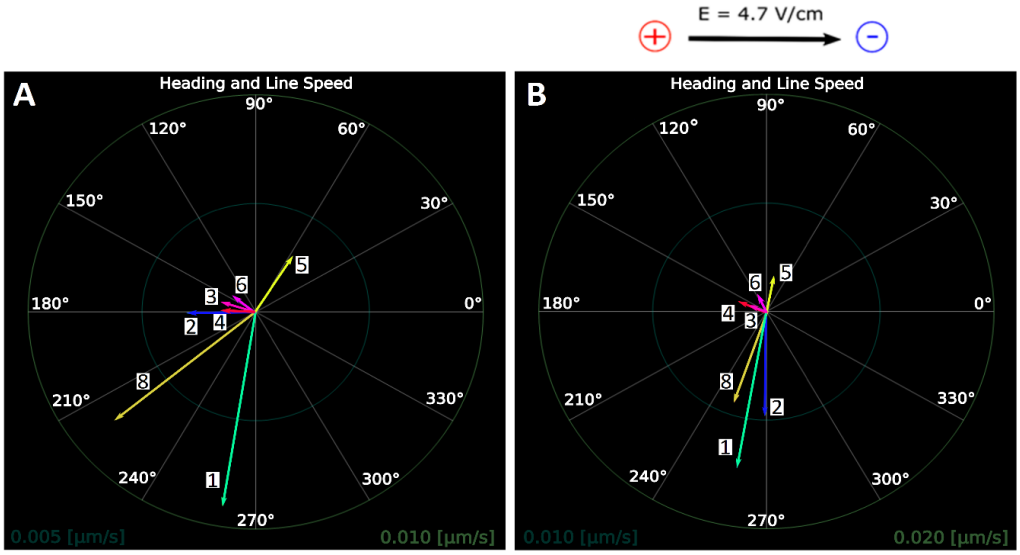

Figure 4.3: **Direction and speed of cells before and after EF applied**. Polar graph **A**) during the control phase (from time 0 to 60 min) and **B**) during the exposure to an EF of E = 4.7 V/cm. The direction of the coloured vectors indicates the cells heading, and their length the line speed. Numbers correspond to *figure 4.2*.

4.3 Discussion

In summary, among 7 cells, 4 can be considered static (do not show susceptibility to motion during the observation time adopted) and the EF seems to have no effect, while 3 cells are characterized by a more active behaviour and they appear to be affected by the EF.

The preliminary data obtained in the "non-contact" mode, although statistically weak, might indicate that an EF of 4.7 V/cm can affect the behaviour of T98G cells but not homogenously. In fact, a net movement of cell towards one of the electrodes was not recorded, almost half of the cells considered showed an alignment along the perpendicular to the electric field, in accordance with the established literature [143].

As shown in *figure 4.4A*, cell polarization represents the first clue of the electric field effects on cells in a 2D galvanotactic chamber, because at first

they align themselves perpendicular to the EF, and only later they begin to move towards one of the electrodes, maintaining this elongated morphology during all the motion time and never along the direction of migration.

In addition to the electrophoresis and electro-osmosis forces mentioned above, applied electric fields of 1-15 V/cm can alter significantly the cell's transmembrane potential, especially in the "contact mode". For a flattened cell on a culture dish, a linear voltage drop occurs over the surface of the cell in the extracellular medium, if the current is uniform and parallel to the substratum.

The transmembrane potential of the cell thus becomes a function of position, which is given by:

$$\Delta\psi(r,\theta) = \Delta\psi_0 - E|\vec{r}|cos\theta \tag{4.1}$$

Where $\Delta\psi$ is the initial transmembrane potential, E is the applied electric field strength, and r and θ are positional coordinates from the cell's electrical center as defined in *figure 4.4B*.

For a cell of 100 μm length in an electrical field of 2 V/cm, the anode-facing membrane will be hyperpolarized by 10 mV over its initial transmembrane potential, whereas the cathode-facing membrane will be depolarized by 10 mV. Note, however, that the transmembrane potential along the perpendicular midline of the cell ($\theta = 90°$, $270°$) remains at $\Delta\psi_0$.

The programmable electronic platform and the support plate for 35 mm Petri dish that we developed in order to study the capability of cells to move on a 2D environment and monitor the effects of the galvanotactic stimulus, are oriented to improve the scientific approach, being a system particularly adapted to cover a wide range of possible experimental parameters. The Arduino2 prototype described here is capable to configure multiple EF driven by dc and/or ac currents with different intensities, strengths and waveforms, representing a system particularly adapted to cover a wide range of possible experimental conditions as strongly suggested by the researchers operating in the electrotaxis field [144].

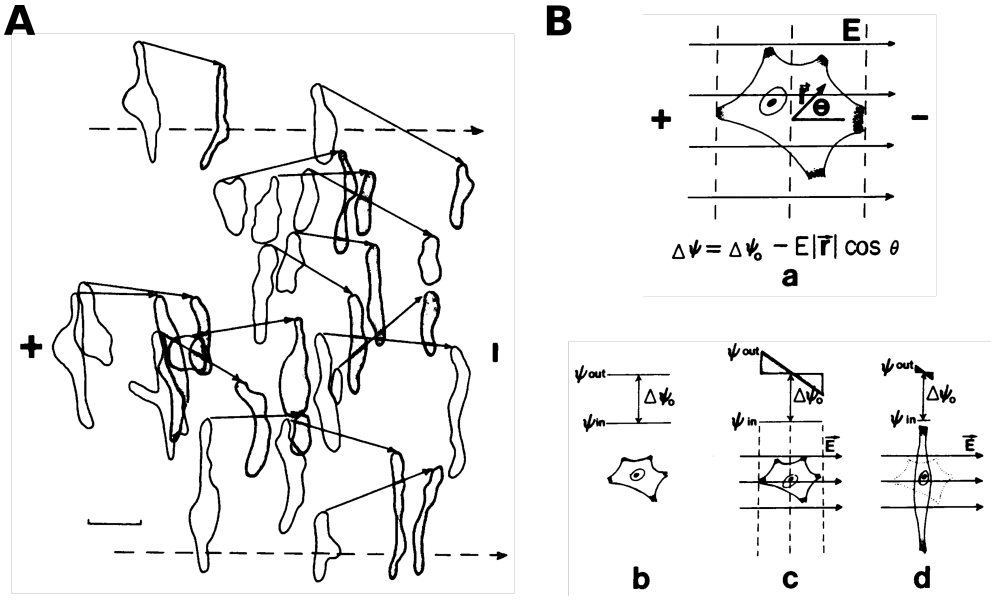

Figure 4.4: **Morphology of cells under the action of an electric field and effect on membrane potential**. (**A**) Lateral migration of cells exposed to an electric field of 12.5 V/cm. Solid arrows indicate lateral translocation of the elongate cells over 35 min at an average rate of 3.6 ± 0.7 μm/min (scale bar 50 μm). (**B**) Transmembrane potential of a flattened cell in a uniform dc electric field in "contact mode": a) the centre of the voltage drop that occurs across the cell lies midway between the furthest extremities of the cell in the direction of the field. (b and c) Transmembrane potential of a cell before (b) and after (c) field application. Anode- and cathodefacing sides of cell become hyperpolarized and depolarized, respectively. The midline of the cell is not perturbed. (d) Withdrawal of protrusions and elongation produce a perpendicular cell. The induced transmembrane potential perturbations are minimized; adapted from Cooper and Keller, 1984 [143].

However, other experiments are planned with the aim to increase the statistical ensemble and then confirm these preliminary results. Furthermore, future improvements of the device are oriented toward the automatization and the on-line adjustment of the parameters controlled by the electronic platform, for example interfacing a flexible software that allows writing simple codes.

In addition, the apparatus can be equipped with a feedback tool so that to adapt and tune the current source to keep constant the inducted current, if desired.

The use of a conventional dish-based device instead of microfluidic ones, despite several limitations such as low throughput and non-uniform EF distributions [145] allows to easily operate, visualize isolated and collective cell migration, design a 3D cellular environment, and monitor voltage values into the medium with recording electrodes connected to an operational amplifier. Moreover, it allows on-line measurements of the cellular polarization degree by the use of the patch clamp technique.

Chapter 5

Ion channels and Progeria Syndrome

In this Chapter the results obtained studying the ageing mechanisms occurring in the Hutchinson-Gilford Progeria Syndrome (HGPS) are presented. Starting from a brief description of the disease, the findings regarding the bioelectric properties of hDF affected by HGPS, as well as their adhesion and proliferation results, compared with those of healthy hDF, are described in detail. Finally, a possible interpretation of the accelerated aging mechanism occurring in HGPS, in the light of a demonstrated overexpression of BK_{Ca} channels is discussed.

5.1 Introduction

Hutchinson-Gilford Progeria Syndrome (HGPS) is a rare fatal genetic disorder characterized by various clinical features and phenotypes of premature ageing. The disorder has a very low incidence rate, occurring in an estimated 1 per 8 million live births. Children born with HGPS typically appear normal at birth, but within a year they begin to display symptoms related to a global premature aging phenotype including hair loss, diminished subcutaneous fat, cardiovascular diseases and skeletal abnormalities. The notable thing in

HGPS is that there is no apparent alteration of the central nervous system. On average, death occurs at the age of 13 from stroke, myocardial infarction, heart failure or atherosclerosis [146, 147]. HGPS is caused by accumulation of an alternative splice variant of lamin A, progerin, that results from erroneous activation of a cryptic splice site within the *LMNA* gene [148, 149, 150]. Progerin is a truncated form of prelamin A, the lamin A precursor, which is also accumulated, as full-length protein, in HGPS and other laminopathies and affects nuclear organization, chromatin dynamics, regulation of gene expression and epigenetic regulation [151, 152, 153], as shown in *figure 5.1*.

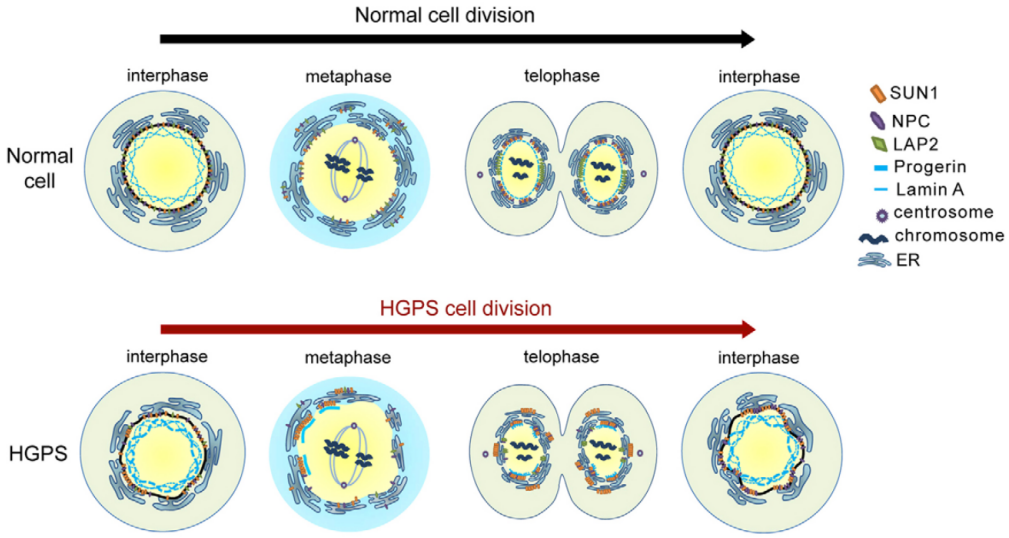

Figure 5.1: **Cartoon showing the role of Progerin in HGPS pathogenesis.** After the breaks down of the nuclear membrane during mitosis, progerin forms insoluble aggregates with another protein (SUN1) in the endoplasmic reticulum of HGPS cells (bottom), but not in that of normal cells (top). During the reassembling of the nuclear envelope, these aggregates negatively interfere with the recruitment of nuclear-envelope-associated proteins from the endoplasmic reticulum or the cytoplasm to the inner nuclear membrane, thereby altering the morphology of the nucleus; adapted from Z. J. Chen et al., 2014 [154].

Progerin has been also detected at low levels in normal ageing cells [155] suggesting that HGPS cells are good candidates for the study of the physiological mechanisms of ageing [156, 157]. However, the detailed cellular mechanisms causing clinical phenotype of HGPS is still unclear.

It has been recently shown that the expression on human dermal fibroblasts (hDF) membrane of large-conductance calcium-activated potassium (BK_{Ca}) channel decreases with the silencing of *LMNA* [158]. Using a system-biology approach Sokolowski and colleagues identified the BK_{Ca} channels interactions with proteins and pathways of a survival/apoptotic nature indicating a specific involvement of BK_{Ca} channels on cell's viability. Furthermore, in a previous study it was showed that BK_{Ca} expression on normal hDF membrane is remodeled as a function of age [19] focusing on this channel a possible role as a marker for early diagnosis of pathologies related to aging.

In general, K^+ channels play an active role in cellular replicative mechanisms, in the appropriate adjustment of cell volume, influence cytosolic Ca^{2+} concentrations and modulate cell resting membrane potential [70].

In this work, the effects of the pathology on the activity of BK_{Ca} were investigated by analyzing the outward current amplitudes in hDF obtained from juvenile patients affected by HGPS and comparing them with those from healthy juvenile donors used as control group. In order to assess the correlation between the BK_{Ca} channels activity and the replicative process, the adhesion and proliferation rates have been tested in treated and un-treated hDF cells with a selective BK_{Ca} inhibitor.

5.2 Results

5.2.1 K^+ current increases in Hutchinson-Gilford Progeria Syndrome (HGPS)-affected cells

In order to compare bioelectrical properties of cells affected by Hutchinson-Gilford progeria syndrome with those of healthy donors of the same age, the

whole-cell outward currents of primary hDF cells, obtained from two juvenile (9 years old) donors and two patients (6-9 years old) affected by HGPS were considered.

The currents recorded in both cell populations show similar characteristics those described in Zironi et al., 2010 [19], that is: noisy traces due to the large conductance of the BK_{Ca} channels, starting activation at about 10 mV and a semi-complete inhibition after the specific inhibitor Iberiotoxin (IbTx) loading (*figure 5.2A, B*).

The current amplitude analysis on a large population of cells revealed that, starting from 70 mV of stimulus, the HGPS group is characterized by a consistent higher mean value compared to that obtained from Juvenile group (*figure 5.2A, B*).

To confirm this result, the mean current densities for each experimental point were considered, normalizing the current amplitudes to the mean membrane capacitance values. This analysis highlighted that also the HGPS cells current density has the same increment compared to control (*figure 5.2C*) clearly suggesting that the pathology induces a large increase of the BK_{Ca} channels weight on eliciting the outward current fluxes without affecting cell size.

Further details about the parameters estimated by patch clamp recordings are reported in *table 5.1*.

Moreover, the recordings obtained perfusing cells with a solution containing the non-selective K^+ channels blocker Tetraethylammonium (TEA 10 mM), showed that the whole-cell outward currents are almost completely blocked (*figure 5.3*), confirming definitely that they are gated through K^+ channels.

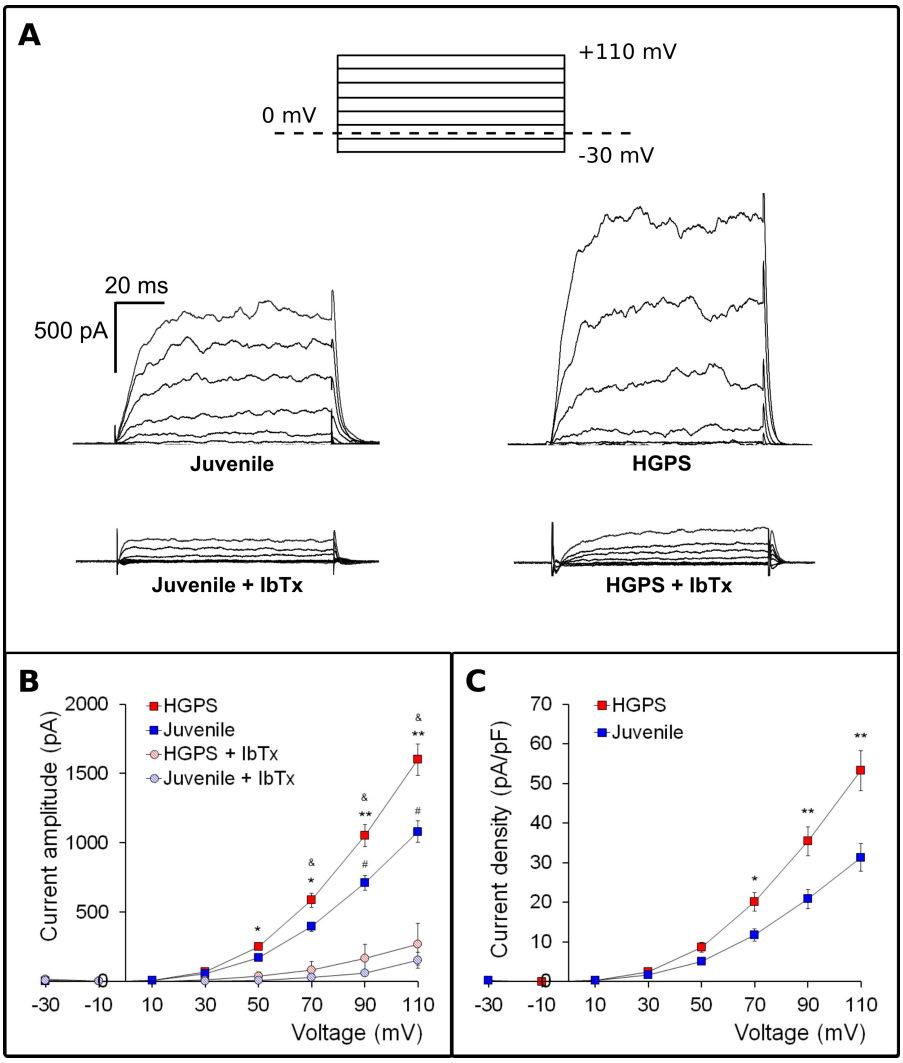

Figure 5.2: **Outward currents patch-clamp recorded in whole-cell configuration.** (**A**) Representative examples of current traces recorded in hDF obtained from a juvenile donor and a patient affected by HGPS, before and after 100 nM IbTx application. (**B**) Average ± SEM of current-voltage relationships (I-V) recorded in hDF obtained from healthy donors (Juvenile, n = 38) and patients affected by HGPS (n = 80), before and after 100 nM IbTx application. (**C**) Average ± SEM of current density-voltage relationships (J-V) of the same cells described in (B) (referred only to control cells). Juvenile vs HGPS: *p<0.05; **p<0.01; Juvenile vs Juvenile + IbTx: #p<0.05; HGPS vs HGPS + IbTx: &p<0.05.

	Juvenile n = 38	**HGPS** n = 80
Mean amplitude (pA)	1081 ± 77	1600 ± 113
t-test	p<0.01	
Capacitance (pF)	39.9 ± 2.2	36.2 ± 1.3
Radius (μm)	17.8 ± 0.4	17.0 ± 0.3
Mean current density (pA/pF)	31.3 ± 3.5	53.2 ± 5.1
t-test	p<0.01	

Table 5.1: **Summary of patch clamp experiments.** Current amplitude, capacitance, radius and current density values obtained at +110 mV of stimulation step. All p values calculated by Student's t-test.

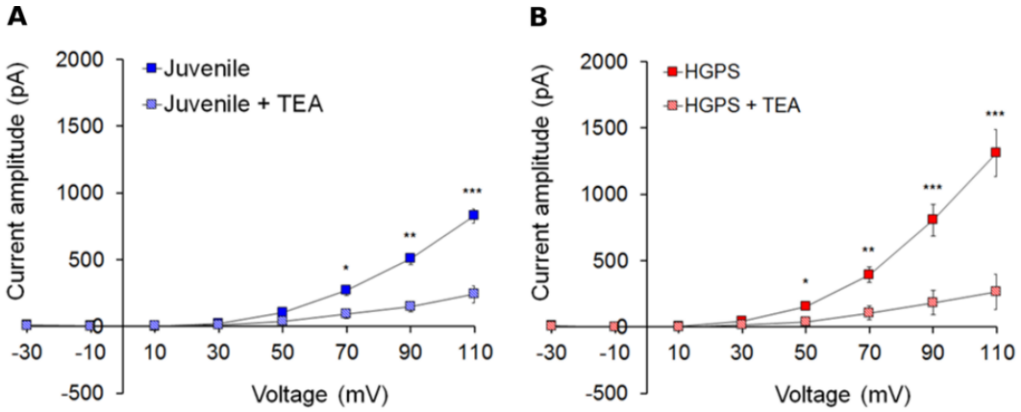

Figure 5.3: **Effect of Tetraethylammonium on Juvenile and HGPS cells.** Average ± SEM of current-voltage relationships (I-V) recorded in hDF obtained from healthy donors 9 years old (**A**) and patients affected by HGPS (**B**), before (n = 6) and after (n = 4) 10 mM TEA application. Control vs TEA: *p<0.05; **p<0.01; ***p<0.005. All p values calculated by Student's t-test.

5.2.2 Expression of BK_{Ca} channels increases in HGPS cells

A semi-quantitative analysis of the large conductance Ca^{2+}-activated K^+ channel was carried out using a polyclonal IgG against an extracellular peptide of the α-subunits (see Chapter 2) in hDF obtained from the Juvenile and HGPS groups. The results showed in *figure 5.4* indicate that hDF affected by HGPS are more positive for BK_{Ca} channels compared to Juvenile, being the mean fluorescence intensity of the HGPS group about 30% higher. The differences between Juvenile and HGPS current amplitudes are obtained while membrane are clamped at voltage potentials that make BK_{Ca} channels totally open. Knowing the cellular membrane potential (V_m) and the current amplitude elicited, the Ohm's law can be solved to calculate the total K^+ conductance, which depends on both the number and yield of the channels. This, together with the immunofluorescence results, indicates an increase of the BK_{Ca} channels number rather than activity.

5.2.3 Impaired proliferation capabilities in HGPS hDF involve BK_{ca} channels

Two groups of hDF (Juvenile and HGPS) were monitored every day for four days; the number of cells normalized to the first 24 h is graphed in *figure 5.5A*. At 96 hours, the comparison between the proliferation rates of hDF obtained from juvenile patients affected by HGPS and from healthy donors shows that the replicative capability is significantly impaired ($p<0.01$) by the syndrome. The same population of cells has been monitored two hours after seeding, the percentage of adherent HGPS hDF is about 20% lower ($p<0.05$) compared to that obtained from Juvenile group (*figure 5.5B*). These two results clearly confirm that HGPS impacts both adhesion and proliferation capabilities of cells, significantly impairing these processes. Interestingly, comparing this result with the current amplitudes (*figure 5.2*) we observe that a lower current amplitude corresponds to a higher proliferation rate, suggesting a causal

relationship between the electrophysiology and the proliferation boost. To assess whether BK_{Ca} channels are involved in the process, cell growth and adhesion experiments were performed, keeping cells in replicative conditions from 0 to 96 hours in the presence or not (Control) of 100 nM IbTx. The inhibited activity of the BK_{Ca} channels by the toxin negatively affects only the proliferation rate of HGPS cells in comparison to Control (*figure 5.5A, B*). The results indicate that the proliferation process involves BK_{Ca} channels activity in HGPS hDF only, with minor involvement, if any, in control cells. The detrimental effect on the adhesion rate may depend on other causes associated with the pathological state of these cells.

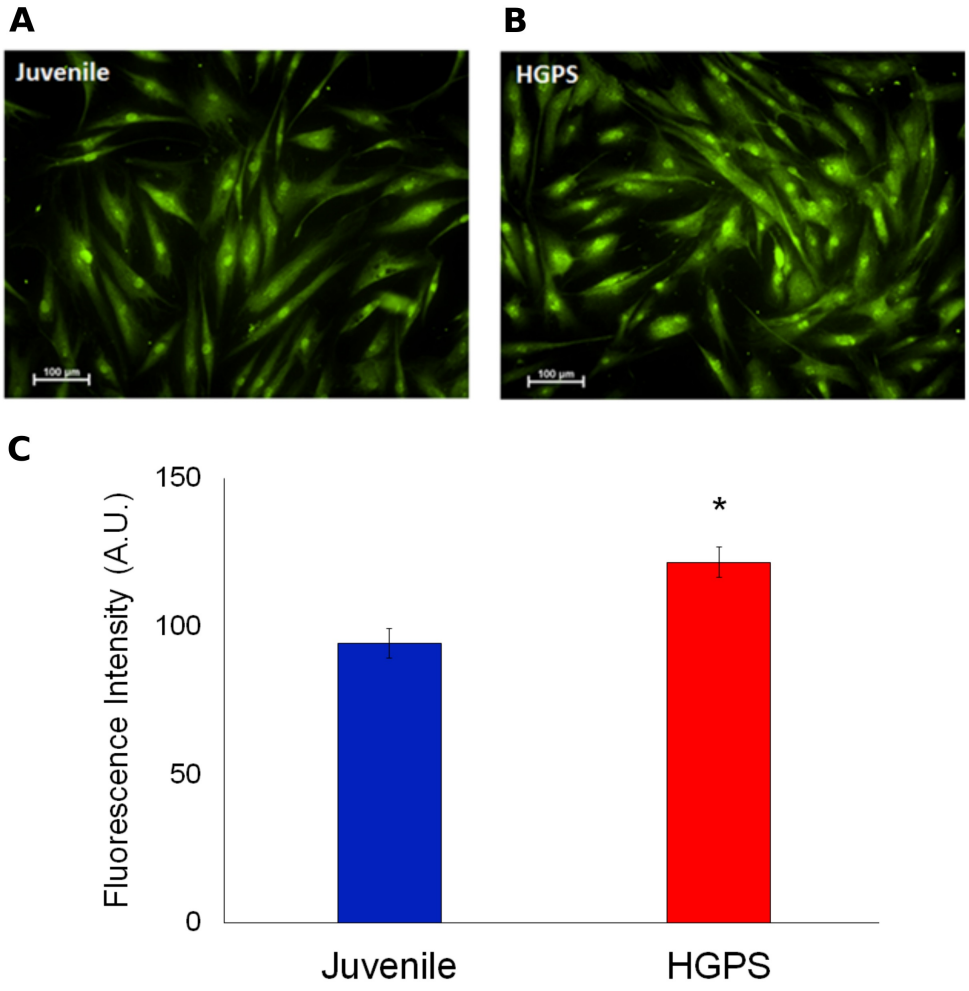

Figure 5.4: **Immunofluorescence detection of the BK_{Ca} channel.** The optical imaging samples of isolated hDF obtained from juvenile (**A**) and HGPS (**B**) donors incubated with anti-BK_{Ca} α-subunit antibody. Bound antibody was visualized by fluorescein 5-isothiocyanate (FITC)-conjugated antibody and observed with epifluorescence filter for FITC at 200× magnification. (**C**) Quantification of mean fluorescence intensity A.U. ± SEM. Juvenile vs. HGPS *p=0.0066.

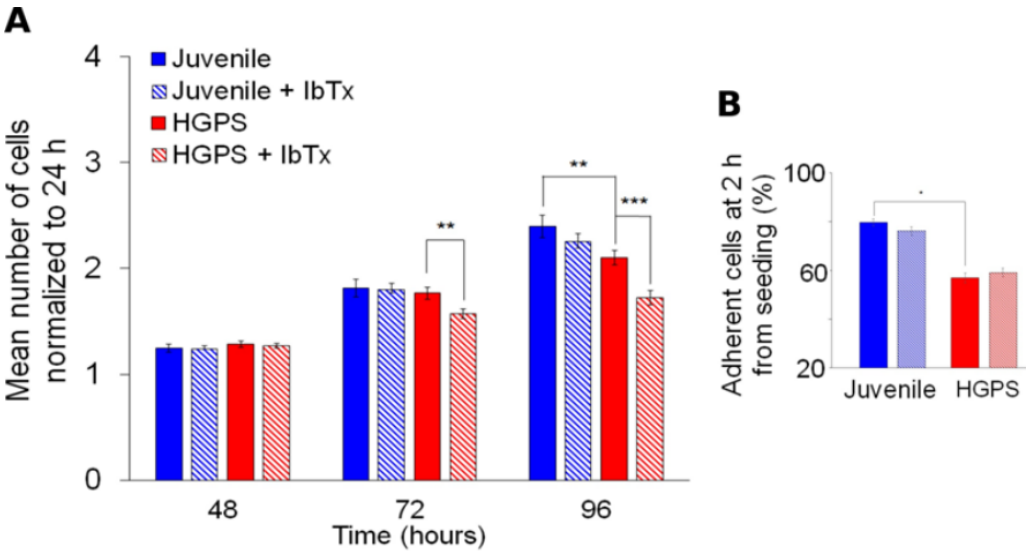

Figure 5.5: **Proliferation and adhesion rates without and with the BK_{Ca} inhibitor IbTx.** (**A**) Mean number ± SEM of hDF counted in a phase-contrast image field of 0.68 mm^2 (100× of magnification) at 24, 48, 72 and 96 h after seeding and then normalized to 24 h. Juvenile and HGPS hDF were allowed to proliferate in wells untreated (HGPS n = 21; Juvenile n = 33) and treated by 100 nM IbTx (HGPS n = 18; Juvenile n = 33), added after 24 h from seeding. (**B**) Average percentage ± SEM of adherent hDF counted 2 h after seeding, without (HGPS n = 24; Juvenile n = 57) and with 100 nM IbTx (HGPS n = 26; Juvenile n = 53); the image legend is the same as figure (A(. *p<0.05; **p<0.01; ***p<0.001.

5.3 Discussion

The evidences described can be summarized as follows: i) human dermal fibroblasts (hDF) obtained from patients carrying a G608G *LMNA* mutation overexpress BK_{Ca} channels on plasma membrane; ii) adhesion and replicative capability tested in the same populations are impaired in HGPS cells, but only proliferation shows a correlation with the overexpression of BK_{Ca} channels.

The BK_{Ca} channel expressed on hDF membrane consists of pore-forming, voltage- and calcium-sensing α-subunits in association with a regulatory subunit ($\beta 1$), as explained in Chapter 1. The α-subunits are encoded by a single gene (KCNA1), which undergoes extensive alternative pre-mRNA splicing leading to a different complement of BK_{Ca} channel α-subunits and providing tissue-specific features of activity, trafficking and regulation [159].

As other systemic laminopathies, HGPS is characterized by impressive alterations in the nuclear profile and in chromatin organization, due to accumulation of unprocessed prelamin-A. Because the lamin A serves as a docking site for transcription factors and chromatin-associated proteins, a dysfunctional lamin, as progerin, may influence gene expression in several ways [160, 161]. This might in turn affect the encoding process of BK_{Ca} channels in one or more steps, even indirectly, acting for example on support proteins that participate in the assembling of the channel on the plasma membrane, leading in general to a non-programmed modulation of the BK_{Ca} channel protein expression.

How the HGPS impacts the proliferative capability of hDF cells is still a controversial issue. A first study showed that low-passage HGPS hDF are highly proliferating compared to normal cells, while high-passage HGPS cultures are characterized by significant increase in the rate of apoptosis [162]. This behavior can be ascribed to an increase of progerin levels that occurs with increasing passage number. This study pointed out that cells obtained from HGPS patients are characterized by a lower replicative boost compared to those obtained from non-affected subjects of the same age (*figure 5.5A*). Interestingly, HGPS cells also show a direct effect of BK_{Ca} channels activity

on replicative boost, but not on the adhesion process (*figure 5.5B*). The negative response of adhesion to BK_{Ca} channels blocking is an important result because it rules out any dependence between these two processes.

BK_{Ca} channel is the main one expressed on the hDF membrane. Thanks to its large conductance for outward potassium (K^+) fluxes and sensitivity for voltage variation and calcium concentration it takes a crucial gating role on setting the V_m. Moreover, it is known that changes of the membrane potential play a crucial role in several physiological cellular pathways [163], including cell cycle and proliferation, and this is true for hDF as well as for other cell types (lymphocytes, astrocytes, and Schwann cells) as explained previously in Chapter 1. In fact the modulation of V_m is required for both G_1/S and G_2/M phase transitions. Hyperpolarization serves for G_1/S progression and depolarization for the G_2/M transition, respectively.

This defines a model that outlines a rhythmic oscillation of membrane potential throughout the cell cycle, with a spike in hyperpolarization, occurring before DNA synthesis, followed by a prolonged period of depolarization necessary for mitosis. Voltage-dependent K^+ channels, including BK_{Ca} channels are the main responsible of this modulation. In fact their expression or activity changes across stages of the cell cycle [70, 164] indicating a key regulatory role in the proliferation process.

In view of this, it becomes very important to contextualize BK_{Ca} channels functionality of HGPS cells to their membrane potential and then to their proliferation functionality. The overexpression of the BK_{Ca} channels α-subunit observed in HGPS cells results into a greater outflow of K^+ in response to physiological depolarization of the cell membrane. This may elicit a feedback effect that tends to restore a more polarized electric state with respect to healthy cells, leading to difficulties in cell depolarization, the condition required for mitosis, thus resulting in a decrease of the proliferation rate.

This effect ultimately leads to cellular senescence, a well-documented state in HGPS fibroblasts [165], which has emerged as a potentially important contributor to aging and age-related disease. Indeed, the number of cells in tissues and organs that show a senescent behavior increases with age [166].

Cellular senescence has a crucial tissue remodeling role in organisms, because senescent cells show a relatively short half-life being recognized and cleared by immune cells. In fact, this is an efficient way to eliminate aged cells, which have accumulated damage during their life, or malignant cells, thus contrasting tumor development [167]. For example, the oncogene-induced senescence (OIS) can constitute a failsafe program that restricts tumor development. Moreover, it has been proved that oncogenic stress may induce senescence in cells, acting on the BK_{Ca} α-subunit expression, increasing it, but also on its relocation from the cytoplasm to the membrane, leading to a change in the channels functionality and then in membrane potential [168].

Therefore, potassium channels functionality, in particular BK_{Ca} channels, as demonstrated in this study, may represent an interesting perspective to better understand the aging effects observed in patients affected by HGPS, but also in other diseases characterized by forms of premature aging.

Conclusions

This work was focused on the bioelectrical properties of the plasma membrane, studying the cellular response to different experimental conditions and stimuli. In particular, monitoring the potassium voltage-gated ion channels activity, it was possible to assess: i) the interaction between cells and organic films made by poly(3,4-ethylenedioxythiophene):poly(styre-nesulfonate) (PEDOT:PSS) with different oxidation states, ii) cellular migration under the influence of an electric field, and iii) premature aging process in cells obtained from donors affected by Hutchinson-Gilford Progeria Syndrome (HGPS).

PEDOT:PSS thin films produced by electropolymerization have been used as culture substrates for cell growth. The redox state of this polymer has been modified through electrochemical oxidation and reduction for 1 hour in buffer solution, applying a voltage of +0.8 V and -0.9 V, respectively. In this way, it was possible to obtain three types of PEDOT:PSS substrates: Not biased, Oxidized and Reduced; tested with a tumor cell line (T98G) and with human dermal fibroblasts (hDF). Previous findings assure that the stability over time of the redox state is maintained for at least 48 h, doing of this substrate an interesting biocompatible support to test the cell behaviour.

The physical and electrochemical properties of these films were characterized by the material physics research group coordinated by Prof. Beatrice Fraboni, using several experimental techniques: cyclic voltammetries, spectrophotometry, atomic force microscopy (AFM), and energy dispersive X-ray (EDX) spectroscopy.

My contribution in this work has mainly regarded the study of the cellular response to the redox forms of PEDOT:PSS substrates, in two different ways: monitoring the bioelectric properties of cells seeded on these substrates through patch clamp recordings of potassium currents and resting membrane potential, and performing growth experiments to assess the adhesion capability and the replicative boost.

The results obtained clearly indicate that redox state of PEDOT:PSS can elicit strong effects on the behaviour of cells through a sort of "sponge-like" effect, that leads to a modulation of the electrochemical equilibrium due to the strong ion exchange properties of this material. This "sponge effect" offers the opportunity to actively change the availability of ionic species around the cell, that is, the key actors in setting the intensity and the dynamic of the cell response, even in terms of cell adhesion and proliferation. This study has been focused on K^+, but other types of cations and anions could be specifically included into the PEDOT:PSS film, through the doping process. This, potentially, could allow the control of a variety of cellular processes linked to the specific bioelectrical features of the doped PEDOT:PSS substrate. Furthermore, these findings revealed that the effect of the redox state of conjugated polymers on cell growth is not related to a single physical or chemical parameter of the material itself, but it is mediated by the interaction with the solution in which the cells are immersed. This new result paves the way for future applications of bioelectronics and biotechnology directed toward controlling the behaviour of a wide range of cells and tissues.

Another topic studied in this work is the phenomenon of galvanotaxis. It regards the moviment of cells under the effect of electric fields. To investigate the galvanotaxis an electronic system based on an Arduino2 board was designed and developed, capable to generate electric fields, static or variable over time, in a scientific and easily reproducible manner. Cells were plated within a Petri dish and placed in a specific holder mounted on the table of the automated microscope to observe cell movements under the influence of an electric field. Experiments were performed applying an external electric field through copper electrodes placed externally to the Petri dish, ("non-contact"

mode) or, by closing the circuit in series with the culture medium, to generate a current flowing within the culture medium itself ("contact" mode). The preliminary results obtained with this device have been shown that, in the "contact-mode", the current drops extremely fast within the first hour of the experiment, probably due to the increase of the electric resistance as a consequence of the amount of ions and charged molecules of the culture medium, that accumulate in proximity of the electrodes. On the other hand, data obtained in the "non-contact" mode, even if statistically weak, revealed that an electric field of 4.7 V/cm can affect the behaviour of the cells tested in this work, but not homogenously. In fact, although it was not recorded a net movement of cell towards one of the electrodes, almost half of the considered cells showed an alignment along the perpendicular to the electric field. The first data collected highlighted that the experimental design and the electronic platform are suitable to study the cellular galvanotaxis phenomenon, and that the device employed might be further used to improve the current knowledge in this topic.

Finally, the attention has been focused on the K^+ channels involvment in the Hutchinson-Gilford Progeria Syndrome (HGPS), an extremely rare genetic disorder in which symptoms resembling aspects of aging are manifested at a very early age. In this study, the effects of the pathology on the activity of Ca^{2+}-activated K^+ (BK_{Ca}) channels were assessed by analyzing the outward current amplitudes of human dermal fibroblasts (hDF) obtained from juvenile patients affected by HGPS and healthy donors, considered as control group. Growth experiments were performed for both cell populations in order to evaluate a possible causal correlation between the BK_{Ca} channels activity and the replicative process; therefore adhesion and proliferation rates have been tested in treated and un-treated hDF cells with Iberiotoxin, a selective BK_{Ca} inhibitor. The results obtained revealed that hDF cells affected by HGPS show a K^+ current amplitude and an expression of BK_{Ca} channels higher than the control group; furthermore, also the proliferation boost appears impaired in HGPS. Therefore, besides the other possible progerin-dependent pathways that may lead to an accelerated aging in HGPS, this study demonstrated

that the overexpression of BK_{Ca} channels, inducing cellular senescence, may be a significant factor contributing to the development of premature ageing in HGPS patients. Thus, understanding the role of the ion channels expressed in cells carrying HGPS may lead to a better knowledge of this disease and implications on physiological aging.

Bibliography

[1] S. Ringer. Regarding the action of hydrate of soda, hydrate of ammonia, and hydrate of potash on the ventricle of the frog's heart. *The Journal of Physiology*, 3(3-4):195-202, 1882.

[2] S. Ringer. Concerning the influence exerted by each of the constituents of the blood on the contraction of the ventricle. *The Journal of Physiology*, 3(5-6):380-393, 1882.

[3] S. Ringer. A further contribution regarding the influence of the different constituents of the blood on the contraction of the heart. *The Journal of Physiology*, 4(1):29-42.3, 1883.

[4] S. Ringer. A third contribution regarding the Influence of the inorganic constituents of the blood on the ventricular contraction. *The Journal of Physiology*, 4(2-3):222-225, 1883.

[5] D. J. Miller. Sydney Ringer; physiological saline, calcium and the contraction of the heart. *The Journal of Physiology*, 555(Pt 3):585-587, 2004.

[6] W. Nernst. Zur Kinetik der in Lösung befindlichen Körper. Erste Abhandlung. Theorie der Diffusion. *Z. phys. Chem.*, 2(9):613-637, 1888.

[7] J. Bernstein. *Elektrobiologie-Die Lehre von den Elektrischen Vorgängen im Organismus auf Moderner Grundlage Dargestellt*. Springer, 1912.

[8] E.A. Seyfarth. Julius Bernstein (1839-1917): pioneer neurobiologist and biophysicist. *Biol. Cybern.*, 94(1):2-8, 2006

[9] B. Hille. *Ion channels of excitable membranes*, Sinauer Associates, 3rd edition, 2001.

[10] A. L. Hodgkin and A. F. Huxley. A quantitative description of membrane current and its application to conduction and excitation in nerve. *The Journal of Physiology*, 117(4):500-544, 1952.

[11] Nobelprize.org. Nobel Media AB 2014. The Nobel Prize in Physiology or Medicine 1963. `www.nobelprize.org/nobel_prizes/medicine/laureates/1963`.

[12] E. Neher and B. Sakmann. Single-channel currents recorded from membrane of denervated frog muscle fibres. *Nature*, 260(5554):799-802, 1976.

[13] Nobelprize.org. Nobel Media AB 2014. The Nobel Prize in Physiology or Medicine 1991. `www.nobelprize.org/nobel_prizes/medicine/laureates/1991`.

[14] D. A. Doyle, J. Cabral Morais, R. A. Pfuetzner, A. Kuo, J. M. Gulbis, S. L. Cohen, B. T. Chait and R. MacKinnon. The structure of the potassium channel: molecular basis of K^+ conduction and selectivity. *Science*, 280(5360):69-77, 1998.

[15] A. Becchetti and A. Arcangeli. *Integrins and ion channels*. Springer, New York, 2010.

[16] M. Marzocchi, I. Gualandi, M. Calienni, I. Zironi, E. Scavetta, G. Castellani and B. Fraboni. Physical and electrochemical properties of PEDOT:PSS as a tool for controlling cell growth. *ACS Appl. Mater. Interfaces*, 7(32):17993-8003, 2015.

[17] N. M. Maraldi and G. Lattanzi. Involvement of prelamin A in laminopathies. *Crit. Rev. Eukaryot. Gene Expr.*, 17(4):317-334, 2007.

[18] G. Lattanzi, S. Marmiroli, A. Facchini and N. M. Maraldi. Nuclear damages and oxidative stress: new perspectives for laminopathies. *Eur. J. Histochem.*, 56(4):e45, 2012.

[19] I. Zironi, P. Gaibani, D. Remondini, S. Salvioli, S. Altilia, M. Pierini, G. Aicardi, E. Verondini, L. Milanesi, F. Bersani, S. Gravina, I. B. Roninson, C. Franceschi and G. Castellani. Molecular remodeling of potassium channels in fibroblasts from centenarians: a marker of longevity? *Mech. Ageing Dev.*, 131(11-12):674-681, 2010.

[20] D. W. Deamer. Origins of life: How leaky were primitive cells? *Nature*, 454(7200):37-8, 2008.

[21] B. Alberts, A. Johnson, J. Lewis, M. Raff, K. Roberts and P. Walter. *Molecular biology of the cell*. Garland Science, New York, 4th edition, 2002.

[22] S. Demarche, K. Sugihara, T. Zambelli, L. Tiefenauer and J. Vörös. Techniques for recording reconstituted ion channels. *Analyst*, 136(6):1077-89, 2011.

[23] A. F. Kintzer and R. M. Stroud. Structure, inhibition, and regulatory sites of TPC1 from *rabidopsis thaliana*. *Nature*, 531(7593):258-62, 2016.

[24] S. Ghatta, D. Nimmagadda, X. Xu and S. T. O'Rourke. Large-conductance, calcium-activated potassium channels: structural and functional implications. *Pharmacol Ther.*, 110(1):103-16, 2006.

[25] Z. Wang, Y. Jiang, L. Lu, R. Huang, Q. Hou and F. Shi. Molecular mechanisms of cyclic nucleotide-gated ion channel gating. *J. Genet. Genomics*, 34(6):477-85, 2007.

[26] M. Baruscotti, A. Bucchi and D. Difrancesco. Physiology and pharmacology of the cardiac pacemaker ("funny") current. *Pharmacol Ther.*, 107(1):59-79, 2005.

[27] B. Nilius and G. Owsianik. *The transient receptor potential family of ion channels.* Genome Biology, 12:218, 2011.

[28] P. L. Piechotta, M. Rapedius, P. J. Stansfeld, M. K. Bollepalli, G. Ehrlich, I. Andres-Enguix, H. Fritzenschaft, N. Decher, M. S. Sansom, S. J. Tucker and T. Baukrowitz. The pore structure and gating mechanism of K2P channels. *EMBO J.*, 30(17):3607-19, 2011.

[29] T. J. Jegla, C. M. Zmasek, S. Batalov and S. K. Nayak. Evolution of the human ion channel set. *Comb. Chem. High Throughput Screen*, 12(1):2-23, 2009.

[30] S. P. Alexander, H. E. Benson, E. Faccenda, A. J. Pawson, J. L. Sharman, W. A. Catterall, M. Spedding, J. A. Peters, A. J. Harmar and CGTP Collaborators. The concise guide to PHARMACOLOGY 2013/14: ion channels. *Br. J. Pharmacol.*, 170(8):1607-51, 2013.

[31] F. H. Yu and W. A. Catterall. The VGL-chanome: a protein superfamily specialized for electrical signalling and ionic homeostasis. *Sci STKE*, (253):re15, 2004.

[32] A. L. Hodgkin and B. Katz. The effect of sodium ions on the electrical activity of the giant axon of the squid. *J. Physiol.*, 108;37-77, 1949.

[33] Q. Kuang, P. Purhonen and H. Hebert. Structure of potassium channels. *Cell. Mol. Life Sci.*, 72:3677-3693, 2015.

[34] G. Yellen. The voltage-gated potassium channels and their relatives. *Nature.* 419(6902):35-42, 2002.

[35] S. A. Seoh, D. Sigg, D. M. Papazian and F. Bezanilla. Voltage-sensing residues in the S2 and S4 segments of the Shaker K^+ channel. *Neuron*, 16(6):1159-1167, 1996.

[36] S. K. Aggarwal and R. MacKinnon. Contribution of the S4 segment to gating charge in the Shaker K^+ channel. *Neuron*, 16(6):1169-1177, 1996.

[37] N.Yang, A. L. George Jr. and R. Horn. Molecular basis of charge movement in voltage-gated sodium channels. *Neuron*, 16(1):113-122, 1996.

[38] H. P. Larsson, O. S. Baker, D. S. Dhillon and E. Y. Isacoff. Transmembrane movement of the Shaker K^+ channel S4. *Neuron*, 16(2):387-397, 1996.

[39] M. Ø. Jensen, V. Jogini, D. W. Borhani, A. E. Leffler, R. O. Dror and D. E. Shaw. Mechanism of voltage gating in potassium channels. *Science*, 336(6078):229-33, 2012.

[40] A. Mathie, J. R. A. Wooltorton and C. S. Watkins. Voltage-activated potassium channels in mammalian neurons and their block by novel pharmacological agents. *Gen. Pharmacol.*, 30(1):13-24, 1998.

[41] K. M. Giangiacomo, M. L. Garcia and O. B. McManus. Mechanism of iberiotoxin block of the large-conductance calcium-activated potassium channel from bovine aortic smooth muscle. *Biochemistry* 31(29):6719-27, 1992.

[42] A. L. Harvey. Twenty years of dendrotoxins. *Toxicon*, 39(1):15-26, 2000.

[43] J. M. Nerbonne. Molecular basis of functional voltage-gated K^+ channel diversity in the mammalian myocardium. *J. Physiol.*, 525 Pt 2:285-98, 2000.

[44] L. A. Pardo and W. Stühmer. The roles of K^+ channels in cancer. *Nat. Rev. Cancer*, 14(1):39-48, 2014.

[45] C. Le Clainche and M. F. Carlier. Regulation of actin assembly associated with protrusion and adhesion in cell migration. *Physiol. Rev.*, 88(2):489-513, 2008.

[46] Roth | McFarlane Hand and Upper Limb Centre (HULC), Cell and Molecular Laboratory, London. `www.uwo.ca/surgery/plastics/HULCcellmollab/dups.htm`.

[47] B. Ladoux and A. Nicolas. Physically based principles of cell adhesion mechanosensitivity in tissues. *Rep. Prog. Phys.*, 75(11):116601, 2012.

[48] A. Schwab, P. Hanley, A. Fabian and C. Stock. Potassium channels keep mobile cells on the go. *Physiology (Bethesda)*, 23:212-20, 2008.

[49] A. Schwab, L. Wojnowski, K. Gabriel and H. Oberleithner. Oscillating activity of a Ca^{2+}-sensitive K^+ channel. A prerequisite for migration of transformed Madin-Darby canine kidney focus cells. *Journal of Clinical Investigation*, 93(4):1631-1636, 1994.

[50] J. Q. Zheng and M. M. Poo. Calcium signaling in neuronal motility. *Annu. Rev. Cell Dev. Biol.*, 23:375-404, 2007.

[51] R. Maroto and O. P. Hamill. MscCa Regulation of Tumor Cell Migration and Metastasis. *Curr. Top Membr.*, 59:485-509, 2007.

[52] M. B. Mcferrin and H. Sontheimer. A role for ion channels in glioma cell invasion. *Neuron Glia Biol.*, 2(1):39-49, 2006.

[53] S. F. Pedersen, E. K. Hoffmann and J. W. Mills. The cytoskeleton and cell volume regulation. *Comp. Biochem. Physiol. A*, 130: 385-399, 2001.

[54] A. Arcangeli, O. Crociani and L.Bencini. Interaction of tumour cells with their microenvironment: ion channels and cell adhesion molecules. A focus on pancreatic cancer. *Philos. Trans. R. Soc. Lond. B Biol. Sci.*, 369(1638):20130101, 2014.

[55] M. R. Williams, J. C. Markey, M. A. Doczi and A. D. Morielli. An essential role for cortactin in the modulation of the potassium channel Kv1.2. *Proc. Natl. Acad. Sci. U S A*, 104(44):17412-7, 2007.

[56] R. Rezzonico, C. Cayatte, I. Bourget-Ponzio, G. Romey, N. Belhacene, A. Loubat, S. Rocchi, E. Van Obberghen, J. A. Girault, B. Rossi and H. Schmid-Antomarchi. Focal adhesion kinase pp125FAK interacts with the large conductance calcium-activated hSlo potassium channel in human osteoblasts: potential role in mechanotransduction. *J. Bone Miner Res.*, 18(10):1863-1871, 2003.

[57] Y. J. Huang, G. Hoffmann, B. Wheeler, P. Schiapparelli, A. Quinones-Hinojosa and P. Searson. Cellular microenvironment modulates the galvanotaxis of brain tumor initiating cells. *Scientific Reports*, 6:21583, 2016.

[58] R. H. W. Funk. Endogenous electric fields as guiding cue for cell migration. *Front. Physiol.*, 6:143, 2015.

[59] M. E. Mycielska and M. B. A. Djamgoz. Cellular mechanisms of direct-current electric field effects: galvanotaxis and metastatic disease. *Journal of Cell Science*, 117(Pt 9):1631-1639, 2004.

[60] M. Allen, A. Mogilner and J. Theriot. Electrophoresis of cellular membrane components creates the directional cue guiding keratocyte galvanotaxis. *Curr. Biol.*, 23:560-8, 2013.

[61] C. H. Golias, A. Charalabopoulos and K. Charalabopoulos. Cell proliferation and cell cycle control: a mini review. *Int. J. Clin. Pract.*, 58(12):1134-41, 2004.

[62] F. Lang, M. Foller, K. S. Lang, P. A. Lang, M. Ritter, E. Gulbins, A. Vereninov and S. M. Huber. Ion channels in cell proliferation and apoptotic cell death. *J. Membrane Biol.*, 205(3):147-57, 2005.

[63] A. Stutzin and E. K. Hoffmann. Swelling-activated ion channels: functional regulation in cell-swelling, proliferation and apoptosis. *Acta Physiol. (Oxf)*, 187(1-2):27-42, 2006.

[64] T. K. Klausen, A. Bergdahl, C. Hougaard, P. Christophersen, S. F. Pedersen and E. K. Hoffmann. Cell cycle-dependent activity of the volume- and Ca^{2+} -activated anion currents in Ehrlich lettre ascites cells. *J. Cell. Physiol.*, 210:831-842, 2007.

[65] H. Ouadid-Ahidouch, X. Le Bourhis, M. Roudbaraki, R. A. Toillon, P. Delcourt and N. Prevarskaya. Changes in the K^+ current-density of MCF-7 cells during progression through the cell cycle: possible involvement of a h-ether.a-gogo K^+ channel. *Receptors Channels*, 7(5):345-56, 2001.

[66] H. Ouadid-Ahidouch, M. Roudbaraki, P. Delcourt, A. Ahidouch, N. Joury and N. Prevarskaya. Functional and molecular identification of intermediate-conductance Ca^{2+}-activated K^+ channels in breast cancer cells: association with cell cycle progression. *Am. J. Physiol. Cell Physiol.*, 287(1):C125-34, 2004.

[67] J. Blackiston, K. A. McLaughlinand and M. Levin. Bioelectric controls of cell proliferation: ion channels, membrane voltage and the cell cycle. *Cell Cycle*, 8(21):3527-3536, 2009.

[68] R. J. Molenaar. Ion channels in glioblastoma. *ISRN Neurology*, 2011:590249, 2011.

[69] V. R. Rao, M. Perez-Neut, S. Kaja and S. Gentile. Voltage-gated ion channels in cancer cell proliferation. *Cancers*, 7, 849-875, 2015.

[70] P. Urrego, F. Tomczak, W. Zahed, L. Stühmer and A. Pardo. Potassium channels in cell Cycle and cell croliferation. *Philos. Trans. R. Soc. Lond. B. Biol. Sci.*, 369(1638):20130094, 2014.

[71] F. Amorini. Proprietá elettriche di cellule interagenti con matrici polimeriche biocompatibili. *Master's Thesis*, University of Bologna, 2014.

[72] HEKA Elektronik Dr. Schulze GmbH, Germany, `www.heka.com`

[73] B. Sakmann and E. Neher. *Single-channel recording*. Springer, New York, 1995.

[74] M. Nikolou, and G. G. Malliaras. Applications of poly(3,4-ethylenedioxythiophene) doped with poly(styrene-sulfonic-acid) transistors in chemical and biological sensors. *Chem. Rec.*, 8(1):13-22, 2008.

[75] J. Rivnay, R. M. Owens and G. G. Malliaras. The rise of organic bioelectronics. *Chem. Mater.*, 26(1):679-685, 2014.

[76] S. C. Luo, E. M. Ali, N. C. Tansil, H. H. Yu, S. Gao, E. A. B. Kantchev and J. Y. Ying. Poly(3,4-ethylenedioxythiophene) (PEDOT) nanobiointerfaces: thin, ultrasmooth, and functionalized PEDOT films with in vitro and in vivo biocompatibility. *Langmuir*, 24:8071-8077, 2008.

[77] B. Zhu, S. C. Luo, H. Zhao, H. A. Lin, J. Sekine, A. Nakao, C. Chen, Y. Yamashita and H. H. Yu. Large enhancement in neurite outgrowth on a cell membrane-mimicking conducting polymer. *Nat. Commun.*, 5, 4523, DOI:10.1038/ncomms5523, 2014.

[78] H. Yamato, M. Ohwa and W. Wernet. Stability of polypyrrole and poly(3,4-ethylenedioxythiophene) for biosensor application. *J. Electroanal. Chem.*, 397:163-170, 1995.

[79] R. Balint, N. J. Cassidy and S. H. Cartmell. Conductive polymers: towards a smart biomaterial for tissue engineering. *Acta Biomater.*, 10:2341-2353, 2014.

[80] J. Y. Wong, R. Langer and D. E. Ingber. Electrically conducting polymers can non invasively control the shape and growth of mammalian cells. *Proc. Natl. Acad. Sci. U. S. A.*, 91:3201-3204, 1994.

[81] C. Saltó, E. Saindon, M. Bolin, A. Kanciurzewska, M. Fahlman, E. W. H. Jager, P. Tengvall, E. Arenas and M. Berggren. Control of neural stem cell adhesion and density by an electronic polymer Surface Switch. *Langmuir*, 24:14133-14138, 2008.

[82] K. Svennersten, M. H. Bolin, E. W. H. Jager, M. Berggren and A. Richter-Dahlfors. Electrochemical modulation of epithelia formation using conducting polymers. *Biomaterials*, 30:6257-6264, 2009.

[83] M. D. Wan, D. J. Brooks, A. Gumus, C. Fischbach and G. G. Malliaras. Electrical control of cell density gradients on a conducting polymer surface. *Chem. Commun.*, 35:5278-5280, 2009.

[84] M. D. Wan, R. M. Schur, C. K. Ober, C. Fischbach, D Gourdon and G. G. Malliaras. Electrical control of protein conformation. *Adv. Mater.*, 24:2501-2505, 2012.

[85] F. Greco, T. Fujie, L. Ricotti, S. Taccola, B. Mazzolai and V. Mattoli. Microwrinkled conducting polymer interface for anisotropic multicellular alignment. *ACS Appl. Mater. Interfaces*, 5:573-584, 2013.

[86] K. M. Sivaraman, B. Ozkale, O. Ergeneman, T. Lühmann, G. Fortunato, M. A. Zeeshan, B. J. Nelson and S. Pané. Redox

cycling for passive modification of polypyrrole surface properties: effects on cell adhesion and proliferation. *Adv. Healthcare Mater.*, 2:591-598, 2013.

[87] F. Pires, Q. Ferreira, C. A. V. Rodrigues, J. Morgado and F. C. Ferreira. Neural stem cell differentiation by electrical stimulation using a cross-linked PEDOT substrate: expanding the use of biocompatible conjugated conductive polymers for neural tissue engineering. *Biochim. Biophys. Acta*, 1850:1158-1168, 2015.

[88] M. D. Wan, E. M. Chandler, M. Madhavan, D. W. Infanger, C. K. Ober, D. Gourdon, D, G. G. Malliaras and C. Fischbach. Fibronectin conformation regulates the proangiogenic capability of tumor-associated adipogenic stromal cells. *Biochim. Biophys. Acta*, 1830:4314-4320, 2013.

[89] M. D. Wan, S. Inal, T. Williams, K. Wang, P. Leleux, L. Estevez, E. P. Giannelis, C. Fischbach, G. G. Malliaras and D. Gourdon. 3D conducting polymer platforms for electrical control of protein conformation and cellular functions. *J. Mater. Chem. B*, 3:5040-5048, 2015.

[90] C. A. Thomas, K. Zong, P. Schottland and J. R. Reynolds. Poly(3,4-alkylenedioxypyrrole)s as highly stable aqueous-compatible conducting polymers with biomedical implications. *Adv. Mater.*, 12:222-225, 2000.

[91] R. Kiebooms, A. Aleshin, K. Hutchison and F. Wudl. Thermal and electromagnetic behavior of doped poly(3,4-ethylenedioxythiophene) films. *J. Phys. Chem. B*, 101(51):11037, 1997.

[92] D. Mecerreyes, R. Marcilla, E. Ochoteco, H. Grande, J. A. Pomposo, R. Vergaz and J. M. Sanchez Pena. A simplified all-polymer flexible electrochromic device. *Electrochim. Acta*, 49(21):3555-3559, 2004.

[93] Q. Pei, G. Zuccarello, M. Ahskog and O. Inganas. Electrochromic and highly stable poly(3,4-ethylenedioxythiophene) switches between opaque blue-black and transparent sky blue. *Polymer*, 35(7):1347, 1994.

[94] G. Heywang and F. Jonas. Poly(alkylenedioxythiophene)s new, very stable conducting polymers. *Adv. Mater.*, 4(2):116-118, 1992.

[95] M. Dietrich, J. Heinze, G. Heywang, and F. Jonas. Electrochemical and spectroscopic characterization of polyalkylenedioxythiophenes. *J. Electroanal. Chem.*, 369(1-2):87-92, 1994.

[96] M. Proctor, J. Rivnay and G. G. Malliaras. Understanding volumetric capacitance in conducting polymers. *J. Polym. Sci. Part B: Polym. Phys*, 54:1433-1436, 2016.

[97] M. Marzocchi. Conducting polymers as novel tools for biosensing and tissue engineering. *Ph. D. Thesis*, University of Bologna, 2015.

[98] X. Strakosas, B. Wei, D. C. Martin and R. M. Owens. Biofunctionalization of polydioxythiophene derivatives for biomedical applications. *J. Mater. Chem. B*, 4:4952-4968, 2016.

[99] V. Karagkiozaki, P. G. Karagiannidis, M. Gioti, P. Kavatzikidou, D. Georgiou and E. Georgaraki. Bioelectronics meets nanomedicine for cardiovascular implants: PEDOT-based nanocoatings for tissue regeneration. *Biochim. Biophys. Acta*, 1830:4294-4304, 2013.

[100] M. Berggren and A. Richter-Dahlfors. Organic bioelectronics. *Adv. Mater.*, 19:3201-3213, 2007.

[101] J. E. Collazos-Castro, J. L. Polo, G. R. Hernández-Labrado, V. Padial-Canete and C. García-Rama. Bioelectrochemical control of neural cell development on conducting polymers. *Biomaterials*, 31:9244-9255, 2010.

[102] R. M. Miriani, M. R. Abidian and D. R. Kipke. Cytotoxic analysis of the conducting polymer PEDOT using myocytes. *30th Annual International IEEE EMBS Conference*, 20-24, 2008.

[103] K. S. The and Y. W. Lu. Surface nanostructuring of biocompatible polymer for wettability control in MEMS. *21st Annual International IEEE MEMS Conference*, 363-366, 2008.

[104] M. J. Dalby, S. J. Yarwood, H. J. Johnstone, S. Affrossman and M. O. Riehle. Fibroblast signaling events in response to nanotopography: a gene array study. *IEEE Trans. Nanobioscience*, 1:12-17, 2002.

[105] A. S. Andersson, J. Brink, U. Lidberg and D. S. Sutherland. Influence of systematically varied nanoscale topography on the morphology of epithelial cells. *IEEE Trans. Nanobioscience*, 2:49-57, 2003.

[106] J. M. Rice, J. A. Hunt, J. A. Gallagher, P. Hanarp, D. S. Sutherland and J. Gold. Quantitative assessment of the response of primary derived human osteoblasts and macrophages to a range of nanotopography surfaces in a single culture model in vitro. *Biomaterials*, 24:4799-4818, 2003.

[107] M. J. Dalby, M. O. Riehlea, D. S. Sutherlandb, H. Aghelib and A. S. G. Curtisa. Use of nanotopography to study mechanotransduction in fibroblasts: methods and perspectives. *Eur. J. Cell Biol.*, 83:159-169, 2004.

[108] V. Vogel and M. Sheetz. Local force and geometry sensing regulate cell functions. *Nat. Rev. Mol. Cell Biol.*, 7:265-275, 2006.

[109] V. Brunetti, G. Maiorano, L. Rizzello, B. Sorce, S. Sabella, R. Cingolani and P. P. Pompa. Neurons sense nanoscale roughness

with nanometer sensitivity. *Proc. Natl. Acad. Sci., U.S.A.*, 107:6264-6269, 2010.

[110] J. H. Lee, G. Khang, J. W. Lee and H. B. Lee. Interaction of different types of cells on polymer surfaces with wettability gradient. *J. Colloid Interface Sci.*, 205:323-330, 1998.

[111] A. Ranella, M. Barberoglou, S. Bakogianni, C. Fotakis and E. Stratakis. Tuning cell adhesion by controlling the roughness and wettability of 3D micro/nano silicon structures. *Acta Biomater.*, 6:2711-2720, 2010.

[112] M. Levite, L. Cahalon, A. Peretz, R. Hershkoviz, A. Sobko, A. Ariel, R. Desai, B. Attali, and O. Lider. Extracellular K^+ and opening of voltage-gated potassium channels activate T cell integrin function: physical and functional association between $K_{v1.3}$ channels and $\beta 1$ integrins. *J. Exp. Med.*, 191:1167-1176, 2000.

[113] M. J. Higgins, S. T. McGovern and G. G. Wallace. Visualizing dynamic actuation of ultrathin polypyrrole films. *Langmuir*, 25:3627-3633, 2009.

[114] A. Zykwinska, W. Domagala, B. Pilawa and M. Lapkowski. Electrochemical overoxidation of poly(3,4-ethylenedioxythiophene)-PEDOT studied by means of in situ ESR spectroelectrochemistry. *Electrochim. Acta*, 50:1625-1633, 2005.

[115] J. Oostra, K. H. Van Den Bos, P. W. Blom and J. J. Michels. Disruption of the electrical conductivity of highly conductive poly(3,4-ethylenedioxythiophene):poly(styrene sulfonate) by hypochlorite. *J. Phys. Chem. B.*, 117:10929-10935, 2013.

[116] M. L. Olsen and H. Sontheimer. Mislocalization of K_{ir} channels in malignant glia. *Glia*, 46:63-73, 2004.

[117] C. Callies, J. Fels, I. Liashkovich, K. Kliche, P. Jeggle, K. Kusche-Vihrog and H. Oberleithner. Membrane potential depolarization decreases the stiffness of vascular endothelial cells. *J. Cell Sci.*, 124:1936-1942, 2011.

[118] C. B. Ransom and H. Sontheimer. BK channels in human glioma cells. *J. Neurophysiol.*, 85:790-803, 2001.

[119] M. Guéguinou, A. Chantome, G. Fromont, P. Bougnoux, C. Vandier and M. Potier-Cartereau. K_{Ca} and Ca^{2+} channels: the complex thought. *Biochim. Biophys. Acta*, 1843:2322-2333, 2014.

[120] A. J. Ridley, M. A. Schwartz, K. Burridge, R. A. Firtel, M. H. Ginsberg, G. Borisy, J. T. Parsons, and A. R. Horwitz. Cell migration: integrating signals from front to back. *Science*, 302:1704-1709, 2003.

[121] M. J. Berridge, M. D. Bootman and P. Lipp. Calcium - a life and death signal. *Nature*, 395:645-648, 1998.

[122] W. Nagel. Uber Galvanotaxis. *Pflugers Archive f.d. ges. Physiology*, 59, 603-642, 1895.

[123] M. A. Messerli and D. M. Graham. Extracellular electrical fields direct wound healing and regeneration. *Biol. Bull.*, 221, 79-92, 2011.

[124] K. Ahirwar, M. W. Nasser, T. H. Jones, E. K. Sequin, J. D. West, T. L. Henthorne, J. Javor, A. M. Kaushik, R. K. Ganju and V. V. Subramaniam. Non-contact method for directing electrotaxis. *Sci. Rep.*, 5, 11005, 2015.

[125] K. R. Robinson. The responses of cells to electrical fields: a review. *J. Cell Biol.*, 101 2023-2027, 1985.

[126] K. Y. Nishimura, R. R. Isseroff and R. Nuccitelli. Human keratinocytes migrate to the negative pole in direct current electric

fields comparable to those measured in mammalian wounds. *J. Cell Sci.*, 109(Pt1):199-207, 1996.

[127] C. D. McCaig, B. Song and A. M. Rajnicek. Electrical dimensions in cell science. *J. Cell Sci.*, 122(Pt23):4267-4276, 2009.

[128] M. Zhao, C. D. McCaig, A. Agius-Fernandez, J. V. Forrester and K. Araki-Sasaki. Human corneal epithelial cells reorient and migrate cathodally in a small applied electric field. *Curr. Eye Res.*, 16, 973-984, 1997.

[129] M. B. A. Djamgoz, M. Mycielska, Z. Madeja, S. P. Fraser and W. Korohoda. Directional movement of rat prostate cancer cells in direct-current electric field: involvement of voltage gated Na^+ channel activity. *J. Cell. Sci.*, 114(Pt14):2697-2705, 2001.

[130] C. E. Pullar, B. S. Baier, Y. Kariya, A. J. Russell, B. A. Horst, M. P. Marinkovich and R. R. Isseroff. beta4 integrin and epidermal growth factor coordinately regulate electric field-mediated directional migration via Rac1. *Mol. Biol. Cell*, 17(11):4925-4935, 2006.

[131] R. H. Funk, T. Monsees and N. Ozkucur. Electromagnetic effects-from cell biology to medicine. *Prog. Histochem. Cytochem.*, 43(4):177-264, 2009.

[132] M. Zhao, J. Pu, J. V. Forrester and C. D. McCaig. Membrane lipids, EGF receptors, and intracellular signals colocalize and are polarized in epithelial cells moving directionally in a physiological electric field. *FASEB J.*, 16(8):857-859, 2002.

[133] P. Friedl and K. Wolf. Tumour-cell invasion and migration: diversity and escape mechanisms. *Nat. Rev. Cancer*, 3(5):362-374, 2003.

[134] R. Trollinger, R. R. Isseroff and R. Nuccitelli. Calcium channels blockers inhibit galvanotaxis in human keratinocytes. *J. Cell. Physiol.*, 193(1):1-9, 2002.

[135] D. Bray. *Cell movements: from molecules to motility*. New York, Garland, 2001.

[136] W. S. Beane, J. Morokuma, J. M. Lemire and M. Levin. Bioelectric signaling regulates head and organsize during planarian regeneration. *Development*, 140(2):313-322, 2013.

[137] Y. Li, M. Weiss and L. Yao. Directed migration of embryonic stem cell-derived neural cells in an applied electric field. *Stem Cell Rev.*, 10(5):653-62, 2014.

[138] D. J. Cohen, W. J. Nelson and M. M. Maharbiz. Galvanotactic control of collective cell migration in epithelial monolayers. *Nat. Mater.*, 13, 409-417, 2014.

[139] Y. J. Huang, J. Samorajski, R. Kreimer and P. C. Searson. The influence of electric fields and confinement on cell motility. *PLoS ONE*, 8, 1-9, 2013.

[140] Li and F. Lin. Microfluidic devices for studying chemotaxis and electrotaxis. *Trends Cell Bio.*, 21(8):489-497, 2011.

[141] B. Song, Y. Gu, J. Pu, B. Reid, Z. Zhao and M. Zhao. Application of direct current electric fields to cells and tissues in vitro and modulation of wound electric field in vivo. *Nat. Protoc.*, 2(6):1479-1489, 2007.

[142] D. Wu, X. Ma and F. Lin. DC electric fields direct breast cancer cell migration, induce EGFR polarization, and increase the intracellular level of calcium ions. *Cell Biochem. Biophys.*, 67(3):1115-1125, 2013.

[143] M. S. Cooper and R. E. Keller. Perpendicular orientation and directional migration of amphibian neural crest cells in dc electrical fields. *Proc. Natl. Acad. Sci. U S A.*, 81(1):160-4, 1984.

[144] D. Wu and F. Lin. Recent developments in electrotaxis assays. *Adv. Wound Care (New Rochelle)*, 3(2):149-155, 2014.

[145] H. Zhao, A. Steiger, M. Nohner and H. Ye. Specific intensity direct current (DC) electric field improves neural stem cell migration and enhances differentiation towards βIII-Tubulin+ neurons. *PLoS One*, 10, e0129625, 2015.

[146] R. L. Pollex and R. A. Hegele. Hutchinson-Gilford progeria syndrome. *Clin. Genet.*, 66:375-381, 2004.

[147] J. K. Sinha, S. Ghosh and M. Raghunath. Progeria: A rare genetic premature ageing disorder. *Indian J. Med. Res.*, 139:667-674, 2014.

[148] M. Eriksson, W. T. Brown, L. B. Gordon, M. W. Glynn, J. Singer, L. Scott, M. R. Erdos, C. M. Robbins, T. Y. Moses, P. Berglund, A. Dutra, E. Pak, S. Durkin, A. B. Csoka, M. Boehnke, T. W. Glover and F. S. Collins. Recurrent de novo point mutations in lamin A cause Hutchinson-Gilford progeria syndrome. *Nature*, 423:293-298, 2003.

[149] J. M. Gonzalez, D. Pla, D. Perez-Sala and V. Andres. A-type lamins and Hutchinson-Gilford progeria syndrome: pathogenesis and therapy. *Front. Biosci. (Schol Ed)*, 3:1133-1146, 2011.

[150] E. Mattioli, M. Columbaro, C. Capanni, N. M. Maraldi, V. Cenni, K. Scotlandi, M. T. Marino, L. Merlini, S. Squarzoni and G. Lattanzi. Prelamin A-mediated recruitment of SUN1 to the nuclear envelope directs nuclear positioning in human muscle. *Cell Death Differ.*, 18(8):1305-1315, 2011.

[151] W. Arancio, G. Pizzolanti, S. I. Genovese, M. Pitrone and C. Giordano. Epigenetic involvement in Hutchinson-Gilford progeria syndrome: a mini-review. *Gerontology*, 60(3):197-203, 2014.

[152] S. Ghosh and Z. Zhou. Genetics of aging, progeria and lamin disorders. *Curr. Opin. Genet. Dev.*, 26:41-46, 2014.

[153] G. Lattanzi, M. Ortolani, M. Columbaro, S. Prencipe, E. Mattioli, C. Lanzarini, N. M. Maraldi, V. Cenni, P. Garagnani, S. Salvioli, G. Storci, M. Bonafé, C. Capanni and C. Franceschi. Lamins are rapamycin targets that impact human longevity: a study in centenarians. *J. Cell Sci.*, 127:147-157, 2014.

[154] Z. J. Chen, W. P. Wang, Y. C. Chen, J. Y. Wang, W. H. Lin, L. A. Tai, G. G. Liou, C. S. Yang and Y. H. Chi. Dysregulated interactions between lamin A and SUN1 induce abnormalities in the nuclear envelope and endoplasmic reticulum in progeric laminopathies. *J. Cell Sci.*, 127(Pt 8):1792-804, 2014.

[155] P. Scaffidi and T. Misteli. Lamin A-dependent nuclear defects in human aging. *Science*, 312:1059-1063, 2006.

[156] B. Korf. Hutchinson-Gilford progeria syndrome, aging, and the nuclear lamina. *N. Engl. J. Med.*, 358:552-5, 2008.

[157] D. McClintock, D. Ratner, M. Lokuge, D. M. Owens, L. B. Gordon, F. S. Collins and K. Djabali. The mutant form of lamin A that causes Hutchinson-Gilford progeria is a biomarker of cellular aging in human skin. *PLoS One*, 2(12):e1269, 2007.

[158] B. Sokolowski, S. Orchard, M. Harvey, S. Sridhar and Y. Sakai. Conserved BK Channel-Protein Interactions Reveal Signals Relevant to Cell Death and Survival. *PLoS One*, 6(12):e28532, 2011.

[159] L. Chen, L. Tian, S. H. MacDonald, H. McClafferty, M. S. Hammond, J. M. Huibant, P. Ruth, H. G. Knaus and M. J. Shipston. Functionally diverse complement of large conductance calcium- and voltage-activated potassium channel (BK) alpha-subunits

generated from a single site of splicing. *J Biol Chem.*, 280(39):33599-609, 2005.

[160] A. B. Csoka, S. B. English, C. P. Simkevich, D. G. Ginzinger, A. J. Butte, G. P. Schatten, F. G. Rothman and J. M. Sedivy. Genome-scale expression profiling of Hutchinson-Gilford progeria syndrome reveals widespread transcriptional misregulation leading to mesodermal/mesenchymal defects and accelerated atherosclerosis. *Aging Cell.*, 3(4):235-43, 2004.

[161] D. Camozzi, C. Capanni, V. Cenni, E. Mattioli, M. Columbaro, S. Squarzoni and G. Lattanzi. Diverse lamin-dependent mechanisms interact to control chromatin dynamics. Focus on laminopathies. *Nucleus*, 5(5):427-40, 2014.

[162] J. M. Bridger and I. R. Kill. Aging of Hutchinson-Gilford progeria syndrome fibroblasts is characterised by hyperproliferation and increased apoptosis. *Exp. Gerontol.*, 39(5):717-24, 2004.

[163] B. D. Kyle and A. P. Braun. The regulation of BK channel activity by pre- and post-translational modifications. *Front. Physiol.*, 5:316, 2014.

[164] X. Huang and L. Y. Jan. Targeting potassium channels in cancer. *J. Cell Biol.*, 206(2):151-62, 2014.

[165] C. Pellegrini, M. Columbaro, C. Capanni, M. R. D'Apice, C. Cavallo, M. Murdocca, G. Lattanzi and S. Squarzoni. All-trans retinoic acid and rapamycin normalize Hutchinson Gilford progeria fibroblast phenotype. *Oncotarget.*, 6(30):29914-28, 2015.

[166] J. Campisi and F. d'Adda di Fagagna. Cellular senescence: when bad things happen to good cells. *Nat. Rev. Mol. Cell Biol.*, 8(9):729-40, 2007.

[167] B. G. Childs, M. Durik, D. J. Baker and J. M. van Deursen. Cellular senescence in aging and age-related disease: from mechanisms to therapy. *Nat Med.*, 21(12):1424-35, 2015.

[168] H. Lallet-Daher, C. Wiel, D. Gitenay, N. Navaratnam, A. Augert, B. Le Calvé, S. Verbeke, D. Carling, S. Aubert, D. Vindrieux and D. Bernard. Potassium channel KCNA1 modulates oncogene-induced senescence and transformation. *Cancer Res.*, 73(16):5253-65, 2013.

Acknowledgements

It is my pleasure to thank all the people with whom I have collaborated to the realization of this PhD thesis. I would like to thank my supervisor, Prof. Gastone Castellani for his constant support and guidance, and my tutor, Dr. Isabella Zironi, for her patience, continuous help and, above all, for teaching me almost everything I know about electrophysiology and cell cultures.

In an interdisciplinary research field such as Bioelectronics, collaboration with researchers with different backgrounds is crucial and, at the same time, very stimulating. For this reason I really want to thank Prof. Beatrice Fraboni and her group from the Department of Physics and Astronomy of the University of Bologna, in particular Dr. Marco Marzocchi, Dr. Isacco Gualandi, Dr. Tobias Kramer and Dr. Maria Calienni for their help on all the aspects regarding the material studied, from the electrochemical characterization to our scientific discussions.

A very special thanks to my present and former colleagues in Bologna for the everyday collaboration and for creating a wonderful atmosphere in the laboratory, in particular Angela, Stefania, Laura, Daniela and Nico. Finally, I gratefully thank my family for supporting me in every choice I make, and to Laura, for always being by my side.